THEORY AND APPLICATIONS OF WAVE-MIXINGS IN PHOTOREFRACTIVE CRYSTALS

Thesis by

Sze-Keung Kwong

In Partial Fulfillment of the Requirements

for the Degree of

Doctor of Philosophy

California Institute of Technology

Pasadena, California

1986

(Submitted April 4, 1986)

Acknowlegments

I am deeply indebted, first of all, to my girlfriend, Juliana Wong, for her love, her support, both spiritual and emotional, the warmth and understanding she extended to me. Without her I could not have accomplished all these achievements.

My greatest gratitude goes to my parents, Hung Kwong and Oi Yueng Kwong, and my brothers Sze-Ki, Sze-Shan, Sze-Kwong, and Sze-Fai for their constant support and encouragement.

It is a pleasure to acknowledge the support, and supervision of my advisor, Prof. Amnon Yariv. His keen scientific insight had been a constant inspiration, and it had been a privilege to work in the dynamic environment fostered in his group.

Thanks are also extended to my colleagues Dr. Mark Cronin-Golomb, Dr. Kazuo Kyuma, Dr. Jeffery O. White and George A. Rakuljic who provided the enthusiasm, encouragement which are essential ingredients in graduate work.

I would like to thank Mr. Desmond Armstrong for his expert technical assistance. I repect him very much for his willingness to make other people's problems his.

Special thanks go to Juliana Wong, Tommy J. Wong, Koichi Sanyano, Dr. Mark Cronin-Golomb, George Rakuljic and Victor Leyva for spending their invaluable time to help in proofreading this thesis.

Finally, I would also like to express my appreciation to my fellow students, John S. Smith, Christopher Lindsey, Yasuo Tomita and Michael Mittlestein for their heplful discussions and enjoyable company.

Abstract

This thesis is an experimental and theoretical investigation of wave-mixing in photorefractive crystals and applications thereof. In the first part, the physics of the photorefractive effect is described. The figures of merit useful in characterizing various photorefractive crystals are also discussed.

In the second part, the coupled wave theory of two interacting optical waves in photorefractive crystals is reviewed. Both the energy coupling and the phase delay of the two beams are analyzed.

In the third part, the coupled wave formalism is extended to four wave mixing in photorefractive crystals. Aspects of real-time holography and phase conjugation are discussed. The coupled wave equations are solved in two special cases: (1) single grating and undepleted pump approximation; and (2) single grating and negligible absorption. The theory is then compared with the experimental results. The solutions of the phase of phase conjugation are presented. The recent developments in self-pumped phase conjugate mirrors are also discussed.

In the fourth part, new types of oscillators ultilizing the photorefractive gain are described and demonstrated. Two approaches to derive the conditions for unidirectional ring oscillation are presented and compared. The theory and experimental demonstration of a double phase conjugate resonator are described. Two applications, the optical path length to frequency conversion interferometer and the

one-way real time wave front converters, are also described.

In the last part, some applications of the previous studies are described. Two novel bistable devices using the self-pumped phase conjugate mirror are demonstrated. Mathematical operations on images, such as real time 'exclusive or' operation, image subtraction, differentiation, and intensity inversion are demonstrated using an interferometer with a self-pumped phase conjugate mirror. Finally, the theory and the experimental demonstration of an all-optical associative holographic memory are discussed. Methods of extending the number of stored messages are also discussed.

Table of Contents

Chapter 1: Introduction

(1.1) The photorefractive effect

In its broadest sense, the photorefractive effect can be interpreted as any effect involving a change of the refractive index due to the presence of light. However in this thesis and most other publications, it refers to those changes in the refractive index which relate to the formation of a periodic space-charge distribution and a corresponding index grating. Some examples of materials which display this effect are $BaTiO_3$, $Sr_xBa_{1-x}Nb_2O_6$ (SBN), $Bi_{12}SiO_{20}$ (BSO), $Bi_{12}GeO_{20}$ (BGO), $LiNbO_3$, $LiTaO_3$, $KNbO_3$, GaAs and InP. The first reported observation of the photorefractive effect was by Ashkin et al. in $LiNbO_3$ and $LiTaO_3$ (it was described as "optical damage" at that time)[1]. The effect persisted even when the light was removed, but the effect was reversible, in contrast to the catastrophic damage that occurs at much higher intensities. Later Chen et al. realized that this effect could be used to make volume holograms in $LiNbO_3$ [2,3]. The first explanation of this effect was given by Chen[4] and Amodei[5]. Their hypothesis was that free carriers were excited by the nonuniform light intensity distribution of the two intersecting coherent beams within an otherwise insulating material. These carriers migrated, until they recombined with trapping centers in dark areas, thus leading to alternating regions of unneutralized charges that persisted after the light was turned off. The electric field due to this space charge distribution

operated through the electrooptic effect to produce a refractive index grating (see Fig. 1.1). It follows from the Poisson equation that the induced index grating is phase shifted spatially from the light interference pattern because the space charge electric field was shifted by $\pi/2$ relative to the trapped charge distribution. This phase shift introduces an asymmetry that allows one of the two beams responsible for grating formation to be amplified by constructive interference with the radiation scattered by the grating from the other beam which, to conserve power, is attenuated. This asymmetry is present because the linear electrooptic effect responsible for the index grating exists only in asymmetric crystals.

Numerous research groups have joined both the theoretical and experimental investigation of the characteristics of photorefractive crystals[6-17]. Two charge transport models have been proposed, the "band transport model" by Kukhtarev et al.[6] and the "hopping model" by Feinberg et al.[7]. Both theories agree well with most experimental results. Most recently, a new photorefractive mechanism, the ϵ model, was proposed by Agranat and Yacoby[15-17].

Numerous applications using the photorefractive effect have been reported. These include holographic memories[9,10], coherent beam amplification[18-20], image processing[21-26] and generation of high reflectivity phase conjugation with low power lasers[27-28]. The author is responsible for the invention of a number of new devices which utilize the photorefractive effect. These include the self-starting and self-pumped multicolor phase conjugate mirrors(PPCM's)[29], wave front converters[30], optical path length to frequency conversion interferome-

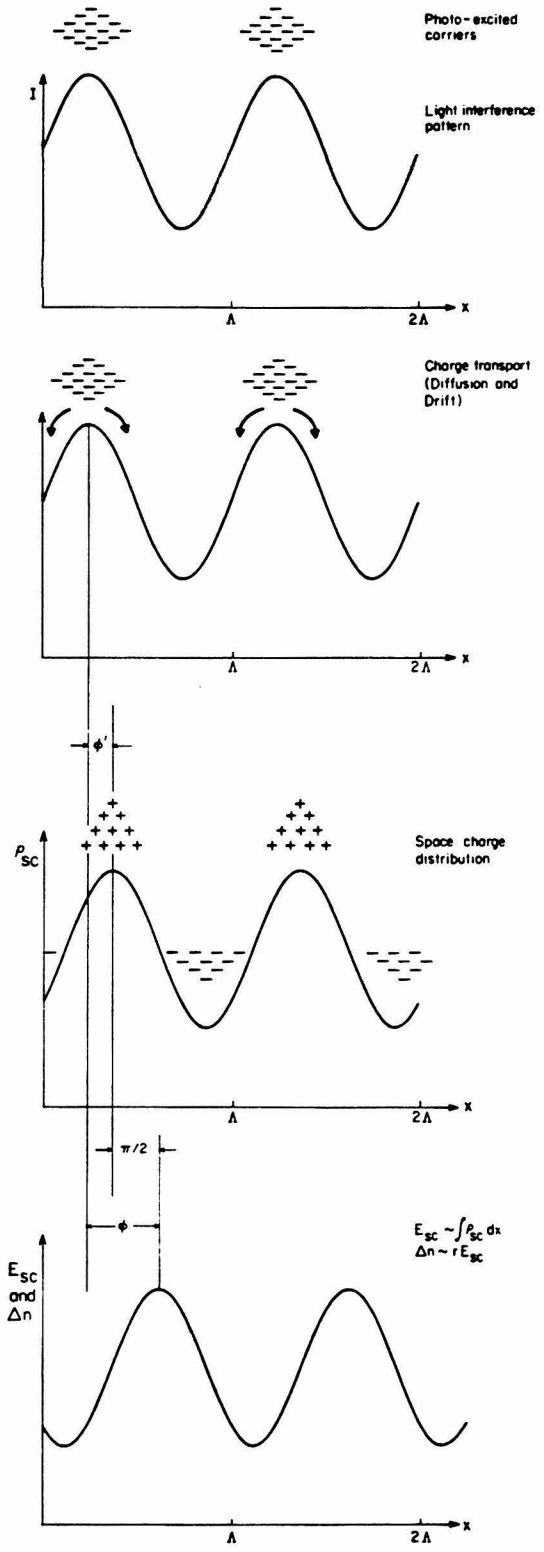

Fig. 1.1 : The photorefractive mechanism. Two coherent light beams intersect, forming an interference pattern. Charge is excited where the intensity is large and migrates to regions of low intensity. The electric field associated with the resultant space charge operates through the electrooptic coefficients to produce a refractive index grating. ϕ is the phase shift between the light interference pattern and the index grating.

ters[31—33], bistable devices[34,35], real image subtraction and differentiation devices[22,23] and associative memories[24-26]. All these devices will be discussed in detail in this thesis.

(1.2) Outline of the thesis

In Chapter 2, the band transport theory for the photorefractive effect is briefly reviewed. Some of the main results will be needed in the following chapters. The figures of merit useful in characterizing various photorefractive crystals are also discussed.

In Chapter 3, the coupled wave equations for two-wave mixing are derived and solved. The effects of energy coupling between the two interacting beams and the phase delay of each beam are discussed. These provide the basis for the discussions in the following chapters.

In chapter 4, the coupled wave formalism is extended to four-wave mixing in photorefractive crystals. Aspects of real-time holography and phase conjugation are discussed. The coupled wave equations are solved in two special cases: (1) single grating and undepleted pump approximation; and (2) single grating and negligible absorption. The theory is then compared with the experimental results. The solutions of the phase of phase conjugation are discussed. The recent developments in self-pumped phase conjugate mirrors are also discussed.

In Chapter 5, two new types of oscillators ultilizing the photorefractive gain are described and demonstrated. They are the unidirectional ring resonator, and the double phase conjugate resonator. Two applications, the optical path length to frequency conversion interferometer and one-way real time wave front converters, are also described.

In Chapter 6, two novel bistable devices using the self-pumped phase conjugate mirror are described. A threshold basis for the effect as well as the results of experimental demonstration are presented.

In Chapter 7, mathematical operations on images are discussed. Real time 'exclusive or' operation and image subtraction are experimentally demonstrated using an interferometer with a self-pumped phase conjugate mirror. Image differentiation as well as intensity inversion are also demonstrated.

In the last chapter, the theory and the experimental demonstration of all-optical associative holographic memory are discussed. Methods of extending the number of stored messages are also discussed.

References for Chapter One

1. A. Ashkin, G.D. Boyd, J.M. Dziedzic, R.G. Smith, A.A. Ballman, J.J. Levinstein and K. Nassau, Appl. Phys. Lett. **9**, 72, 1966.
2. F.S. Chen, J.T. LaMacchia and D.B. Fraser, Appl. Phys. Lett. **13**, 223, 1968.
3. F.S. Chen, J. Appl. Phys. **40**, 3389, 1969.
4. F.S. Chen, J. Appl. Phys. **38**, 3418, 1967.
5. J.J. Amodei, RCA Review, **32**, 185, 1971.
6. N.V. Kukhtarev, V.B. Markov, S.G. Odulov, M.S. Soskin and V.L. Vinetskii, Ferroelectrics, **22** pp. 949, 1979.
7. J. Feinberg, D. Heiman, A.R. Tanguay, Jr. and R.W. Hellwarth, J. Appl. Phys. **51** pp. 1297, 1980.
8. S.F. Su and T.K. Gaylord, J. Appl. Phys., **46**, 5208, 1975.
9. M. Peltier and F. Micheron, J. Appl. Phys. **48**, 3683, 1977.
10. M.G. Moharam and L. Young, J. Appl. Phys. **48**, 3230, 1977.
11. J.P. Huignard, J.P. Herriau, G. Rivet and P. Gunter, Opt. Lett. **5**, 102, 1980.
12. P. Günter, Phys. Rep. **93**, 200, 1983.
13. M. Cronin-Golomb, Ph.D. Dissertation (California Institute of Technology, Pasadena, California 1983, unpublished).
14. R.A. Mullen, Ph.D. Dissertation (University of Southern California, Los Angeles, California 1984, unpublished).
15. A. Agranat and Y. Yacoby, Phys. Rev. B, **27**, 5712, 1983.

16. A. Agranat and Y. Yacoby, Solid Stat. Comm., **52** 531, 1984.

17. A. Agranat and Y. Yacoby, Ferro. Lett., **4**, 19, 1985.

18. N.V. Kukhtarev, V.B. Markov, S.G. Odulov, M.S. Soskin and V.L. Vinetskii, Ferroelectrics, **22** pp. 961-964 (1979).

19. V.L. Vinetskii, N.V. Kukhtarev, S.G. Odulov and M.S. Soskin, Sov. Phys. Us, **22** 742 (1979).

20. F. Laeri, T. Tschudi, J. Albers, Opt. Comm. **47**, 387, 1983.

21. J.O. White and A. Yariv, Appl. Phys. Lett., **37**, 5, 1980.

22. S.-K. Kwong, G. Rakuljic and A. Yariv, Appl. Phys. Lett., **48**, 201, 1986.

23. S.-K. Kwong, G. Rakuljic, V. Leyva and A. Yariv, SPIE O-E'86, paper 613-07, 1986.

24. A. Yariv, S.-K. Kwong and K. Kyuma, Appl Phys. Lett., **48**, 1114, 1986.

25. A. Yariv, S.-K. Kwong and K. Kyuma, SPIE O-E LASE'86 Conference, paper 613-01, 1986.

26. A. Yariv and S.-K. Kwong, Opt. Lett., **11**, 186, 1986.

27. J. Feinberg, and R.W. Hellwarth, Opt. Lett. **5**, 519; Erratum Opt. Lett. **6**, 257, 1981.

28. M. Cronin-Golomb, B. Fischer, J.O. White and A. Yariv, IEEE J. **QE-20** 12-30 (1984).

29. M. Cronin-Golomb, S.-K. Kwong, and A. Yariv, Appl. Phys. Lett., **44**, 727, 1984.

30. S.-K. Kwong and A. Yariv, Appl. Phys. Lett., **48**, 564, 1986.

31. S.-K. Kwong, A. Yariv, M. Cronin-Golomb and I. Ury, Appl. Phys. Lett. **47** pp. 460-462 (1985).

32. S.-K. Kwong, M. Cronin-Golomb, B. Fischer, and A. Yariv, J. Opt. Soc. Am. **A3**, 157, 1986.

33. M. Cronin-Golomb, B. Fischer, S.-K. Kwong, J.O. White, and A. Yariv, Opt. Lett. **10**, 353, 1985.

34. S.-K. Kwong, M. Cronin-Golomb and A. Yariv, Appl. Phys. Lett. 45 1016 (1984).

35. S.-K. Kwong and A. Yariv, submitted to Opt. Lett.

Chapter 2: Charge transport in photorefractive crystals

(2.1) The band transport theory

In the Band transport theory, charge carriers are believed to move between trapping centers via a three-step process of photoexcitation, drift or diffusion in the conduction band, and recombination into a neighboring trapping center[1], see Fig. 2.1.

Let us consider the writing of a refractive index grating by two coherent beams intersecting in a slice of photorefractive medium sufficiently thin that the intensity modulation I_1 is constant. Suppose the intensity interference pattern, possibly in motion in the x direction, is given by

$$I(x) = I_+ + I_1 e^{i(kx+\Omega t)} + I_1^* e^{-i(kx+\Omega t)} \qquad [2.1]$$

The set of equations for determining the spatial distribution of the electric field that is responsible for modulating the refractive index is given in MKS units by

the continuity equation

$$\frac{\partial n}{\partial t} = \frac{\partial N_D^+}{\partial t} + \frac{1}{e}\frac{\partial j}{\partial x} \quad , \qquad [2.2]$$

the current equation

$$j = e\mu nE + \mu k_B T \frac{\partial n}{\partial x} \quad , \qquad [2.3]$$

the rate equation

$$\frac{\partial N_D^+}{\partial t} = \alpha_i I(N_D - N_D^+) - \gamma_R n N_D^+ \quad , \text{ and} \qquad [2.4]$$

Poisson's equation

$$\frac{\partial E}{\partial x} = \frac{e}{\epsilon}\,(n+N_A-N_D^+) \qquad [2.5]$$

where

$n(m^{-3})$ is the density of free (conduction band) electrons;

$N_D(m^{-3})$ is the total density of occupied and unoccupied donor sites;

$N_D^+(m^{-3})$ is the density of ionized donor sites;

$N_A(m^{-3})$ is the density of compensative acceptor sites;

$j(Am^{-2})$ is the current density in the conduction band;

$\mu(m^2/V/s)$ is the electron mobility;

$\epsilon(V/C/m)$ is the dc dielectric constant;

$\alpha_i(m^2)$ is the photo-ionization cross-section of the donor sites;

$\gamma_R(m^3/s)$ is the recombination coefficient of the acceptor sites;

$k_B(J/^oK)$ is the Boltzman's constant; and

$T(K^o)$ is the temperature.

When the modulation index of the light interference pattern is significantly less than one, then E, N_D^+, and n can be approximated by

$$E = E_o + E_1 e^{ikx} + E_1^* e^{-ikx} \qquad [2.6a]$$

$$N_D^+ = (N_D^+)_o + (N_D^+)_1 e^{ikx} + (N_D^+)_1^* e^{-ikx} \qquad [2.6b]$$

$$n = n_o + n_1 e^{ikx} + n_1^* e^{-ikx} \qquad [2.6c]$$

where E_1, $(N_D^+)_1$ and n_1 are the first order harmonics and are the functions of crystal parameters and of Ω. Higher order hamonics are important when the modulation index approaches unity[2,3]. By substituting Eq. [2.6] into [2.2]-[2.5], the result is[4]

$$[E_o+i(E_d+E_\mu)]t_o\frac{d(N_D^+)_1}{dt} = -(N_D^+)_1[E_o+i(E_d+E_q)] + m\,N_A e^{i\Omega t}(E_o+iE_d) \qquad [2.7]$$

where the characteristic time t_o is given by

$$t_o = N_A/(\alpha_i N_D I_+) \qquad [2.8]$$

where the characteristic fields are defined by

$$E_\mu = \frac{\gamma_R N_A}{\mu k} \quad \text{(drift field)} \qquad [2.9a]$$

$$E_d = \frac{k_B T k}{e} \quad \text{(diffusion field)} \qquad [2.9b]$$

$$E_q = \frac{eN_A}{\epsilon k} \quad \text{(space charge field)} \qquad [2.9c]$$

and the light modulation index m is defined as

$$m = \frac{I_1}{I_+}$$

The solution for $(N_D^+)_1$ is given by

$$\frac{(N_D^+)_1}{N_A} = \frac{m\,(E_o+iE_d)(e^{i\Omega t}-e^{-t/\tau})}{[E_o-\Omega t_o(E_d+E_\mu)] + i(E_d+E_q+\Omega t_o E_o)} \qquad [2.10]$$

where $\tau = t_o\,\dfrac{E_o+i(E_d+E_\mu)}{E_o+i(E_d+E_q)}$ [2.11]

Eqs. [2.10] and [2.11] are the main results. The space charge electric field and the index pattern can be calculated from Eq. [2.10].

(2.2) Figures of merit

In order to characterize and compare photorefractive crystals for

various applications, some figures of merit are defined. There are many figures of merit proposed in the literature[5-8]. Among these, the three most important ones are:

(a) Two-beam coupling constant; Γ (cm^{-1})

$$\Gamma = \frac{\cos\theta}{\ell} \ln \left[\frac{I_1(0)}{I_1(\ell)} \frac{I_2(\ell)}{I_2(0)} \right] \qquad [2.12]$$

where θ is the angle between the light beams and the z-axes, ℓ is the interaction length, and $I_1(0)$, $I_2(0)$, $I_1(\ell)$ and $I_2(\ell)$ are the light intensities of beams 1 and 2 at z=0 and z=ℓ, respectively. All these quantities can be measured in a the two-beam coupling experiment, see Fig. 2.2.

Γ gives a measure of energy transfer from beam 1 to beam 2. The above definition has the advantage of the successful elimination of the absorption coefficient due to the symmetry of the two interacting beams about the z-axis. However, if the two beams are not symmetric about the z-axis, some geometrical factors and the absorption coefficient must be taken into account. The dependence of Γ on the crystal parameters and interaction geometry will be further elaborated in Chapter 3, Eqs. [3.8] and [3.13].

(b) Response time constant; τ_o (J/cm^2)

$$\tau_o = tI_+ \Big/ \ln \left[\frac{\Gamma(\infty)}{\Gamma(\infty) - \Gamma(t)} \right] \qquad [2.13]$$

where $\Gamma(t)$ and $\Gamma(\infty)$ are the coupling constants, defined in Eq. [2,12], at time t and ∞, respectively. Eq. [2.13] is directly deduced from Eq.

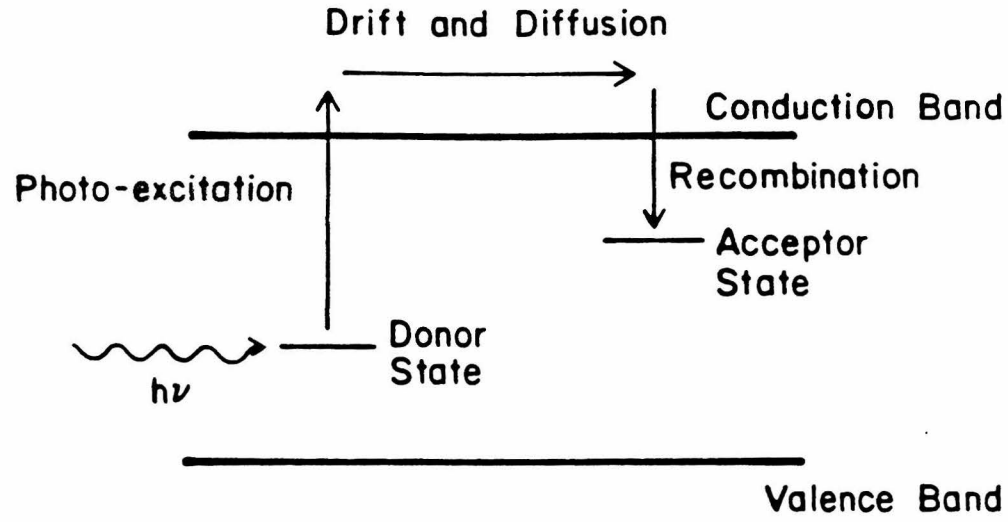

Fig. 2.1: Schematic diagram of the Band transport model.

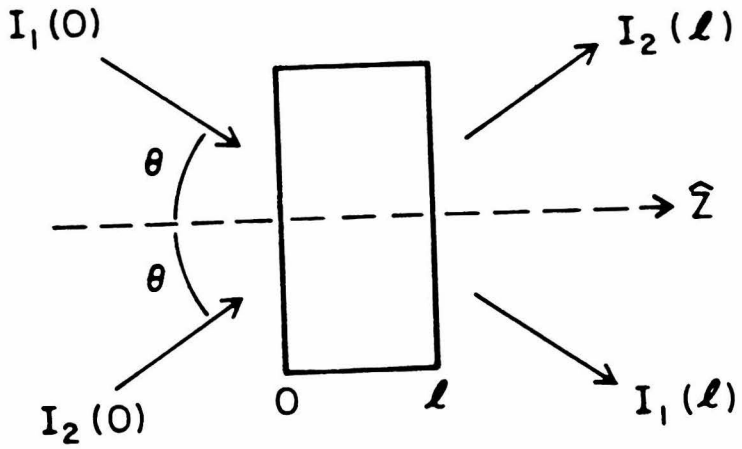

Fig. 2.2: Schematic diagram of a two-beam coupling experiment.

[2.10]. τ_o allows the comparison of the speed of the two beam coupling process with different experimental conditions on an equal basis. An expression relating τ_o to the crystal parameters and interaction geometry is given by Eqs. [2.8] and [2.11].

(c) Photorefractive sensitivity; S (cm^3/J)

$$S = \frac{\Delta n}{\alpha \tau I_+} \qquad [2.14]$$

The photorefractive sensitivity S is defined as the refractive index change per absorbed energy per unit volume[5]. It shows how well a material can utilize a given amount of optical energy. Alternatively, it compares materials with different absorption coefficients on an equal basis. Expression of Δn in terms of crystal parameters and interaction geometry is given in Eq. [3.4].

Based on these three figures of merit and some crystal parameters, other proposed figures of merit can be calculated. Table 2.1 give some experimentally measured figures of merit and crystal parameters of $BaTiO_3$, SBN, and BSO.

Table 2.1

	N_A	α (514nm)	Γ	τ_o	S
	(cm^{-3})	(cm^{-1})	(cm^{-1})	(J/m^2)	(cm^3/J)
BSO[9-11] (E_o=0)	10^{16}	1.6	1.4	16	3×10^{-3}
BSO[9-11] (E_o=10kV/cm)†	10^{16}	2.0	12	0.5	1
$BaTiO_3$[7,12,13] (E_o=0)	10^{16}	3.0	10	200	10^{-3}
SBN(undoped) (E_o=0)[7,8]	?	0.5	5	1000	10^{-2}
SBN:Ce[7,8] (E_o=0)	10^{16}	2.0	15	400	4×10^{-3}

† Optimum fringe speed was adjusted in these experiments.

References for Chapter Two

1. N.V. Kukhtarev, V.B. Markov, S.G. Odulov, M.S. Soskin and V.L. Vinetskii, Ferroelectrics, **22** pp. 949, 1979.

2. M.P. Petrov, S.V. Miridonov, S.I. Stepanov and V.V. Kulikov, Opt. Comm. **31**, 301, 1979.

3. E. Ochoa, F. Vachss and L. Hesselink, J. Opt. Soc. Am. A **3**, 181, 1986.

4. M. Cronin-Golomb, Ph.D. Dissertation (California Institute of Technology, Pasadena, California 1983, unpublished).

5. A.M. Glass, Opt. Eng., **17**, 470, 1978.

6. G.C. Valley, and M.B. Klein, Opt. Eng. **22**, 704, 1983.

7. G.A. Rakuljic, A. Yariv, and R. Neurgaonkar, SPIE O-E LASE'86 Conference, Los Angeles, 1986, paper 613-19.

8. G.A. Rakuljic, A. Yariv, and R. Neurgaonkar, to be published in Opt. Eng., 1986.

9. Ph. Refregier, L. Solymar, H. Rajbenbach, and J.P. Huignard, J. Appl. Phys. **58**, 45, 1985.

10. R.A. Mullen, and R.W. Hellwarth, J. Appl. Phys. **58**, 40, 1985.

11. S.L. Hou, R.B. Lauer, and R.E. Aldrich, J. Appl. Phys. 44,2652, 1973.

12. G.C. Valley, IEEE J. Quant. Electron. **QE-19**, 1637, 1983.

13. J. Feinberg, D. Heiman, A.R. Tanguay, Jr. and R.W. Hellwarth, J. Appl. Phys. **51** pp. 1297, 1980.

Chapter 3: Two Wave Mixing in Photorefractive Crystals

In chapter 2, we discussed the photorefractive crystals as dynamic holographic media. The main results were: (1) they are reusable volume refractive index holograms, and (2) in general, there is a phase shift between the light interference pattern and the index grating which causes energy coupling between the two interacting beams. Both of these effects are different from fixed volume holograms such as photographic emulsions, dichromated gelatin[1], photopolymer materials[2], and photorefractive crystals that have been fixed after recording[3]. The coupled wave theory for fixed volume hologram has also been developed in 1969 by Kogelnik[4].

In this chapter, the basic results of two-beam interaction in photorefractive crystals are reviewed. This review will serve as the basis for the discussion of four wave mixing in Chapter 4, photorefractive resonators in Chapter 5, and various applications and devices in Chapters 6 to 8.

(3.1) The coupled wave theory

Refering to the configuration shown in Fig. 3.1, Beam 1 and beam 2 are plane waves. They have the same polarization and their optical electric field can be written as

$$\vec{E}_j = A_j(\vec{r})\ \exp[i(\vec{k}_j\cdot\vec{r}-\omega_j t)] + c.c. \qquad j=1,2 \qquad [3.1]$$

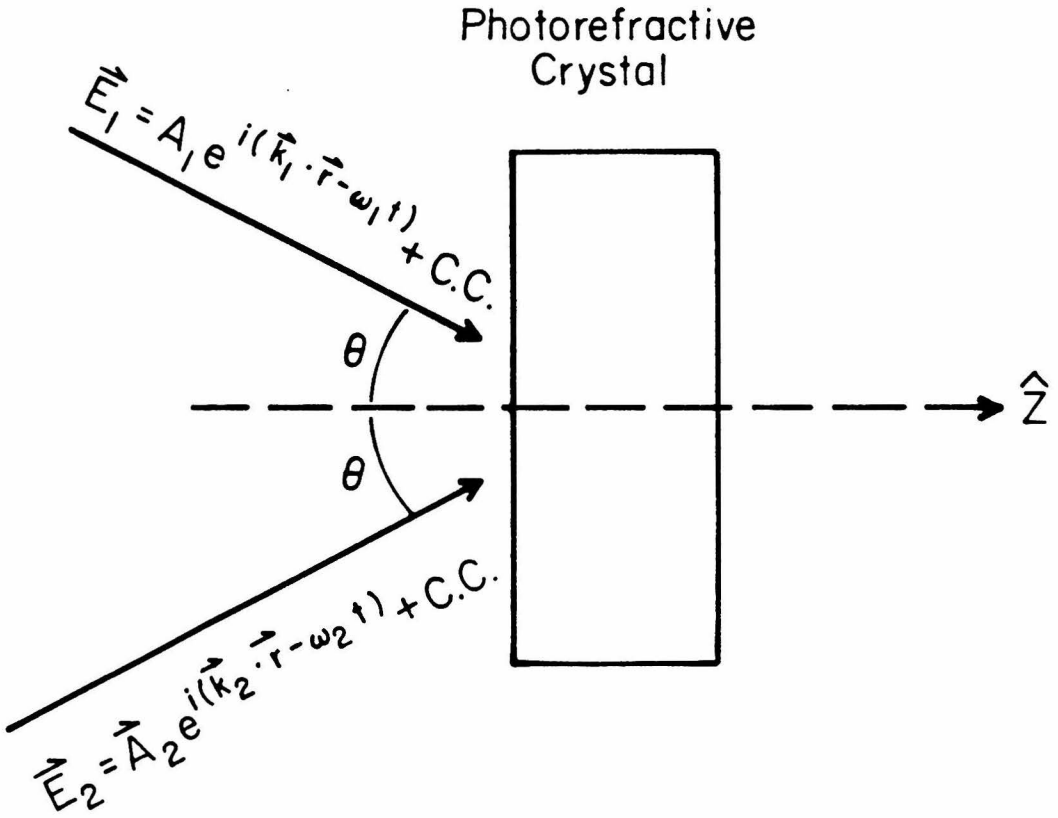

Fig. 3.1: A schematic diagram of two-wave mixing in photorefractive crystals.

These two coherent beams write a interference pattern which gives rise to a refractive index variation through the photorefractive effect.

$$n = n_o + n_1 e^{-i\phi} \frac{A_1 A_2^*}{I_+} e^{-i(\vec{k}_1-\vec{k}_2)\cdot\vec{r}} + n_1 e^{i\phi} \frac{A_1^* A_2}{I_+} e^{i(\vec{k}_2-\vec{k}_1)\cdot\vec{r}} \qquad [3.2]$$

where $I_+=I_1+I_2$ is the total intensity, and

$$I_j = |A_j|^2 \quad \text{and} \quad A_j = |A_j|\exp[i\psi_j] , \qquad j=1,2 \qquad [3.3]$$

From the photorefractive theory developed in chapter 2, the index grating amplitude is given by

$$n_1 e^{i\phi} = \frac{r_{eff}\, n_o^3}{2} \frac{iE_q(E_o+iE_d)}{\left[E_o-(\omega_2-\omega_1)t_o(E_d+E_\mu)\right] + i\left[E_d+E_q+(\omega_2-\omega_1)t_o E_o\right]} \qquad [3.4]$$

where r_{eff} is the relevant electro-optic coefficient, n_o is the ordinary refractive index of the crystal, and ϕ is the phase shift between the light interference pattern and the index grating.

Substituting this index variation, Eq. [3.2], into the scalar wave equation

$$\nabla^2 E + k^2 E = 0 \qquad [3.5]$$

and using the slowly varying field approximation[5]

$$\left| \frac{d^2 A_j}{dz^2} \right| << k \left| \frac{dA_j}{dz} \right| \qquad [3.6]$$

the coupled wave equations,

$$\frac{dA_1}{ds} = -\frac{\gamma}{I_+}(A_1A_2^*)A_2 - \frac{\alpha}{2}A_1 \qquad [3.7a]$$

$$\frac{dA_2}{ds} = \frac{\gamma^*}{I_+}(A_1^*A_2)A_1 - \frac{\alpha}{2}A_1 \qquad [3.7b]$$

are obtained, where

$$s = z/\cos\theta$$

$$\gamma = \frac{i\omega n_1 e^{-i\phi}}{2c} \quad , \qquad [3.8]$$

When there is no applied electric field, i.e. E_o=0,

$$\gamma = \frac{\gamma_o}{1 + i(\omega_2-\omega_1)\tau} \qquad [3.9]$$

where

$$\gamma_o = \frac{r_{eff}\, n_o^s}{4}\,\frac{\omega}{c}\,\frac{E_q E_d}{(E_q+E_d)} \qquad [3.10]$$

and

$$\tau = t_o\left[\frac{E_d+E_\mu}{E_d+E_q}\right] \qquad [3.11]$$

θ is the angle between the beams and the z-axis and α is the intensity absorption coefficient. In most practical situations $(\omega_2-\omega_1)/\omega_1 < 10^{-14}$, because if the frequency difference is too large, the response of the crystal is not fast enough to follow the moving light interference pattern. Therefore, ω_1 and ω_2 can be accurately replaced by $\omega \simeq \omega_2 \simeq \omega_1$ except in Eq. [3.4] and [3.9]. This approximation will be justified in section 5.1.

The first term of the right side of Eq. [3.7] represents the contribution from self-diffraction and the second term represents the linear aborption in the crystal. Eq. [3.7] can be decomposed into

intensity and phase equations for each beam:

$$\frac{dI_1}{ds} = -\Gamma \frac{I_1 I_2}{I_+} - \alpha I_1 \qquad [3.12a]$$

$$\frac{dI_2}{ds} = \Gamma \frac{I_1 I_2}{I_+} - \alpha I_2 \qquad [3.12b]$$

$$\frac{d\psi_1}{ds} = -\Gamma' \frac{I_2}{I_+} \qquad [3.12c]$$

$$\frac{d\psi_2}{ds} = -\Gamma' \frac{I_1}{I_+} \qquad [3.12d]$$

where $\Gamma = 2\mathrm{Re}[\gamma]$ and $\Gamma' = \mathrm{Im}[\gamma]$. [3.13]

From Eq. [3.12], note that the intensity coupling is due to the real part of the coupling constant γ, and the phase delay is due to the imaginary part of γ. The phase delay is independent of $\alpha\ell$ and always equal to zero when ϕ equal to $\pi/2$.

(3.2) Solutions to the coupled wave equations

Eq. [3.12] can be solved[6] using the boundary conditions $|A_j(0)|\exp[i\psi_j(0)]$, j=1,2

$$I_1(s) = \frac{I_+(0)e^{-\alpha s}}{1+(I_2(0)/I_1(0))e^{\Gamma s}} \qquad [3.14a]$$

$$I_2(s) = \frac{I_+(0)e^{-\alpha s}}{1+(I_1(0)/I_2(0))e^{-\Gamma s}} \qquad [3.14b]$$

$$\psi_1(s) = \psi_1(0) - \Gamma' s + \frac{\Gamma'}{\Gamma} \ln\left[\frac{1+I_1(0)/I_2(0)}{1+(I_1(0)/I_2(0))e^{-\Gamma s}}\right] \qquad [3.14c]$$

$$\psi_2(s) = \psi_2(0) - \Gamma' s - \frac{\Gamma'}{\Gamma} \ln\left[\frac{1+I_2(0)/I_1(0)}{1+(I_2(0)/I_1(0))e^{\Gamma s}}\right] \qquad [3.14d]$$

Eqs. [3.14a] and [3.14b] describe the coherent optical gain for beam 2 and loss for beam 1, when $\Gamma\ell$ is positive. A coherent optical amplifier can be built based on this principle. Typical Input/Output curves for such amplifiers are shown in Fig. 3.2 for the case of $\alpha\ell=0$. In the region of very small signal to pump ratio, $I_1(0)\gg I_2(0)$, the differential gain is very large.

Eqs. [3.14c] and [3.14d] describe the phase delay (or advance) of beam 2 due to the nonlinear interaction. In Fig. 3.3, the phase shift of beam 2, $\psi_2(\ell)-\psi_2(0)$, is plotted against the phase shift between the index grating and the light interference pattern, ϕ. A similar set of curves for $\psi_1(\ell)-\psi_1(0)$ versus ϕ can be readily obtained by replacing ϕ with $-\phi$ and r by 1/r in Fig. 3.3, where $r=I_2(0)/I_1(0)$.

The noise in the conventional population inversion gain medium is due to spontaneous emission. In the photorefractive gain medium, the noise is not due to spontaneous emission but is due to random thermal excitation, background illumination, and scattering from crystal defects.

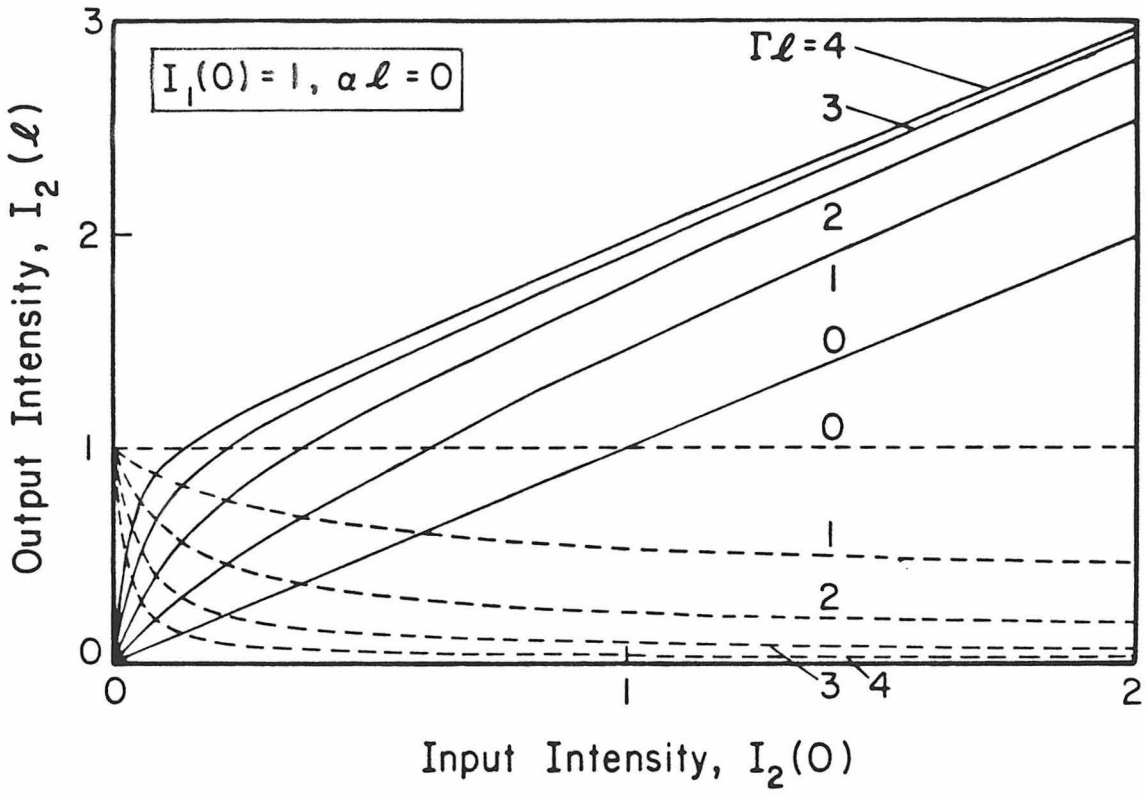

Fig. 3.2: Input/Output characteristic curves for a coherent amplifier using photorefractive two-wave mixing. The intensity of the pump beam $I_1(0)$ is fixed at 1 (arbitrary units). The dashed curves correspond to the deamplified beam $I_1(\ell)=1+I_2(0)-I_2(\ell)$. $\alpha\ell$ is zero.

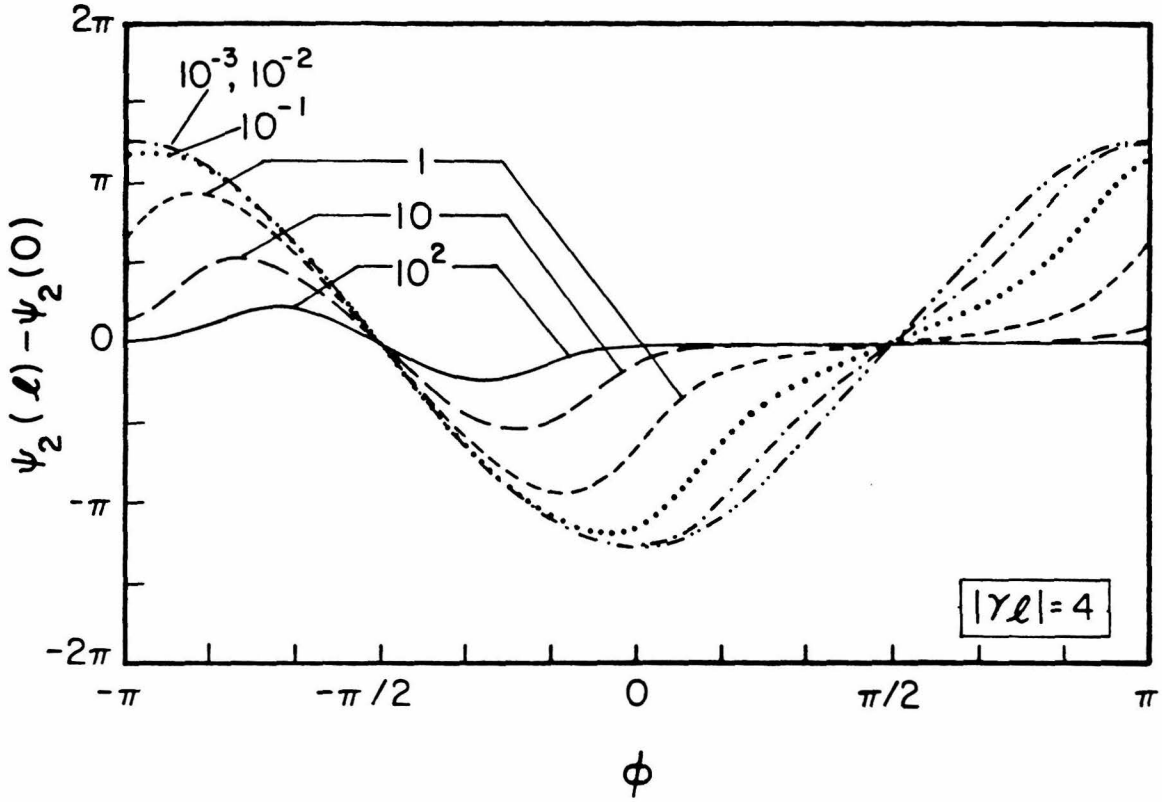

Fig. 3.3: The phase shift of beam 2, $\psi_2(\ell)-\psi_2(0)$, versus the phase shift between the index grating and the light interference pattern, ϕ, see Eq. [3.14d].

References for Chapter 3

1. T. Shankoff, Appl. Opt. **7**, 2101, 1968.

2. D.H. Close, A.D. Jacobson, J.D. Margerum, R.G. Brault and F.J. McClung, Appl. Phys. Lett. **14**, 159, 1969.

3. D.L. Staebler, W.J.Burke, W. Phillips and J.J. Amodei, Appl. Phys. Lett. **26**, 182, 1975.

4. H. Kogelnik, Bell Syst. Tech. J. **48**, 2909, 1969.

5. A. Yariv, Quantum Electronics, (Wiley, New York, 1975)

6. D.W. Vahey, J. Appl. Phys. **46**, 3510, 1975.

Chapter 4: Four-Wave Mixing and Phase Conjugation

In this chapter, the holographic formulation of four-wave mixing is discussed. It is an extension of the two-wave mixing formulism presented in Chapter 3. Four-wave mixing in a nonlinear media is one of the most frequently used techniques of generating phase conjugate beam since it does not have the restrictive phase matching requirement of three wave mixing. In Section 4.1, the formal analogy between four-wave mixing and real time holography is presented. In Section 4.2 a coupled wave theory of four-wave mixing in photorefractive crystals is described. The solution of the coupled wave equations is summarized in Section 4.3. Experiments to verify this theory have been performed giving results which are summarized in Section 4.4. Analytic expressions for the phase of the phase conjugate beam are also presented in Section 4.5. Recent development in self-pumped phase conjugators using photorefractive crystals are discussed in Sections 4.6.

(4.1) Four-wave mixing and real time holography

To set the stage for the present discussion, let us first consider conventional holography[1]. It consists of two steps, the first (the recording) is illustrated in Fig. 4.1a, where A_1 and A_4 are the complex amplitudes of the reference beam and the object beam at the hologram plane respectively. The resulting transmission function of the hologram is

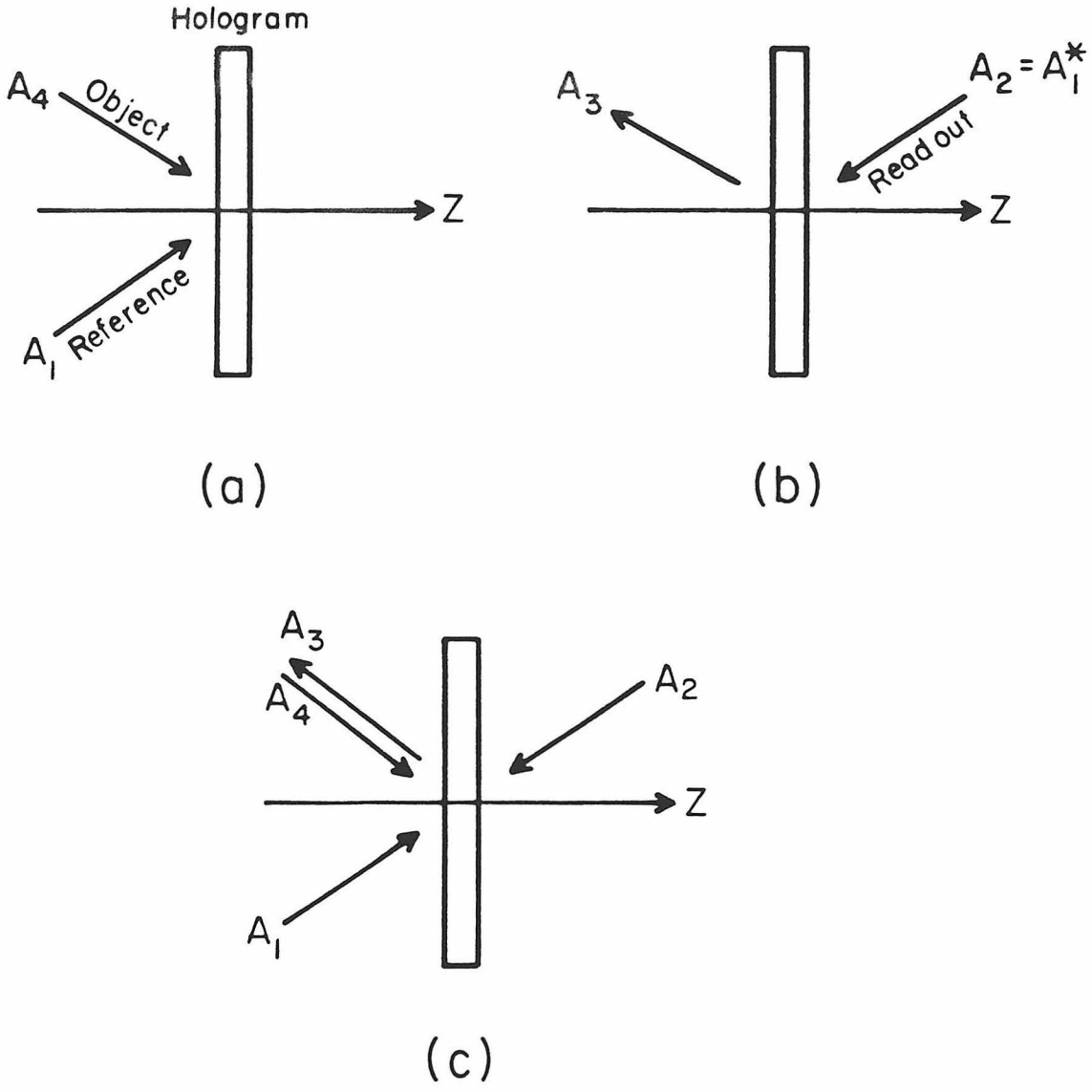

Fig. 4.1 : (a) Recording a hologram; (b) Reconstruction step; (c) real time holography.

$$T \propto (A_4 + A_1)(A_4^* + A_1^*) = |A_4|^2 + |A_1|^2 + A_4A_1^* + A_1A_4^* \qquad [4.1]$$

In the reconstruction step, the hologram is illuminated by a single reference wave A_2 impinging from the right in a direction opposite to that of A_1 as shown in Fig. 4.1b. The diffracted field to the left of the hologram is

$$A_3 = TA_2 \propto (|A_4|^2 + |A_1|^2)A_2 + A_4A_1^*A_2 + A_1A_2A_4^* \qquad [4.2]$$

The first term on the right side of [4.2] is proportional to the incident field A_2 and is of no interest here. The term $A_4A_1^*A_2$ in a thick hologram will have a phase factor $\exp[-i(\vec{k}_1-\vec{k}_2-\vec{k}_4)\cdot\vec{r}]$ and is thus phase mismatched, i.e. will not radiate. The term of interest is

$$A_3 \propto A_1A_2A_4^* \qquad [4.3]$$

In particular if A_1 and A_2 are counter-propagating plane waves, then A_3 will become the phase conjugate replica of the original object field A_4 at $z<0$ [2]. The phase matching condition for the generation of phase conjugate waves is the same as the Bragg condition for a hologram. If the recording medium is a dynamic hologram, such as a photorefractive crystal, the recording and the reconstruction processes in Fig. 4.1a and 4.1b can be combined simultaneously to perform the real time holography in Fig. 4.1c.

(4.2) Coupled wave equations

The basic interaction geometry is shown in Fig. 4.2. The four interacting beams have the same polarization and are mutually coherent. Let the electric field amplitude associated with the j-th

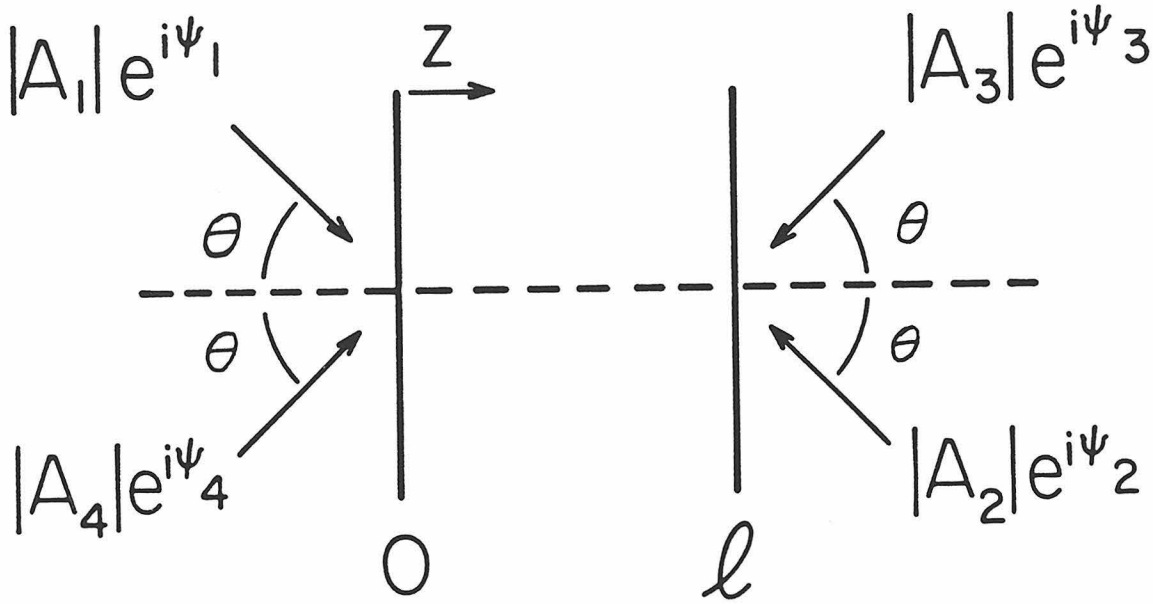

Fig. 4.2 : A schematic diagram of nonlinear four-wave mixing in a nonlinear medium. A_1 and A_2 are the pumping beams, A_3 is the phase conjugate output and A_4 is the probe beam.

beam be

$$E_j(\vec{r},t) = A_j(\vec{r})\exp[i(\vec{k}_j\cdot\vec{r}-\omega t)] + c.c. \qquad j=1,..,4 \qquad [4.4]$$

There are four possible sets of index gratings,

$$\vec{k}_I = \vec{k}_4-\vec{k}_1 = \vec{k}_2-\vec{k}_3 \qquad [4.5a]$$

$$\vec{k}_{II} = \vec{k}_1-\vec{k}_3 = \vec{k}_4-\vec{k}_2 \qquad [4.5b]$$

$$\vec{k}_{III} = \vec{k}_1-\vec{k}_2 \qquad [4.5c]$$

$$\vec{k}_{IV} = \vec{k}_4-\vec{k}_3 \qquad [4.5d]$$

These gratings are shown in Fig. 4.3. The photo-induced index variation is[3-5]

$$n = n_o + \frac{n_I e^{i\phi_I}}{2}\frac{A_1^*A_4+A_2A_3^*}{I_+}e^{i\vec{k}_I\cdot\vec{r}} + \frac{n_{II}e^{i\phi_{II}}}{2}\frac{A_1A_3^*+A_2^*A_4}{I_+}e^{i\vec{k}_{II}\cdot\vec{r}}$$
$$+ \frac{n_{III}e^{i\phi_{III}}}{2}\frac{A_1A_2^*}{I_+}e^{i\vec{k}_{III}\cdot\vec{r}} + \frac{n_{IV}e^{i\phi_{IV}}}{2}\frac{A_3^*A_4}{I_+}e^{i\vec{k}_{IV}\cdot\vec{r}} + c.c. \qquad [4.6]$$

Substituting this index variation into the scalar wave equation, Eq. [3.5], and using the slowly varying field approximation, Eq. [3.6], the following coupled wave equations are obtained

$$\cos\theta_1\frac{dA_1}{dz} = -i\frac{\pi n_I}{\lambda}e^{-i\phi_I}\frac{A_1A_4^*+A_2^*A_3}{I_+}A_4 - i\frac{\pi n_{II}}{\lambda}e^{i\phi_{II}}\frac{A_1A_3^*+A_2^*A_4}{I_+}A_3$$
$$- i\frac{\pi n_{III}}{\lambda}e^{i\phi_{III}}\frac{A_1A_2^*}{I_+}A_2 - \frac{\alpha}{2}A_1 \qquad [4.7a]$$

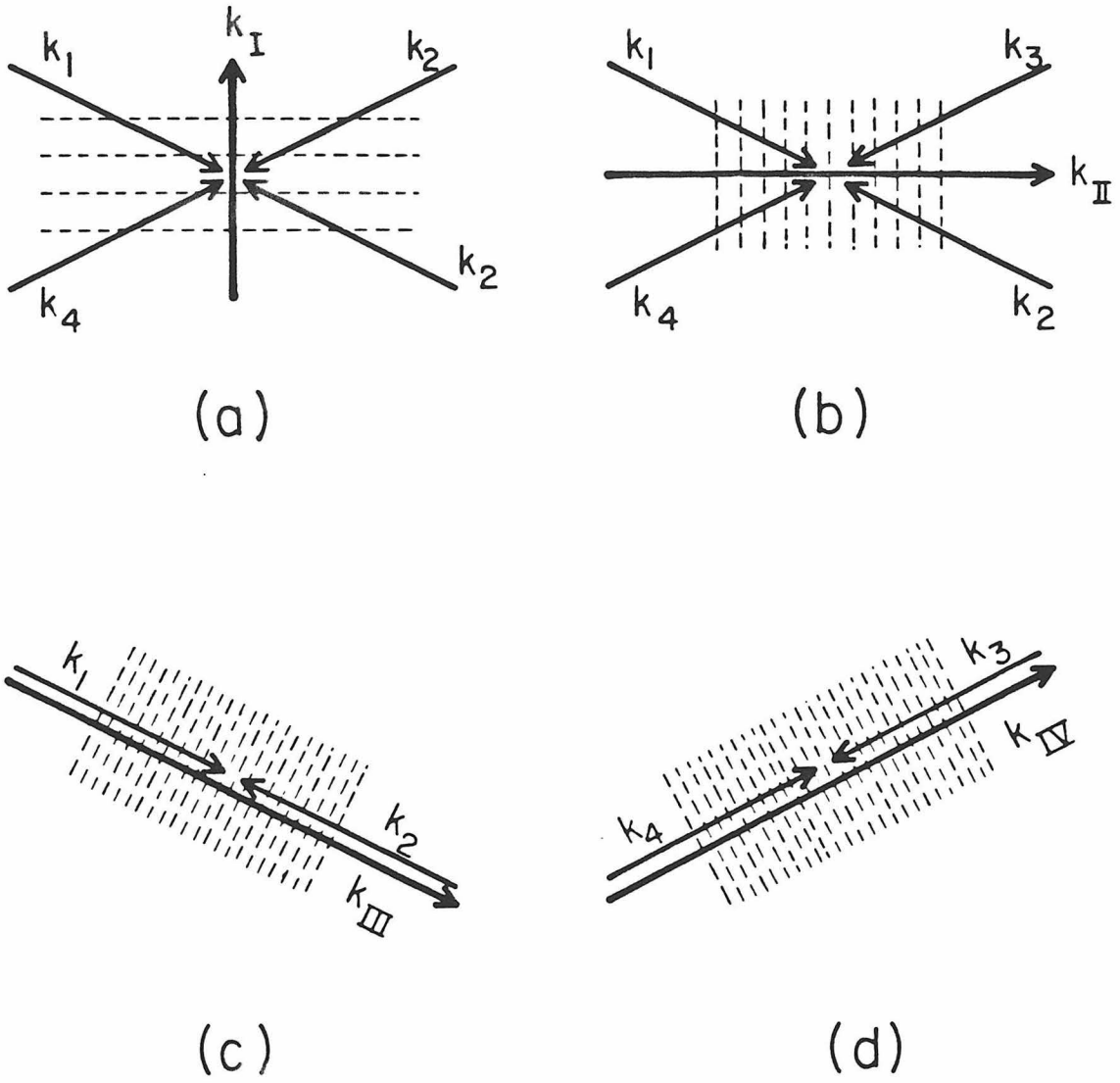

Fig. 4.3 : Schematic diagram of the four grating vectors.

$$\cos\theta_1 \frac{dA_2}{dz} = i\frac{\pi n_I}{\lambda} e^{i\phi_I} \frac{A_1^* A_4 + A_2 A_3^*}{I_+} A_3 + i\frac{\pi n_{II}}{\lambda} e^{-i\phi_{II}} \frac{A_1^* A_3 + A_2 A_4^*}{I_+} A_4$$

$$+ i\frac{\pi n_{III}}{\lambda} e^{-i\phi_{III}} \frac{A_1^* A_2}{I_+} A_1 + \frac{\alpha}{2} A_2 \qquad [4.7b]$$

$$\cos\theta_2 \frac{dA_1}{dz} = i\frac{\pi n_I}{\lambda} e^{-i\phi_I} \frac{A_1 A_4^* + A_2^* A_3}{I_+} A_2 + i\frac{\pi n_{II}}{\lambda} e^{-i\phi_{II}} \frac{A_1^* A_3 + A_2 A_4^*}{I_+} A_1$$

$$+ i\frac{\pi n_{IV}}{\lambda} e^{-i\phi_{IV}} \frac{A_3 A_4^*}{I_+} A_4 + \frac{\alpha}{2} A_3 \qquad [4.7c]$$

$$\cos\theta_2 \frac{dA_2}{dz} = -i\frac{\pi n_I}{\lambda} e^{i\phi_I} \frac{A_1^* A_4 + A_2 A_3^*}{I_+} A_1 - i\frac{\pi n_{II}}{\lambda} e^{i\phi_{II}} \frac{A_1 A_3^* + A_2^* A_4}{I_+} A_2$$

$$- i\frac{\pi n_{IV}}{\lambda} e^{i\phi_{IV}} \frac{A_3^* A_4}{I_+} A_3 - \frac{\alpha}{2} A_4 \qquad [4.7d]$$

$$\text{where } I_+ = \sum_{j=1}^{4} |A_j|^2 \qquad [4.8]$$

If there are only two beams involved in the interaction, Eq. [4.7] will then reduce to the two-wave mixing equations of Eq. [3.7].

A complete analytical solution to this set of nonlinear coupled equations is not presently available. Some numerical solutions have been obtained recently by assuming that only two of the four sets of gratings are present in the interaction[6]. However if we assume that only one grating is important, then Eq. [4.7] can be solved analytically in two cases: (a) with the undepleted pumps approximation, i.e. I_1, $I_2 \gg I_3$, I_4; and (b) without absorption. Predominance of one

grating is common in most experimental situations due to the directions, polarizations, and coherence relationships of the four beams relative to the nonlinear medium and to the application, in some cases, of an electric field which enhances certain gratings.

(4.3a) Single grating, undepleted pump approximation

The transmission grating is chosen because it matches the experimental geometry to be described in Section 4.3. In the undepleted pumps approximation, Eq. [4.7] becomes

$$\frac{dA_1}{ds} = -\frac{\alpha}{2} A_1 \qquad [4.9a]$$

$$\frac{dA_2}{ds} = \frac{\alpha}{2} A_2 \qquad [4.9b]$$

$$\frac{dA_3}{ds} = \frac{\alpha}{2} A_3 + \gamma \frac{A_1 A_4^* + A_2^* A_3}{I_+} A_2 \qquad [4.9c]$$

$$\frac{dA_4^*}{ds} = -\frac{\alpha}{2} A_4^* + \gamma \frac{A_1 A_4^* + A_2^* A_3}{I_+} A_1^* \qquad [4.9d]$$

where γ and s are defined in Eq. [3.8] (assume $\theta_1 = \theta_2$). With boundary conditions, $A_1(0)$, $A_2(\ell)$, $A_3(\ell)=0$ and $A_4^*(0)$ are known, the solutions of [4.9] are[7]

$$A_1(s) = A_1(0)\, e^{-\alpha/2 s} \qquad [4.10a]$$

$$A_2(s) = A_2(\ell)\, e^{\alpha/2(s-\ell)} \qquad [4.10b]$$

$$A_3(s) = -\frac{A_2(\ell) A_4^*(0)\, e^{\alpha/2(s-\ell)+\gamma s}}{A_1^*(0)} \frac{J(s)}{J(0)-1} \qquad [4.10c]$$

$$A_4^*(s) = -A_4^*(0)\, e^{-\alpha/2 s+\gamma s} \left[\frac{J(s) - e^{-\gamma s}}{J(0)-1} \right] \qquad [4.10d]$$

where

$$J(s) = \int_{\gamma s}^{\gamma \ell} \frac{\exp(-x)\, dx}{1 + r\, e^{-\alpha' \gamma \ell} \exp(2\alpha' x)} \qquad [4.11]$$

where r is the pump ratio $I_2(\ell)/I_1(0)$ and α' is the normalized linear absorption α/γ. The phase conjugate reflection coefficient is thus

$$\rho = \frac{A_3(0)}{A_1^*(0)} = - \frac{A_2(\ell)}{A_1^*(0)} \frac{J(0) e^{-\alpha \ell/2}}{J(0)-1} \qquad [4.12]$$

When the absorption is negligibly small, the integral in Eq. [4.13] can be performed explicitly. The phase conjugate reflection coefficient is[3]

$$\rho(\alpha \to 0) = - \left[\frac{A_1 A_2}{A_1^* A_2^*} \right]^{1/2} \frac{\sinh \left(\frac{1}{2} \gamma \ell \right)}{\cosh \left(\frac{1}{2} \gamma \ell + \frac{1}{2} \ln r \right)} \qquad [4.13]$$

A plot of phase conjugate reflectivity, $R=|\rho|^2$, versus pump ratio at various absorptions values $\alpha\ell$ is shown in Fig. 4.4.

(4.3b) Single grating, no absorption

With only the transmission grating present and no absorption, Eq [4.7] becomes

$$\frac{dA_1}{ds} = \frac{-\gamma}{I_+} (A_1 A_4^* + A_2^* A_3) A_4, \qquad [4.14a]$$

$$\frac{dA_2^*}{ds} = \frac{-\gamma}{I_+} (A_1 A_4^* + A_2^* A_3) A_3^*, \qquad [4.14b]$$

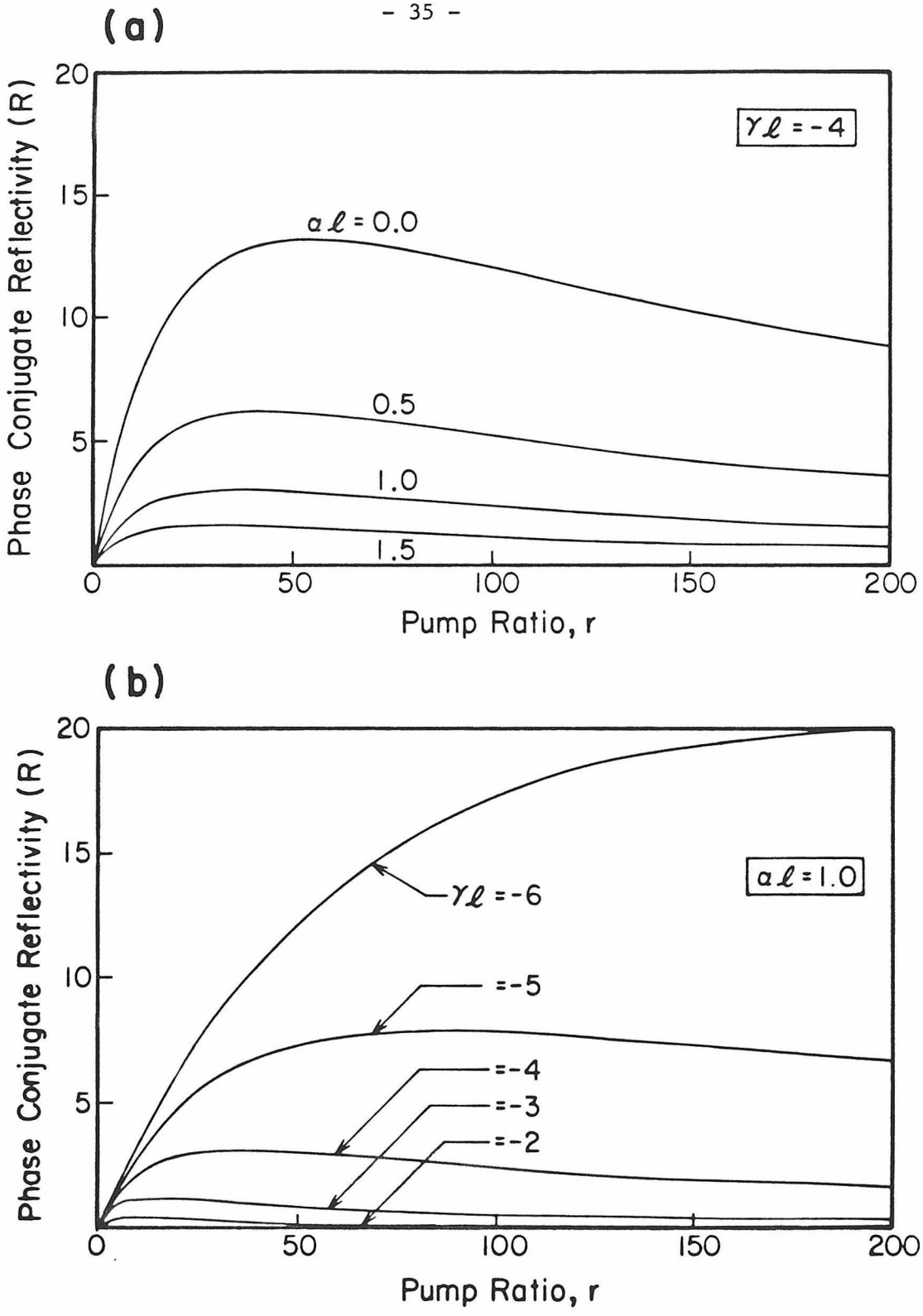

Fig. 4.4 : (a) Phase conjugate reflectivity, R, versus pump ratio, r, for various absorption $\alpha\ell$ and at $\gamma\ell$=-4 in undepleted pump approximation. (b) R vs. r for various $\gamma\ell$ and at $\alpha\ell$=1.0.

$$\frac{dA_3}{ds} = \frac{\gamma}{I_+}(A_1A_4^* + A_2^*A_3)A_2, \qquad [4.14c]$$

$$\frac{dA_4^*}{ds} = \frac{\gamma}{I_+}(A_1A_4^* + A_2^*A_3)A_1 \qquad [4.14d]$$

The boundary conditions for common laboratory phase conjugation experiments are: $I_1(0)$, $I_2(\ell)$, $I_3(\ell)=0$ and $I_4(0)$ are known. The solutions to Eq. [4.14] are[7,8]

$$I_1(s) = I_{12}(s)\,\frac{d_2 - I_{34}(s)\,d_1}{1 - I_{12}(s)\,I_{34}(s)} \qquad [4.15a]$$

$$I_2(s) = \frac{d_2 - I_{34}(s)\,d_1}{1 - I_{12}(s)\,I_{34}(s)} \qquad [4.15b]$$

$$I_3(s) = I_{34}(s)\,\frac{d_1 - I_{12}(s)\,d_2}{1 - I_{12}(s)\,I_{34}(s)} \qquad [4.15c]$$

$$I_4(s) = \frac{d_1 - I_{12}(s)\,d_2}{1 - I_{12}(s)\,I_{34}(s)} \qquad [4.15d]$$

and the phase conjugate reflectivity is

$$R = \frac{I_3(0)}{I_4(0)} = \frac{4|c|^2|T|^2}{|\Delta T + (\Delta^2 + 4|c|^2)^{1/2}|^2} \qquad [4.16]$$

where

$$d_1 = I_1(0) + I_4(0) \qquad [4.17a]$$

$$d_2 = I_2(\ell) \qquad [4.17b]$$

$$I_{12}(s) = \frac{I_1(s)}{I_2(s)} = \left| \frac{S_-De^{-\mu s} - S_+D^{-1}e^{\mu s}}{2c^*(De^{-\mu s} - D^{-1}e^{\mu s})} \right|^2 \qquad [4.18a]$$

$$I_{34}(s) = \frac{I_3(s)}{I_4(s)} = \left| \frac{S_-Ee^{-\mu s} - S_+E^{-1}e^{\mu s}}{2c^*(Ee^{-\mu s} - E^{-1}e^{\mu s})} \right|^2 \qquad [4.18b]$$

$$\Delta = d_1 - d_2 \qquad [4.19a]$$

$$Q = (\Delta^2 + 4|c|^2)^{1/2} \qquad [4.19b]$$

$$S_{\pm} = \Delta \pm Q \qquad [4.19c]$$

$$\mu = \gamma Q/2I_+ \qquad [4.19d]$$

$$T = \tanh \mu\ell \qquad [4.19e]$$

$$D = \left[\frac{S_+ + 2|c|^2/I_2(\ell)}{S_- + 2|c|^2/I_2(\ell)} \right]^{1/2} e^{\mu\ell} \qquad [4.20a]$$

$$E = \left[\frac{S_+}{S_-} \right]^{1/2} e^{\mu\ell} \qquad [4.20b]$$

$|c|^2$ is given by the equation

$$\left[|c|^2 - I_1(0)I_2(\ell) \right] \left| \Delta T + (\Delta^2 + 4|c|^2)^{1/2} \right|^2 + 4|c|^2|T|^2 I_4(0)I_2(\ell)$$

$$+ 2|c|^2 I_4(0)(\Delta^2 + 4|c|^2)^{1/2}(T+T)^* = 0 \qquad [4.21]$$

When considering the phase conjugate reflectivity as a funtion of the various input beam intensities, it is convenient to define two parameters:

the probe ratio q

$$q \equiv \frac{I_4(0)}{I_1(0) + I_2(\ell)} \qquad [4.22a]$$

and the pump ratio

$$r = \frac{I_2\gamma(\ell)}{I_1(0)} \qquad [4.22b]$$

These two parameters are sufficient to describe the input beams. In

terms of these parameters we have

$$I_1(0) = \frac{I_+}{(r+1)(q+1)} \qquad [4.23a]$$

$$I_2(\ell) = \frac{rI_+}{(r+1)(q+1)} \qquad [4.23b]$$

$$I_4(0) = \frac{qI_+}{(q+1)} \qquad [4.23c]$$

A contour plot of phase conjugate reflectivity for $\gamma\ell$=-3, as a function of both pump and probe ratios is shown in Fig. 4.5.[7] In some regions, there exist multiple solutions which are the result of the nonuniqueness of the solution to Eq. [4.21] for a certain range of parameters. Futher discussion of multiple solutions will be given in Section 4.5.

(4.4) Experimental studies of four wave mixing and phase conjugation

My experimental studies of four-wave mixing in both photorefractive barium titanate $BaTiO_3$ and strontium barium niobate $Sr_{0.6}Ba_{0.4}Nb_2O_6$ (SBN) crystals are described in this section. The experimental results are compared with the theoretical predictions from the coupled wave theory described in the last section. Three different methods to measure the nonlinear coupling constant of the given crystal are also presented and compared[9].

The experimental arrangement is shown in Fig. 4.6. The output of the Argon ion laser at 514nm was expanded and spatial-filtered into an approximately 1-inch diameter beam. The total beam intensity $I_1+I_2+I_4$ was $0.3W/cm^2$. The crystal C was either a $4.5x4.5x5mm^3$ $BaTiO_3$ or a $5x5x6mm^3$ SBN crystal. Both crystals were electrically poled into a

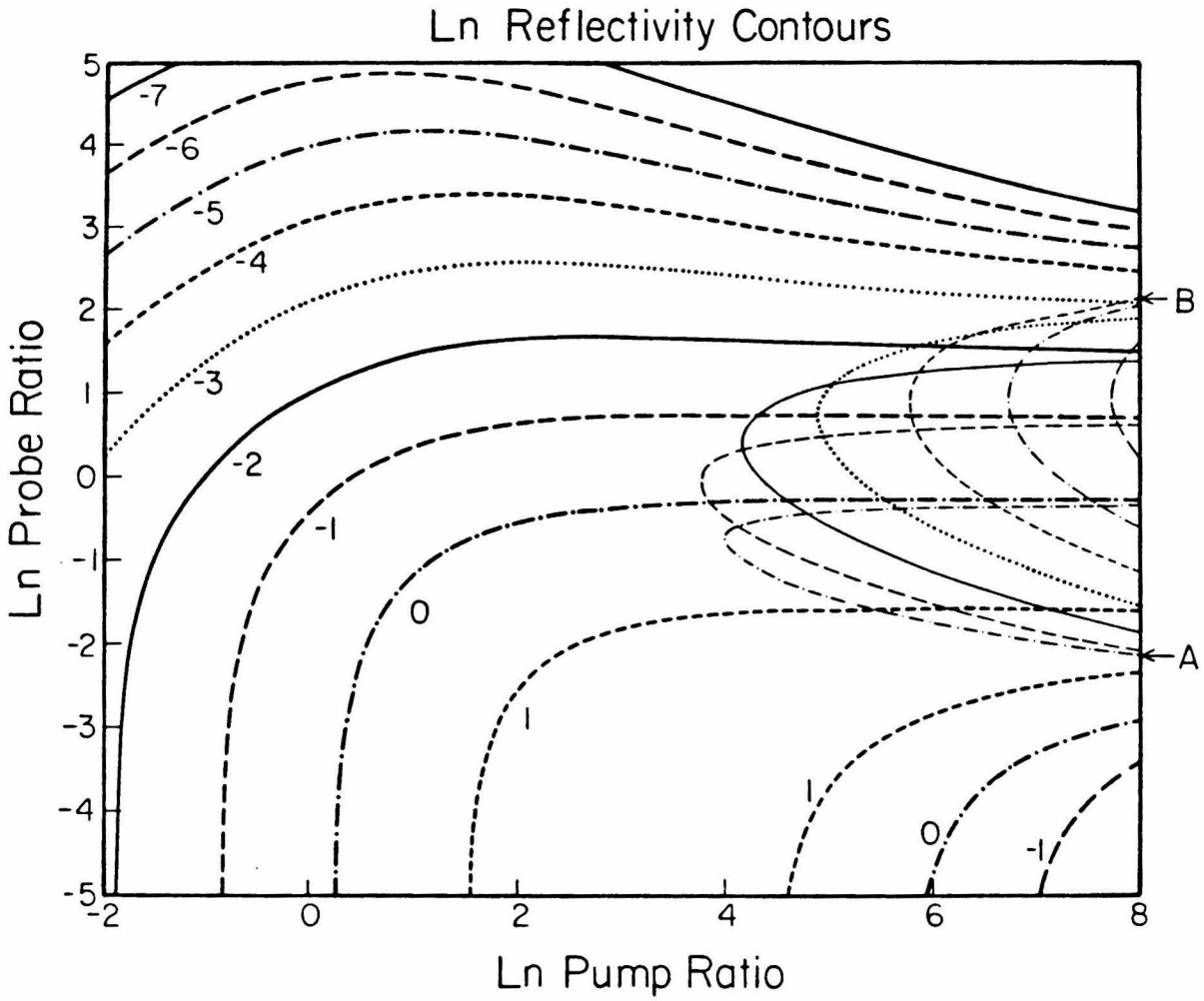

Fig. 4.5 : Contour plot of phase conjugate reflectivity for $\gamma\ell$=-3, as a function of both pump and probe ratios.(after Ref. 7)

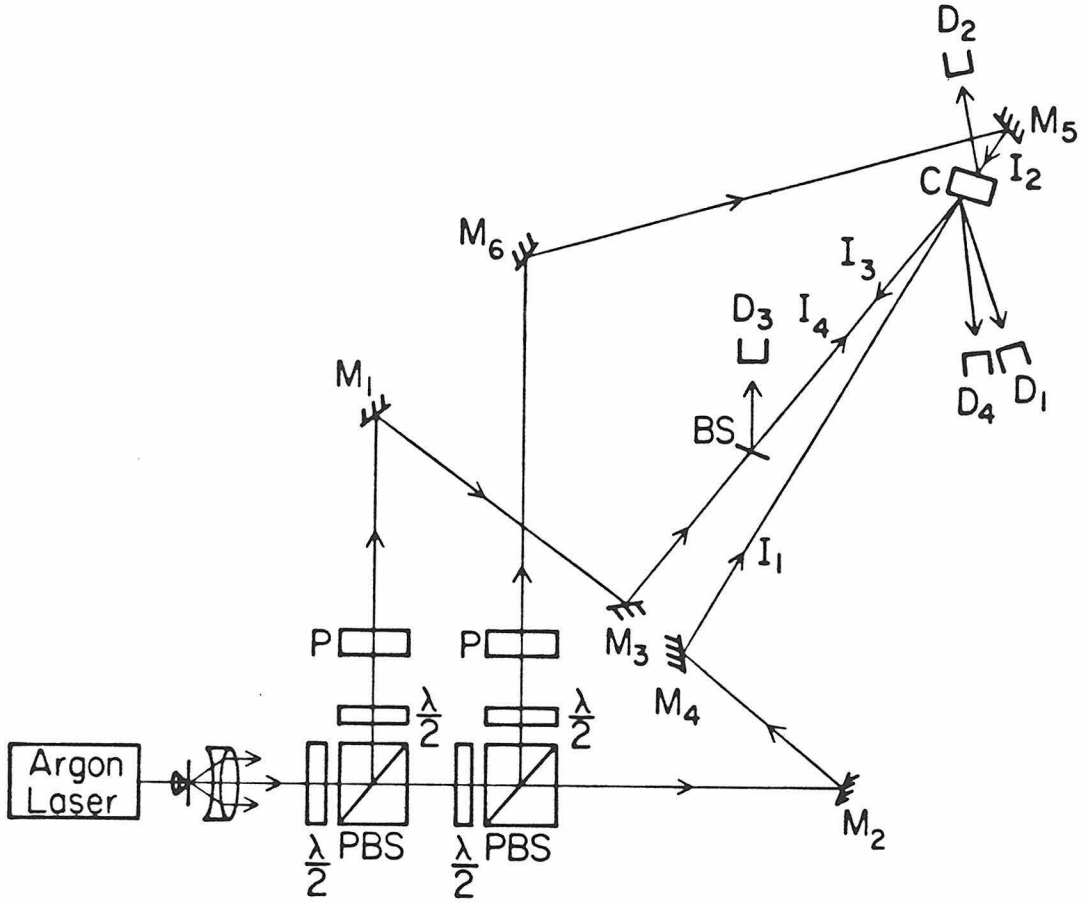

Fig. 4.6: Experimental configuration for measuring phase conjugate reflectivity versus various beam ratios. Using a cartesian coordinate system with the incident beam traveling along the abscissa and the coordinate in inches, the elements are 10x objective and pinhole (7,0); lens (12,0); half-wave plate, $\lambda/2$ and polarizing beamsplitters, PBS, (23,0) and (25,0); polarizers, P,(21,6) and (25,3); beamsplitter, BS, (30,8); crystal, C(42,25); mirrors M_1(17,21), M_2(40,0), M_3(29,7), M_4(30,4), M_5(44,28), and M_6(25,23); detectors D_1, D_2, D_3, D_4.

single domain before the experiment. Since only a small part (≈5mmx5mm) of the central portion of the expanded beam was used, we can approximate all the incoming beams to the crystal as plane waves. The half-wave plate and the polarizing beam splitter combination form a lossless beamsplitter with a transmission and reflection ratio that can be varied simply by rotating the half-wave plate. In order to make sure that only one grating (the transmission grating) dominated the system, the optical path lengths of beams 1 and 4 were adjusted to be the same, while the optical path difference between beams 2 and 4 was adjusted to be much longer than the coherence length of the light source (<7cm) so that beams 2 and 4 cannot interfere coherently to "write" a grating. The angle between beams 1 and 4 was made small (10^{o}) so as to increase the interaction length. The orientation of the crystals with respect to the input beams is shown in Fig. 4.7 where θ_1 and θ_2 are the angles of beams 1 and 4 with repect to the normal of the crystal C. All the beams were polarized in the plane of Fig. 4.6 to utilize the large r_{42} electrooptical coefficient of $BaTiO_3$. The phase conjugate beam I_3 was separated from beam 4 by a beam splitter BS and was detected by detector D_3. Parts of the intensities of beam 1, 2 and 4 were reflected at the surface of the crystal and were detected by detector D_1, D_2, and D_4 respectively. All the data collected by detectors D_1-D_4 were sent to a minicomputer for data analysis.

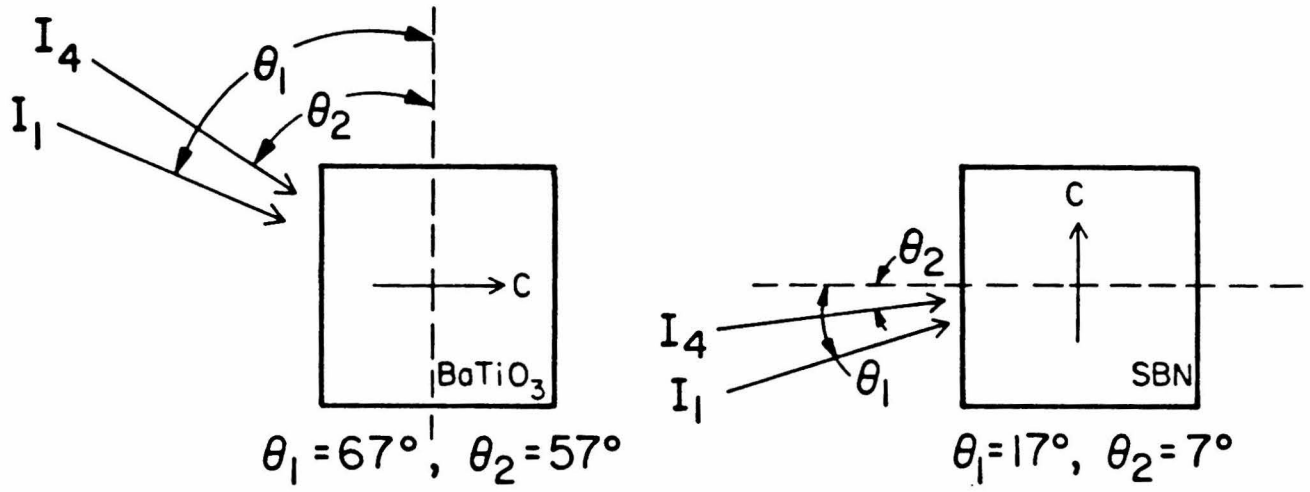

Fig. 4.7 : The orientation of $BaTiO_3$ crystal and the SBN crystal with respected to the input beams.

The experimental results for the $BaTiO_3$ crystal are shown in Fig. 4.8(a) and (b). The phase conjugate reflectivity, $R = I_3(0)/I_4(0)$, was plotted against the probe ratio, q, at various pump ratios, r. A set of theoretical curves based on Eq. [4.15] was also plotted. These theoretical curves give a best fit to the experimental curves if the nonlinear coupling constant $\gamma\ell$ is chosen to be -0.9.† Similar experiments were also done with SBN whose large electrooptic coefficient is r_{33}. The results are shown in Fig. 4.9. The coupling constant chosen from the best curve fitting is -1.3. This provides the first method of determining the nonlinear coupling constant.

The phase conjugate reflectivity versus the pump ratio at very small probe ratios (i.e. undepleted pumps approximation which is I_1, $I_2 \gg I_3$, I_4) are shown in Fig. 4.10 and 4.11. The experimental curve fits well with the theoretical curve except at very large and very small pump ratios. From the theory of undepleted pumps approximation, Section 4.3a, the phase conjugate reflectivity R for negligible absorption is, Eq. [4.13]

$$R = \left| \frac{\sinh\left(\frac{\gamma\ell}{2\cos\theta_2}\right)}{\cosh\left(\frac{\gamma\ell}{2\cos\theta_2} + \frac{\ln r}{2}\right)} \right|^2 \qquad [4.24]$$

---

† The geometrical factor, $\cos\theta$, of the coupling constant $\gamma\ell$ was neglected in plotting the theoretical curves in Figs. 3.8 - 3.11.

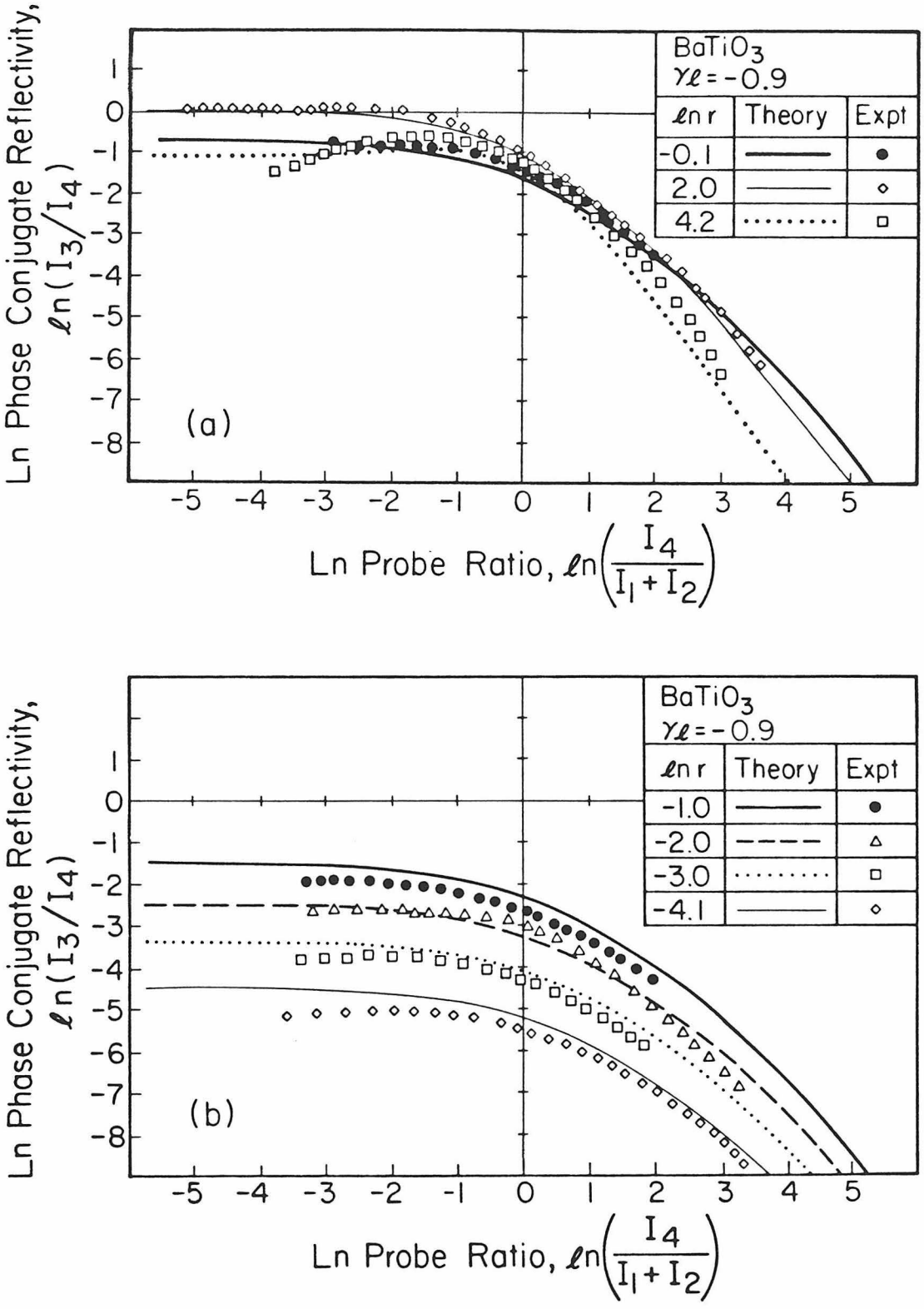

Fig. 4.8 : Experimental and theoretical curves of phase conjugate reflectivity in $BaTiO_3$ vs. probe ratio at ln pump ratio equals to (a) 4.2, 2.0, -0.1 and (b) -1.0, -2.0, -3.0, -4.1.

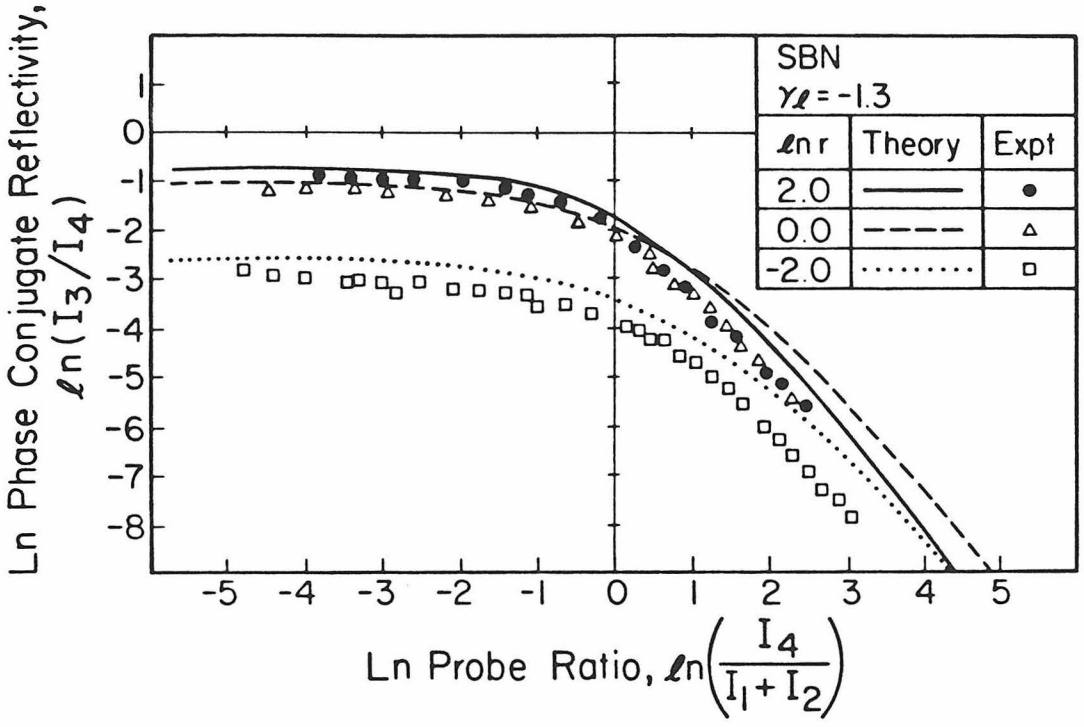

Fig. 4.9 : Experimental and theoretical curves of phase conjugate reflectivity in SBN vs. probe ratio at ln pump ratio equals to 2.0, 0.0, -2.0.

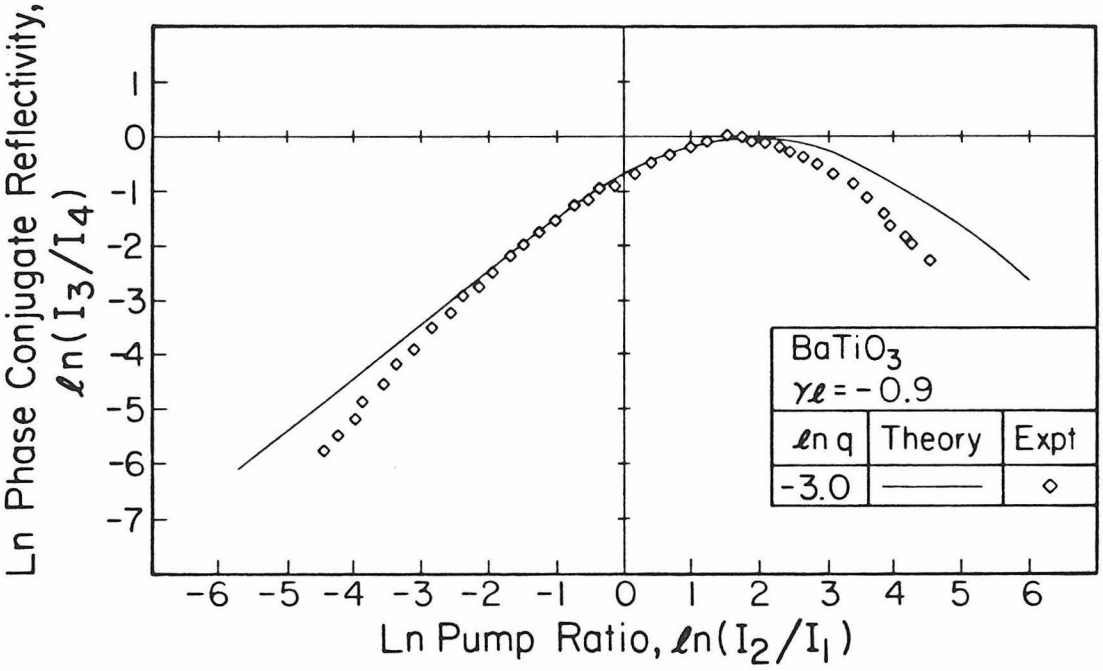

Fig. 4.10: Experimental and theoretical curve of phase conjugate reflectivity vs. the pump ratio in undepleted pumps region for $BaTiO_3$.

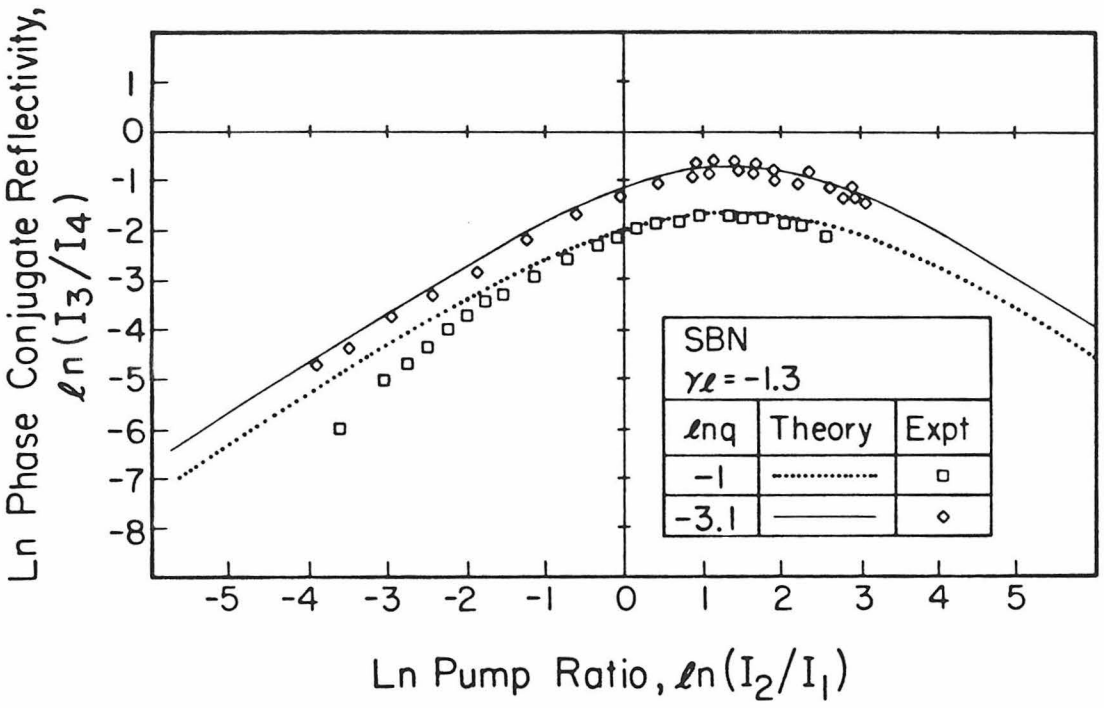

Fig. 4.11: Experimental and theoretical curve of phase conjugate reflectivity vs. the pump ratio in undeplete pumps region for SBN.

Therefore at the maxium reflectivity,

$$\gamma\ell = -\cos\theta_2 \ln r \qquad [4.25]$$

From the experimental data, the nonlinear coupling constant of $BaTiO_3$ ranges from -0.82 to -1.0 and from -1.1 to -1.5 for SBN. These values are consistent with the above values of the coupling constants which were determined by curve fitting.

Finally, a two-wave mixing experiment to measure the coupling constant directly was also performed. Here the energy exchange in a crystal of length ℓ between beams 1 and 2 was measured. The input and output intensities can be used to obtain the coupling constant γ according to: †

$$\gamma\ell = -\frac{1}{2}\left[\cos\theta_1 \ln\frac{I_1(\ell)}{I_1(0)} + \cos\theta_2 \ln\frac{I_4(0)}{I_4(\ell)}\right] \qquad [4.26]$$

The experimental arrangement was very similar to Fig. 4.6 with beam 2 being blocked and detector D_2 and D_3 repositioned to measure the transmitted beams $I_1(\ell)$ and $I_4(\ell)$ through the crystal. An experimental plot of coupling constant $\gamma\ell$ against beam ratio, $I_4(0)/I_1(0)$, is shown in Fig. 4.12. From the prediction of the photorefractive

---

† The crystal absorption, α, has already been taken into account in deriving this formula.

effect theory discussed in Chapters 1 and 2, the coupling constant should be independent of the beam ratio. The slight variation of the coupling constant with input beams ratio, which was also observed by Kuktarev et.al.[10], is under current investigation. The variation of coupling constant for $BaTiO_3$ is between -0.8 to -1.3 and -0.4 to -1.0 for SBN over the range of beam ratio from 0.02 to 20. These values are quite consistent with the values obtained by the two previous methods.

In deriving the coupled wave theory, Eqs. [4.13] and [4.15], the absorption of the crystal was neglected. Besides absorption, the crystals also give rise to asymmetric scattering (fanning)[11-13]. We approximate the total loss of the system by $\alpha\ell$, where

$$\alpha\ell \approx \frac{1}{2}\beta \ln\left[\frac{I_1(0) + I_4(0)}{I_1(\ell) + I_4(\ell)}\right] \qquad [4.27]$$

and β is a geometrical factor, in particular $\beta=\cos[(\theta_1+\theta_2)/2]$ in our experiments. The results are shown in Fig. 4.13. The average absorption, $\alpha\ell$, of the $BaTiO_3$ crystal is about 1.35 and is about 0.1 for the SBN crystal. Indeed the SBN crystal shows much less asymmetric scattering than the $BaTiO_3$ crystal. The effects of crystal absorption tend to lower the phase conjugate reflectivity, see Fig. 4.4(a). The theory also neglects multiple Fresnel reflections within the crystal. Therefore a certain amount of discrepancy between the theory and experiment is expected.

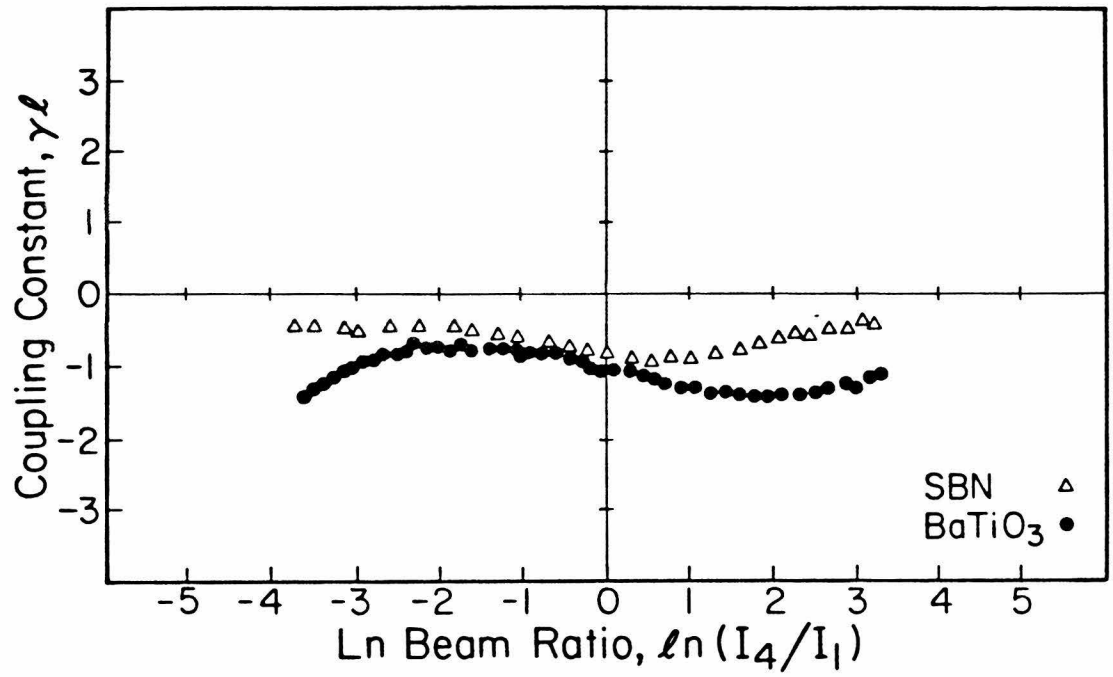

Fig. 4.12: The two beam coupling constant vs. the ratio of the intensities of the two input beams.

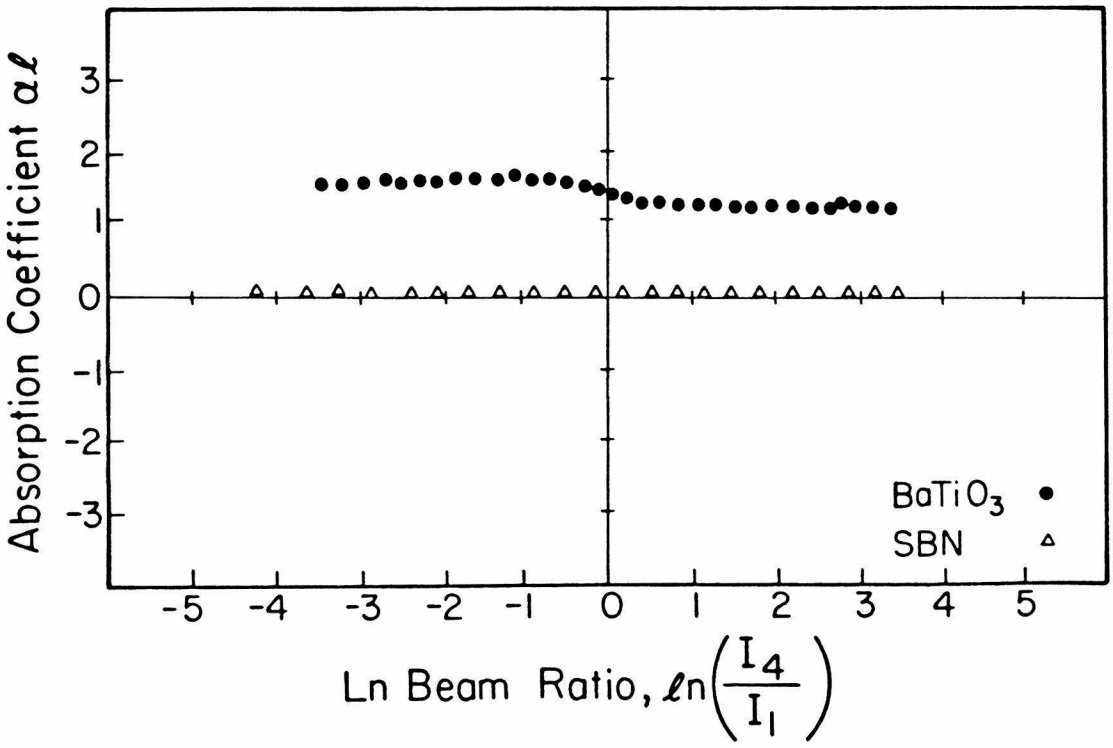

Fig. 4.13 : The total loss of the system, $\alpha\ell$, vs. the ratio of the intensity of the two input beams.

(4.5) The phase of phase conjugation

In Sections 4.3 and 4.4, the magnitude of the phase conjugate reflectivity was obtained theoretically and studied experimentally. In this section, the output phase of the phase conjugate wave as a function of various parameters will be studied[14]. These studies provide a better understanding of 4WM in photorefractive media and are needed in the analysis double phase conjugate resonators[14-17] in Section 5.3.

For simplicity, we assume that the nonlinear medium is lossless with only the transmission grating dominant, Eq. [4.14], and that the four interacting beams are plane waves. We represent A_j in Eq. [4.4] by

$$A_j(\mathbf{r}) = |A_j(\mathbf{r})| e^{i\psi_j(\mathbf{r})} \qquad j = 1,..,4 \qquad [4.28]$$

where $\psi_j(\mathbf{r})$ is the phase factor associated with the complex amplitude $A_j(\mathbf{r})$.

In the undepleted pumps approximation, from Eq. [4.13],

$$\psi_3(0) = \psi_1(0) + \psi_2(\ell) - \psi_4(0) + \mathrm{Im}\ \ln\left[\frac{e^{-\gamma\ell}-1}{r^{-1}e^{-\gamma\ell}+1}\right] \qquad [4.29]$$

In particular, $\psi_3(0) = \psi_1(0) + \psi_2(\ell) - \psi_4(0)$ if γ is real, which corresponds to a $\pi/2$ phase shift between refractive index grating and

the light interference fringes, see Eq. [3.8]. This happens in photorefractive crystals when the index grating is formed by charge diffusion. In general, $\psi_3(0)$ is a function of the complex coupling constant and pump ratio.

Without the undepleted pumps approximation, $\psi_3(0)$ can be determined from the following equation:

$$\psi_3(0) = \text{Im ln} \left[\frac{A_1^*(0)}{A_2(0)} \frac{A_3(0)}{A_4^*(0)} \right] + \psi_1(0) + \psi_2(0) - \psi_4(0) \qquad [4.30]$$

The given boundary conditions are $A_1(0)$, $A_2(\ell)$, $A_3(\ell) = 0$, $A_4(0)$. Therefore $\psi_1(0)$, $\psi_2(\ell)$ and $\psi_4(0)$ are known. $[A_1^*(0)/A_2(0)]$ and $[A_3(0)/A_4^*(0)]$ are[7],

$$\frac{A_1(s)}{A_2^*(s)} = - \frac{S_- D e^{\mu s} - S_+ D^{-1} e^{\mu s}}{2c^* (D e^{-\mu s} - D^{-1} e^{\mu s})} \qquad [4.31a]$$

$$\frac{A_3(s)}{A_4^*(s)} = - \frac{S_- E e^{\mu s} - S_+ E^{-1} e^{\mu s}}{2c^* (E e^{-\mu s} - E^{-1} e^{\mu s})} \qquad [4.31b]$$

where $S_\pm$, D, E, μ and c are given from Eq. [4.17]-[4.21].

$\psi_2(0)$ in Eq. [4.30] can be calculated as follows:

rewrite Eq. [4.14b] into

$$\frac{d(\ln A_2^*)}{ds} = \frac{-\gamma}{I_+} \left(\frac{A_1}{A_2^*} \frac{A_3^*}{A_4} I_4 + I_3 \right) \qquad [4.32]$$

then integrate to get

$$\psi_2(0) = \psi_2(\ell) + \int_{\ell}^{0} \left\{ \mathrm{Re}\left[\frac{\gamma}{I_o}\right] \mathrm{Im}\left[\frac{A_1(s)}{A_2^*(s)} \frac{A_3^*(s)}{A_4(s)} I_4(s) \right] \right.$$

$$\left. + \left\{ I_3(s) + \mathrm{Re}\left[\frac{A_1(s)}{A_2^*(s)} \frac{A_3^*(s)}{A_4(s)} I_4(s) \right] \right\} \mathrm{Im}\left[\frac{\gamma}{I_o}\right] \right\} ds \qquad [4.33]$$

Where Re and Im are the real and imaginary parts, respectively. The integrand in Eq. [4.33] is known from Eq. [4.31], therefore, $\psi_3(0)$ is completely known. Again from Eq. [4.31], if γ is real,

$$\mathrm{Im}\left[\frac{A_1(s)}{A_2^*(s)} \frac{A_3^*(s)}{A_4(s)} \right] = 0$$

Therefore,

$$\psi_3(0) = \psi_1(0) + \psi_2(\ell) - \psi_4(0) \quad , \qquad [4.34]$$

as in the case of the undepleted pumps approximation with real γ, and the phase of the conjugate reflection is independent of the intensities of the interacting beams. The integral in Eq. (4.33) can be evaluated numerically. Fig. 4.14 shows some numerical curves of $\psi_3(0)$ against natural log of the probe ratio, ln q, for various pump beam ratios r and phases of the complex coupling constant γ. $|\gamma\ell|$ is chosen to be 6 for all curves. Some of the curves show multiple values in $\psi_3(0)$ which are associated with the multiple values in phase conjugate intensity reflectivity, R, in Fig. 4.5. The basic physical difference between the two solution surfaces of Fig. 4.5 lies in the

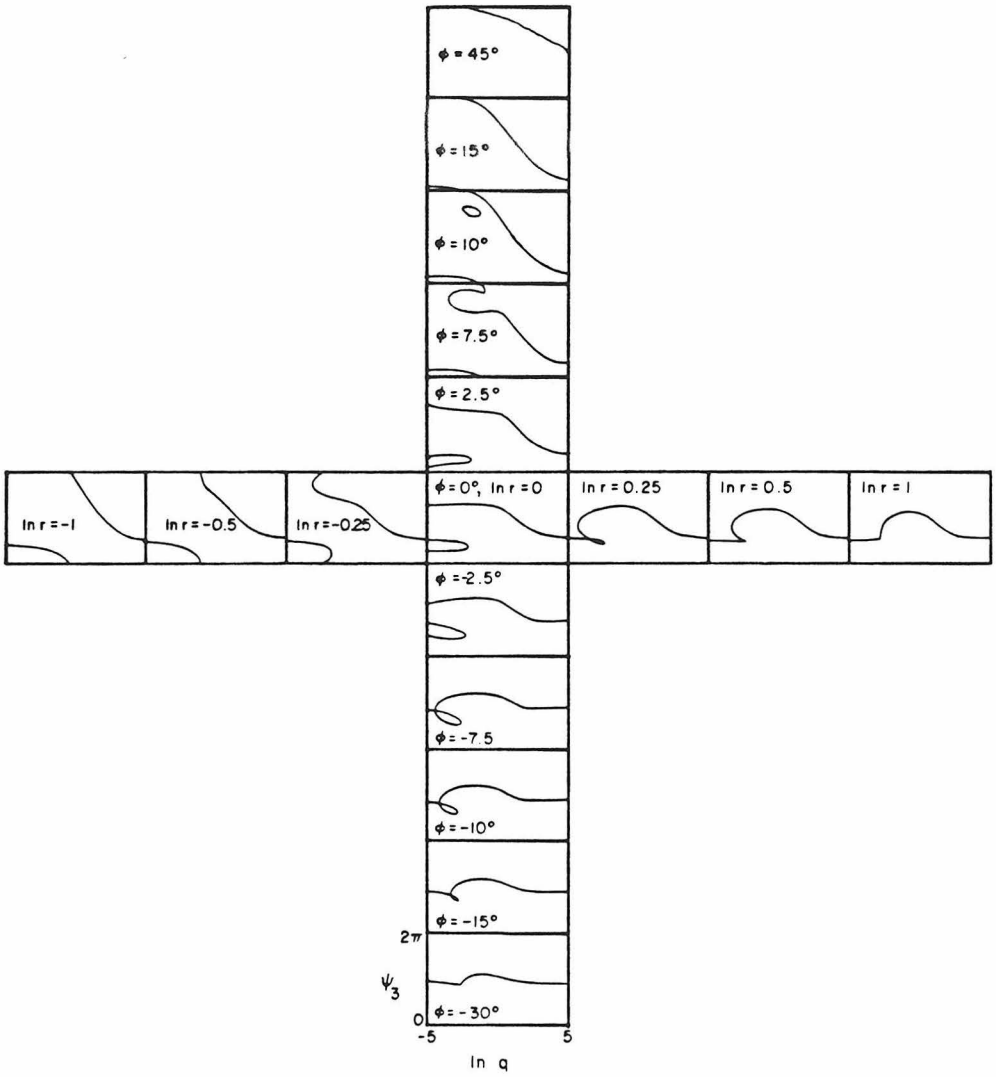

Fig. 4.14 :Numerical curves of ψ_3 vs. ln q for various ln r and ϕ. $|\gamma\ell|$ was chosen to be 6. For each of the curves, the range of ψ_3 is from 0 to 2π and from -5 to 5 for ln q.

relative phases, see Fig. 4.15, of the two terms $A_1A_4^*$ and $A_2^*A_3$ in the interference factor $(A_1A_4^* + A_2^*A_3)$ which appear in the coupled wave equations Eq. [4.14]. When the phase conjugate mirror is operating on the main surface, the one which extends over the entire q-r plane, the phase conjugate beam is generated so that the interference pattern formed between itself and beam 2 is <u>in phase</u> with the interference pattern formed between the forward going beams 1 and 4. On the secondary surface, these two terms are <u>π out of phase</u> with each other, so that both the grating strength and the reflectivity are diminished.

We also observe in Fig. 4.14 that the vertical series of curves are very similar to the horizontal series of curves. In other words, the effect of changing the pump ratio on the system is very similar to that of changing the phase shift between the light interference pattern and the refractive index pattern. This is reasonable because the phase shift between the light interference pattern and index grating causes energy coupling from one beam to the other beam. As a result, the pump ratio of the system changes accordingly. This kind of similarity relationship is very difficult to observe from the set of coupled wave equations, Eq. [4.14], but is clearly shown in Fig. 4.14.

The application of the above phase analysis of phase conjugation to the double phase conjugate resonator will be discussed in Section 5.3.

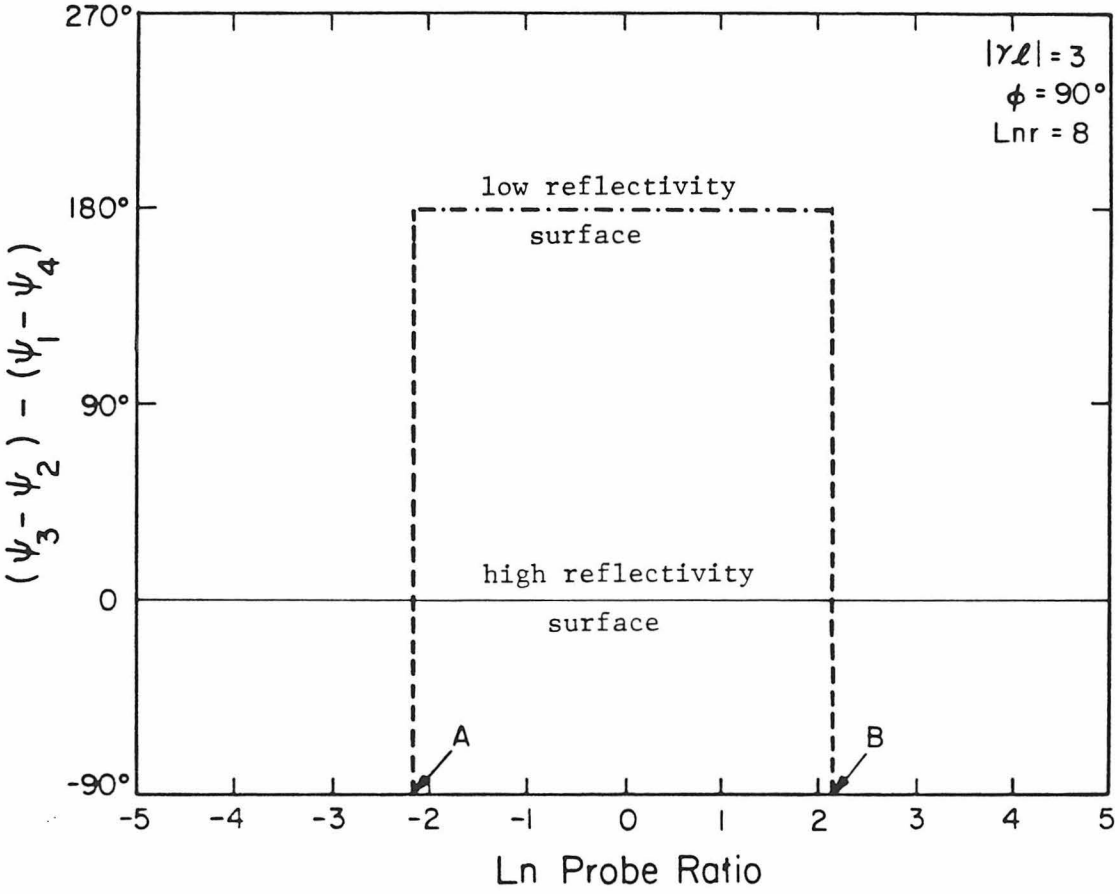

Fig. 4.15 : The relative phase of two grating terms, $A_1A_4^*$ and $A_2^*A_3$.

(4.6) Self-pumped phase conjugate mirror

The generation of phase conjugated wave using the four-wave mixing techniques discussed so far requires two external supplied counter-propagating pumping beams. One of the recent advances in this field is the demonstration of self-pumped phase conjugate mirrors (PPCM's) in photorefractive crystals. Several self-pumped configurations have been discovered; they are: (1) the linear PPCM[19]; (2) semilinear PPCM[19-20]; (3) 'internal reflection' PPCM[21]; (4) the ring PPCM[22]; and (5) the two-wave mixing PPCM[23]. Their respective configurations are shown in Fig. 4.16. The principle of operation behind most of the PPCM's, except the two-wave mixing PPCM, is that the input beam which is to be phase conjugated is used to pump, by the two-beam photorefractive coupling discussed in Chapter 3, an oscillation in a resonator. The resonator can be formed by two conventional mirrors as in the linear-PPCM, or a conventional mirror and a photorefractive crystal as in the semilinear PPCM, or 'two' photorefractive crystals as in the 'internal reflection' PPCM and the ring PPCM. The counter-propagating oscillation beams thus generated then act as the pumping beams to generate phase conjugation by four-wave mixing. A more detailed discussion on the photorefractive pumped oscillation is given in Chapter 5. On the other hand, the two-wave mixing PPCM is operated by the stimulated backscattering arising from the two-beam coupling in a photorefractive crystal. A discussion on the similarity between the photorefractive two beam coupling and Stimulated Brillouin Scattering

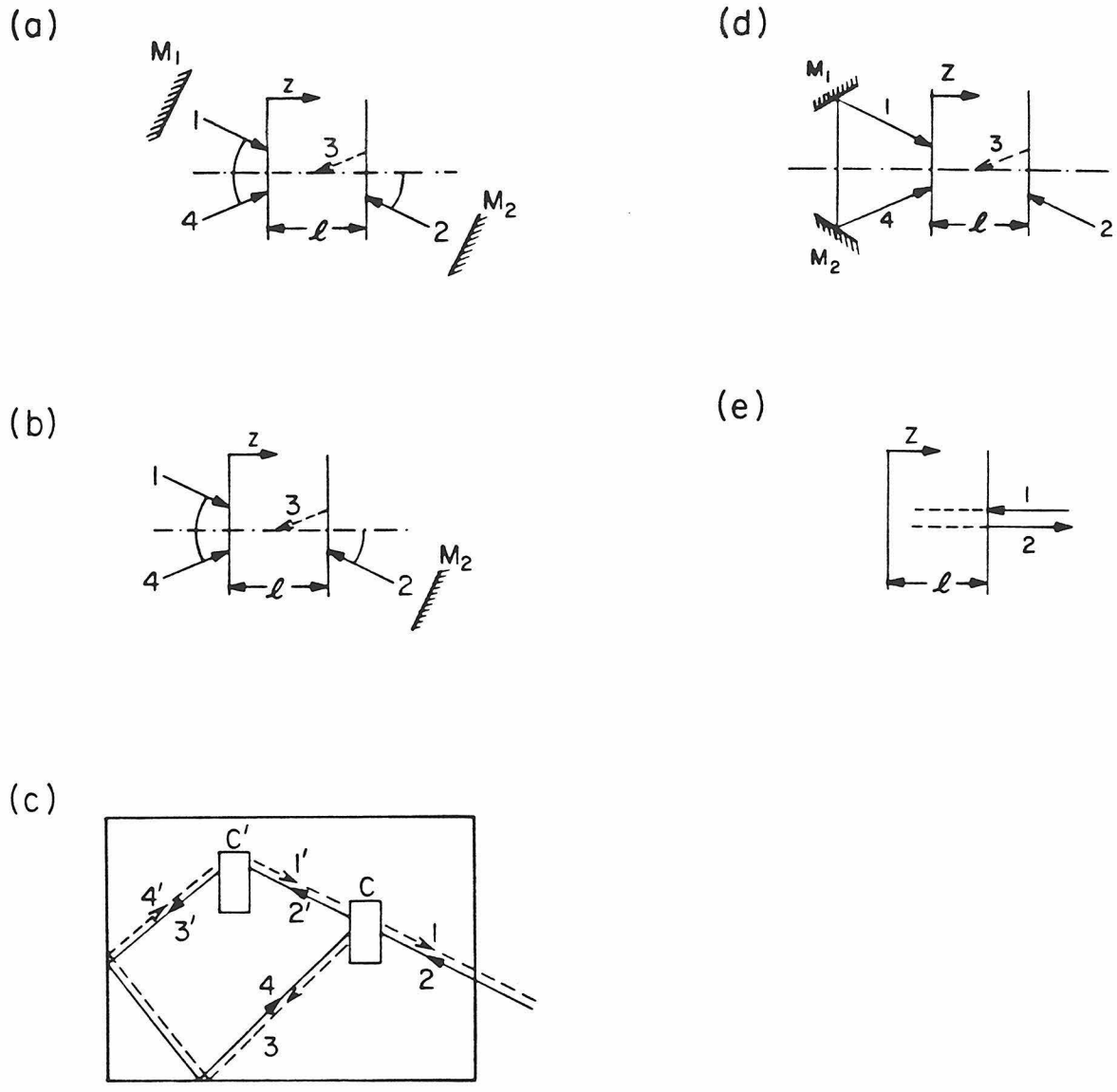

Fig. 4.16 : Geometry of passive phase conjugate mirrors. The probe is beam 4 and its phase conjugate is beam 3. The two pumping beams are land 2. (a) Linear PPCM; (b) Semi-linear PPCM; (c) Two-interaction-region PPCM; (d) Ring PPCM; and (e) 2WM-PPCM.

(SBS) is given in Section 5.4b.

At least some of the PPCMs discussed above are also capable of phase conjugating several laser lines simultaneously[20]; this development leads to the possibility of self-pumped conjugation of full color images. Using the all-lines output from an argon ion laser, simultaneous reflection of up to six different lines: 457, 476, 488, 496, 501, and 514 nm in both the semi-linear and the ring PPCMs were observed. The devices generate their own pumping beams so that no a priori knowledge of the spectral components of the incident laser beam is required, thereby removing one of the problems associated with previous multiline photorefractive phase conjugation where the pumps had to be supplied externally[24].

In Chapter 6, optical bistabilities using the semilinear PPCM and the ring-PPCM are demonstrated. These bistable devices are also found useful as thresholding devices for the associative memories experiments which are described in Section 7.2.

References for Chapter Four

1. Nils Abramson, The making and evaluation of holograms, New York, Academic Press, 1981.

2. A. Yariv, IEEE J.Q.E. QE-14, 650 (1978); ibid, QE-15, 256 and 523 (1979).

3. B. Fischer, M. Cronin-Golomb, J.O. White, and A. Yariv. Opt. Lett., **6**, pp. 519, 1981.

4. M. Cronin-Golomb, Ph.D. Thesis, California Institute of Technology, 1984, unpublished.

5. J.O. White, Ph.D. Thesis, California Institute of Technology, 1984, unpublished.

6. C. Karaguleff, T. Jannson, and H. Stoll, O-E LASE'86 Conference, postdeadline paper 613-06.

7. M. Cronin-Golomb, B. Fischer, J. O. White, and A. Yariv, IEEE J.Q.E. QE-20, 12 (1984).

8. M. Cronin-Golomb, J. O. White, B. Fischer, and A. Yariv, Opt. Lett. 7, 313 (1982).

9. S.-K. Kwong, Y.H. Chung, M. Cronin-Golomb, and A. Yariv, Opt. Lett. **10**, 359, 1985.

10. N.V. Kukhtarev, V.B. Markov, S.G. Odulov, M.S. Soskin, and V.L. Vinetskii, Ferroelectrics, **22**, pp. 949-964, 1979.

11. V.V. Voronov, I.R. Dorosh, Yu. S. Kuz'minov, and N.V. Tkachenko, Sov. J. Quantum Electron **10**(11), 1346, 1980.

12. J. Feinberg, J. Opt. Soc. Am., **72**, 46, 1982.

13. S. Odoulov, K. Belabaev, and I. Kiseleva, Opt. Lett., 10, 31, 1985.

14. S.-K. Kwong, M. Cronin-Golomb, B. Fischer, and A. Yariv, J. Opt. Soc. Am. A3, 157, 1986.

15. P. Yeh, I. McMichael, and M. Khoshnevisan, Opt. Soc. Am. Annual Meeting 1985, paper THK1.

16. M. Cronin-Golomb, B. Fischer, S.-K. Kwong, J.O. White, and A. Yariv, Opt. Lett. 10, 353, 1985.

17. P. Yeh, M. Khoshnevisan, M.D. Ewbank, and J.M. Tracy, Technical Program, Opt. Soc. Am. 1984 Annual Meeting, paper TuA1.

18. P. Yeh, Opt. Comm. 51, 195, 1984.

19. M. Cronin-Golomb, B. Fischer, J.O. White, and A. Yariv Appl. Phys. Lett., 41, pp. 689, 1982.

20. M. Cronin-Golomb, S.K. Kwong, and A. Yariv Appl. Phys. Lett., 44, pp. 727, 1984.

21. J. Feinberg, Opt. Lett. 8, pp. 569, 1983.

22. M. Cronin-Golomb, B. Fischer, J.O. White, and A. Yariv, Appl. Phys. Lett., 42, 919.

23. T.Y. Chang, and R.W. Hellwarth, Opt. Lett., 10, 408, 1985.

24. T.Y. Chang, D.L. Naylor, and R.W. Hellwarth, Appl. Phys. B28, 156, 1983.

Chapter 5: Oscillations with photorefractive gain

The two-beam coupling effect discussed in Chapter 4 has led us to use photorefractively pumped crystals as the gain element in a new class of optical resonator[1]. Photoerfractively pumped oscillations have indeed been observed experimentally[1-7]. Theories of oscillation with photorefractive gain has been developed[8-11].

In this chapter, two types of oscillators utilizing the photorefractive gain are discussed. They are: (1) the unidirectional ring oscillator; and (2) the double phase conjugate resonator. In Section 5.1, the two-beam coupling theory developed in Chapter 3 is applied to derive the oscillation conditions for the ring oscillator. The resulting predictions are then verified experimentally. In Section 5.2, the theoretical treatment is extended beyond the plane wave case to an interference pattern which produces a complicated hologram rather than a simple grating. In Section 5.3, the theory and experiment of a double phase conjugate resonator are discussed. In Section 5.4, two applications of the above analysis are described: (a) the optical path length to frequency conversion interferometer; and (b) the one-way, real time wave front converter.

(5.1) Ring Oscillator – Plane wave analysis

The simplest oscillator ultilizing photorefractive gain is the ring oscillator[1-5,8-9], shown in Fig. 5.1. The pumping beam, I_1, amplifies the beam I_2 circulating in the clockwise direction. Therefore this is a 'unidirectional' ring oscillator. Since only two-beam coupling is involved, we can apply the theory developed in Chapter 3.

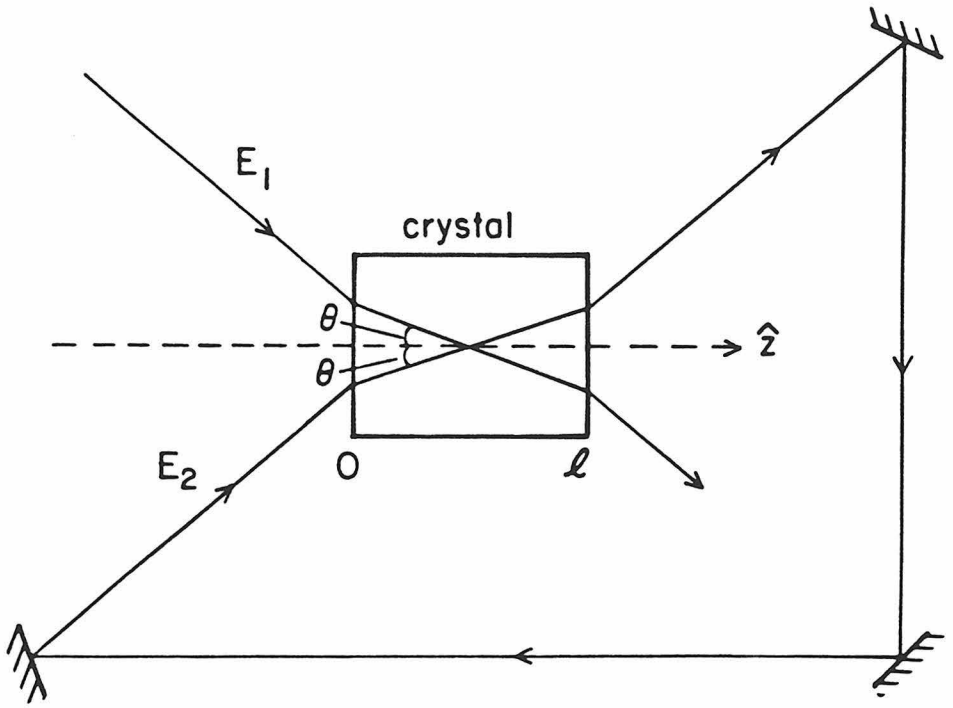

Fig. 5.1: A schematic diagram of photorefractively pumped unidirectional ring oscillator.

The boundary condition appropriate to a ring oscillator is,

$$I_2(0) = R\, I_2(\ell) \qquad [5.1]$$

where ℓ is the interaction length and R is the combined reflectivity for one round trip. From Eqs. [2.14] and [5.1], $I_2(0)$ and $[\psi_2(\ell) - \psi_2(0)]$ can be solved

$$I_2(0) = I_1(0) \left[\frac{1 - e^{-\Gamma\ell}}{1 - R\, e^{-\alpha\ell}} - 1 \right] \qquad [5.2]$$

$$\psi_2(\ell) - \psi_2(0) = - \frac{\Gamma'}{\Gamma} (\alpha\ell - \ln R) \qquad [5.3]$$

Eq. [5.2] gives the intensity of oscillation and Eq. [5.3] gives the phase shift of A_2 due to the nonlinear interaction. The oscillation conditions are that the round trip beam amplitude returns to its original value and the round phase delay is some multiple of 2π. From Eq. [5.2], the round trip amplitude condition is

$$\Gamma\ell > (\Gamma\ell)_{th} = \alpha\ell \ln R \qquad [5.4]$$

Using Eq. [3.9] and [3.13], Eq. [5.3] can be written as

$$\psi_2(\ell) - \psi_2(0) = \frac{1}{2} (\omega_2 - \omega_1)\, \tau\, (\alpha\ell - \ln R) \qquad [5.5]$$

where we recall that ω_1 and ω_2 are the frequencies of the pumping beam I_1 and the oscillation beam I_2, respectively.

The round trip phase condition for mode the **a** is

$$\frac{\omega_a L}{c} = \frac{\omega_2 L}{c} + \psi_2(\ell) - \psi_2(0) \qquad [5.6]$$

where ω_a is the a^{th} mode frequency of resonator with no photorefractive interaction and L is the length of the resonator. Substituting Eq. [5.5] into [5.6] to obtain

$$(\omega_2 - \omega_1) = \frac{2\,L}{c(\alpha\ell - \ln R)\tau} (\omega_a - \omega_2)$$

$$= \frac{\omega_a - \omega_1}{1 + \frac{\tau}{2\,t_a}} \qquad [5.7]$$

where t_a is the decay time constant of the photon density in the a^{th} mode. Since, typically, $t_a \ll \tau$, the oscillation frequency tends to be near ω_1

$$(\omega_2 - \omega_1) \simeq \frac{2\,t_a}{\tau} (\omega_a - \omega_1) \qquad [5.8]$$

For example, τ is of the order of 1 sec. for $BaTiO_3$ and experimentally $t_a(\omega_a - \omega_1)$ is roughly equal to one, so that $\omega_2 - \omega_1$ is of the order of a few Hz. Therefore the approximation in Eq. [3.7], $\omega_2 \simeq \omega_1$, is well justified. Eq. [5.8] determines the oscillation frequency.† If the zero detuning, $\omega_a - \omega_1 = 0$, is chosen as the origin, the frequency detuning $\delta = (\omega_2 - \omega_1)$ in Eq. [5.8] can be written as

$$\delta = \frac{2\,t_a}{\tau} \frac{\omega_1}{L} \Delta L \qquad \left(-\frac{\lambda}{4} \leq \Delta L \leq \frac{\lambda}{4}\right) \qquad [5.9]$$

where ΔL is the mirror displacement from the origin. Recalling that τ, from Eq. [3.11], is inversely proportional to the sum of the pumping and oscillation beam intensities. From Eqs. [3.11], [5.2] and [5.8],

---

† The result is very similar to the "frequency pulling" effect in laser oscillators[12]: if the atomic resonance frequency ω_1 does not coincide with the passive resonance frequency of the resonator ω_a, the laser frequency ω_2 will be shifted away from ω_a toward ω_1.

$$(\omega_2 - \omega_a) \sim (\omega_1 - \omega_a)(\tau'/t_a)$$

where τ' is the life time of the atomic transition. Since, typically $t_a \gg \tau'$, the laser tends to oscillate near ω_a.

$$\tau(s,\Delta L) = \left[\frac{E_D+E_\mu}{E_D+E_q}\right] \frac{N_A}{\alpha N} \left[I_1(0)\, e^{-\alpha s} \frac{1-\exp\left(- \dfrac{2\,\gamma_o \ell}{1+4\, t_a^2\, \omega_1^2 (\Delta L)^2/L^2} \right)}{1 - R\, e^{-\alpha \ell}} \right]^{-1}$$

[5.10]

Combining Eqs. [5.9] and [5.10], the relationship between the frequency detuning δ and the mirror displacement ΔL can be obtained. Assuming no absorption, theoretical plots of frequency detuning and the oscillation intensity versus mirror displacement are shown in Fig. 5.2(a) and (b) respectively.

The theory presented above has been tested experimentally[3,4] using the apparatus shown in Fig. 5.3. The output from a single longitudinal mode argon ion laser (λ= 514.5nm, P=0.2W, beam diameter = 2mm) was directed to a poled $BaTiO_3$ crystal. The crystal C-axis was in the plane of the ring oscillator in order to make use of the large electrooptic coefficient r_{42}. Mirrors M_1, M_2 and M_3 were aligned to form a ring resonator (L=38cm). Mirror M_1 was set on a piezo-electric mount. A 0.6 mm diameter pinhole was inserted inside the oscillating cavity in order to force a stable single transverse mode oscillation (without the pinhole, the oscillation pattern varied erratically in time)[7]. A fraction of the oscillating beam reflected from the front surface of the crystal was combined with the pumping laser beam to form interference fringes. Detector D_1 monitored the speed of moving fringes, from which the frequency offset δ was inferred.

Fig. 5.4 shows the experimental result of frequency detuning δ against the displacement of mirror M_1, which agrees qualitatively with Fig. 5.2. The gain linewidth is, according to Eq. [3.9], τ^{-1} Hz which

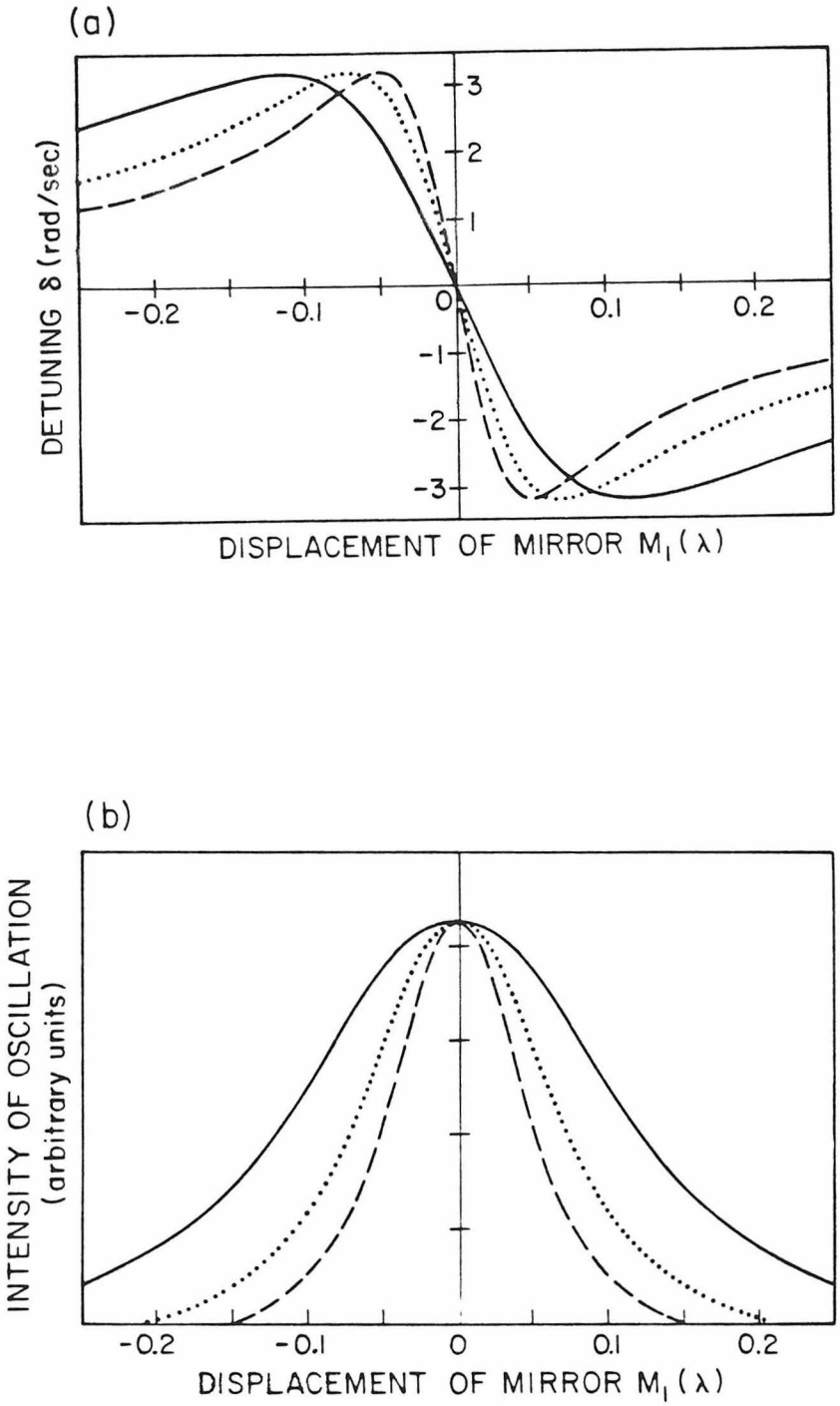

Fig. 5.2: Theoretical plot of (a) frequency detuning and (b) oscillation intensity versus mirror displacement in a ring resonator, where $\gamma_0 \ell = 1.5$, R=0.9 and $4\pi t_a c/L$=15(——), 25(• • •) and 35(---).

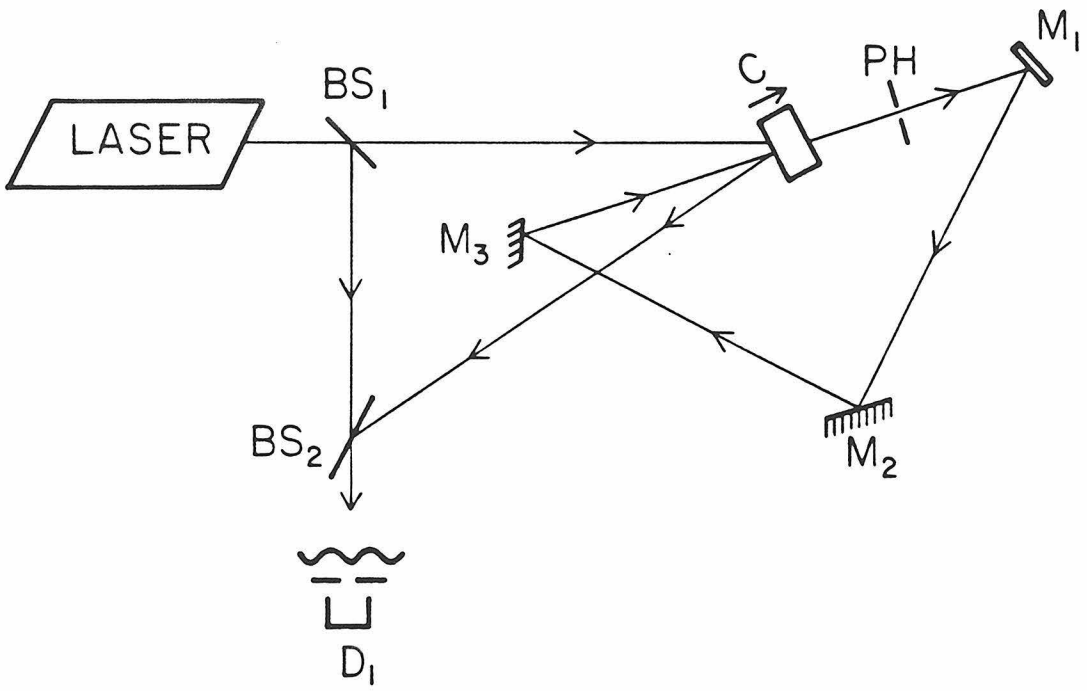

Fig. 5.3: Experimental configuration for measuring frequency detuning δ versus displacement of mirror M_1. Using a cartesian coordinate system with the laser beam traveling along the abscissa and the coordinate in inches, the elements are the Ar laser (0,0); beam splitters BS_1 (1,0), BS_2 (1,-3.5); mirrors M_1 (9,1), M_2 (7,-3) and M_3 (3,-1); crystal C (6,0); 0.6 mm diameter pinhole PH (7.5,0.5); detector D_1 (1,-4.5).

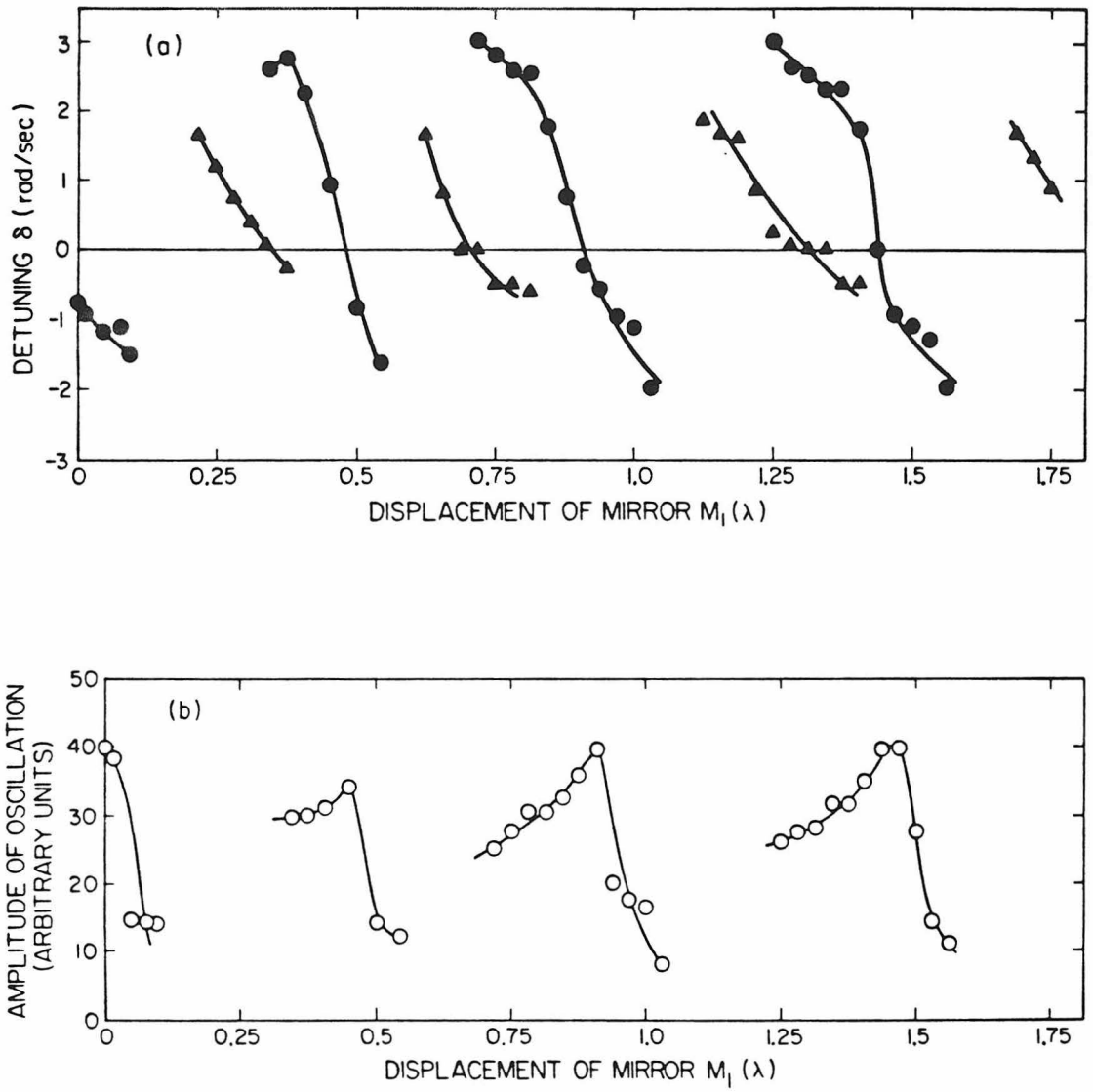

Fig. 5.4: (a) Experimental data of frequency detuning δ versus displacement of mirror M_1, TEM_{00} mode (•), TEM_{01} mode (Δ).
(b) The oscillating beam power of TEM_{00} mode versus displacement of mirror M_1.

in $BaTiO_3$ is a few Hz so that the maximum detuning δ observed is a few Hz. The oscillator can support two transverse modes, TEM_{00} and TEM_{01}. From Fig. 5.4a, the slopes of frequency detuning versus the mirror displacement curves gives, according to Eq. [5.9], an estimate of the ratio t_a/τ which is $1.89\text{x}10^{-8}$ and $0.88\text{x}10^{-8}$ for the TEM_{00} and the TEM_{01} modes respectively. This ratio, t_a/τ, is larger for the TEM_{00} mode than the TEM_{01} mode since the latter, suffering higher diffraction losses, has a smaller t_a. At each region of discontinuity in δ, for example at 0.18λ, 0.6λ, 1.1λ and 1.65λ, the oscillation was unstable and rapid mode hopping between the TEM_{00} and TEM_{01} modes was observed. At other points, transitions between TEM_{00} and TEM_{01} could be induced by disturbing the system, for example, by vibrating one of the ring cavity mirrors. The longitudinal mode spacing was $7.9\text{x}10^8$ Hz and the transverse mode spacing between TEM_{00} and TEM_{01} mode was $2.13\text{x}10^8$ Hz. The power of the oscillating beam for the TEM_{00} mode was also plotted in Fig. 5.4b. The oscillation power was near maximum at zero frequency detuning, $\delta=0$ which is due to the fact that at this point the coupling constant γ as given by Eq. [3.9] is maximum.

By using an additional pumping beam to pump the oscillation in the opposite direction, bi-directional oscillation in a ring resonator was experimentally observed by White et al.[2] and Rajbenbach et al.[5]. A theoretical analysis of photorefractive coupling of counterpropagating travelling waves in ring resonators has been reported by Yeh[10]. The inequality in transmissivities and phase shifts leads to a splitting in both oscillation frequency and intensity.

(4.2) Ring Oscillator – General Oscillator Theory

In this section we present an analysis similar to the Lamb's self-consistent analysis of an inhomogeneous laser[12,13]. Referring to Fig. 4.1, the known input (pump) beam is written as

$$\vec{E}_1(\vec{r},t) = \frac{1}{2}\vec{E}_{10}(\vec{r})e^{i\omega_1 t} + \text{c.c.} \qquad [5.11]$$

where $\vec{E}_{10}(\vec{r})$ contains the propagation factor as well as describing the effect of distortion and of information (spatial) modulation of the beam. The oscillation beam which establishes itself in the ring oscillator is taken as $\vec{E}_2(\vec{r},t)$ and our immediate task is to solve for the oscillation condition and the oscillation frequency of this beam. The resonator field can be expanded in the (complete) set of resonator modes $\vec{E}_a(\vec{r})$ [13]

$$\vec{E}_2(\vec{r},t) = \sum_a -\frac{1}{\sqrt{\epsilon}} p_a(t)\vec{E}_a(\vec{r}) \qquad [5.12a]$$

$$\vec{H}_2(\vec{r},t) = \sum_a \frac{1}{\sqrt{\mu}} \omega_a q_a(t)\vec{H}_a(\vec{r}) \qquad [5.12b]$$

where $\vec{E}_a(\vec{r})$ and $\vec{H}_a(\vec{r})$ satisfy the resonator boundary conditions for electric and magnetic fields, respectively. $\epsilon(\vec{r})$ and μ are electric and magnetic permittivities, respectively. In addition,

$$\vec{\nabla} \times \vec{E}_a = k_a \vec{H}_a \qquad [5.13a]$$

$$\vec{\nabla} \times \vec{H}_a = k_a \vec{E}_a \qquad [5.13b]$$

where

$$\omega_a = k_a(\mu\epsilon)^{-1/2} \qquad [5.13c]$$

ω_a and k_a are the radian oscillation frequency and wave number of the a-th mode, respectively. The quantities $p_a(t)$ and $q_a(t)$ contain the temporal information of mode a, including that of the frequency. In addition, the modal functions $\vec{E}_a$ and $\vec{H}_a$ are orthonormal according to

$$\int_{V_{res}} \vec{E}_a \cdot \vec{E}_b dV = \delta_{ab} \quad \text{and} \quad \int_{V_{res}} \vec{H}_a \cdot \vec{H}_b dV = \delta_{ab} \qquad [5.14]$$

The resonator contains a distributed polarization field $\vec{P}_{NL}(\vec{r},t)$ due to the nonlinear interaction so that Maxwell's equations can be written as

$$\vec{\nabla}x\vec{H} = \vec{j} + \frac{\partial}{\partial t}(\epsilon\vec{E} + \vec{P}_{nonresonant} + \vec{P}_{NL})$$

$$= \vec{\sigma}(\vec{r})\ \vec{E} + \epsilon(\vec{r})\ \frac{\partial E}{\partial t} + \frac{\partial}{\partial t}\ \vec{P}_{NL} \qquad [5.15a]$$

$$\vec{\nabla}x\vec{E} = -\mu\frac{\partial\vec{H}}{\partial t} \qquad [5.15b]$$

where $\sigma(\vec{r})$ is the effective conductivity that is introduced to account for the losses. Using Eqs. [5.12], [5.13] and [5.15], the resonator field will satisfy the equation

$$\sum_a \frac{1}{\sqrt{\mu}}\ \omega_a q_a k_a \vec{E}_a = -\sigma \sum_a \frac{1}{\sqrt{\epsilon}}\ p_a \vec{E}_a - \sum_a \sqrt{\epsilon}\ \dot{p}_a \vec{E}_a + \frac{\partial}{\partial t}\ \vec{P}_{NL}(\vec{r},t) \qquad [5.16]$$

Dot multiplying Eq. [5.16] by $\vec{E}_b$, integrating over the resonator volume V_{res} and using the orthonormality condition, Eq. [5.13], leads

to

$$\omega_b{}^2 q_b + \frac{\sigma}{\epsilon} p_b + \dot{p}_b - \frac{1}{\sqrt{\epsilon}} \frac{\partial}{\partial t} \int_V \vec{P}_{NL} \cdot \vec{E}_b \, dV = 0$$

$$\omega_b{}^2 \dot{q}_b + \frac{\sigma}{\epsilon} \dot{p}_b + \dot{p}_b^{\cdot} - \frac{1}{\sqrt{\epsilon}} \frac{\partial^2}{\partial t^2} \int_V \vec{P}_{NL} \cdot \vec{E}_b \, dV = 0 \qquad [5.17]$$

Substituting Eq. [5.12a] into Eq. [5.15b] and using Eq. [5.12b], then the equation

$$p_b = \dot{q}_b \qquad [5.18]$$

is obtained. Using Eq. [5.18], Eq. [5.17] becomes (without loss of generality, subscript a is used to represent the oscillating mode)

$$\dot{p}_a^{\cdot} + \frac{\omega_a}{Q_a} \dot{p}_a + \omega_a^2 p_a = \frac{1}{\sqrt{\epsilon}} \frac{\partial^2}{\partial t^2} \int_{V_{res}} \vec{P}_{NL}(\vec{r},t) \cdot \vec{E}_a(\vec{r}) dV \qquad [5.19]$$

where $Q_a = \omega_a \epsilon / \sigma$ is the quality factor of the resonator for mode a and $\vec{P}_{NL}(\vec{r},t)$ is the polarization in the photorefractive crystal due to the nonlinear interaction between the pump (input) beam $\vec{E}_1(\vec{r},t)$ and the oscillator field $\vec{E}_2(\vec{r},t)$. From [5.17] ω_a is identified as the resonance frequency of mode a in the no loss ($Q_a \to \infty$) limit. The distributed nonlinear polarization term $\vec{P}_{NL}(\vec{r},t)$ driving the oscillation of the resonator field is that produced by the incidence of the input field $\vec{E}_1(\vec{r},t)$ on the index grating created photorefractively by the interaction of the field $\vec{E}_1(\vec{r},t)$ and the ring oscillator field $\vec{E}_2(\vec{r},t)$. Assuming only one mode, say a, oscillates, then $\vec{E}_2(\vec{r},t)$ is replaced by the a^{th} summand in [5.12] and write

$$\vec{P}_{NL}(\vec{r},t) = \text{Re} \, [\epsilon_o \Delta n(\vec{r},t) \vec{E}_1(\vec{r},t)] \qquad [5.20]$$

where Δn, the index grating formed by the interference of the input beam $\vec{E}_{10}(\vec{r})e^{i\omega_1 t}$ and the oscillation field $\epsilon^{-1/2}p_a(t)\vec{E}_a(r)$ is given by Eq. [3.2]

$$\Delta n(r,t) = -\frac{2c\ i\gamma}{\omega_2\sqrt{\epsilon}} \frac{p_{ao}(t)\left[\vec{E}_{10}^{\,*}\cdot\vec{E}_a\right] e^{-i(\omega_2-\omega_1)t}}{|\vec{E}_{10}|^2 + \frac{1}{\epsilon}|p_a\vec{E}_a|^2} + c.c. \qquad [5.21]$$

where γ is given in Eq. [3.9], and then

$$\vec{P}_{NL}(\vec{r},t) = -\frac{2\epsilon_o c}{\omega_2\sqrt{\epsilon}}\, i\gamma \frac{p_{ao}(t)\left[\vec{E}_{10}^{\,*}\cdot\vec{E}_a\right]\vec{E}_{10}e^{i\omega_2 t}}{|\vec{E}_{10}|^2 + \frac{1}{\epsilon}|p_a\vec{E}_a|^2} + c.c. \qquad [5.22]$$

where $p_a(t)$ is written as the product of a slowly varying amplitude $p_{ao}(t)$ and an optical oscillation term $\exp(i\omega t)$

$$p_a(t) = p_{ao}(t)e^{i\omega_2 t} \qquad [5.23]$$

The sole time dependence of $\vec{P}_{NL}(\vec{r},t)$ is that of mode **a**, i.e, of the term $p_a(t)$. The time dependence of the input mode $\vec{E}_1(\vec{r},t)$ has disappeared since $\vec{E}_1$ appears in [5.22] multiplied by its complex conjugate. Another, equivalent way, to explain this fact is that the index grating produced by the interference of $\vec{E}_1$ and $\vec{E}_a$ (the cavity field) is moving since $\omega_2 \neq \omega_1$ and this velocity is just the right one to Doppler shift the incident frequency ω_1 to ω_2.

The oscillator equation, Eq. [5.19] becomes

$$\left[(\omega_a^2-\omega_2^2) + i\,\frac{\omega_a\omega_2}{Q_a} \right] p_{ao}(t) + (2i\omega_2+\frac{\omega_a}{Q_a})\,\dot{p}_{ao}+\dot{p}_{ao}^{\cdot}\,e^{i\omega_2 t}$$

$$= -\frac{2\epsilon_o c i\gamma}{\omega_2\epsilon}\,\frac{\partial^2}{\partial t^2}\int_{V_{crystal}} \frac{P_{ao}(t)|\vec{E}_{1o}^{\,*}\cdot\vec{E}_a|^2}{|\vec{E}_{1o}|^2+\frac{1}{\epsilon}|p_{ao}(t)\vec{E}_a(\vec{r})|^2}\,e^{i\omega_2 t}\,dV \qquad [5.24]$$

At steady state $\dot{p}_a$, $\dot{p}^{\cdot}_a$ vanish, $\partial/\partial t \to i\omega_2$ and $p_{ao}(t) = p_{ao}(\infty) =$ const. The oscillation condition [5.24] becomes

$$(\omega_a^2-\omega_2^2) + i\,\frac{\omega_a\omega_2}{Q_a} = \frac{2\epsilon_o\omega_2 c}{\epsilon}\,i\gamma f = i\,\frac{2\epsilon_o\omega_2 c}{\epsilon}\,f\,\frac{\gamma_o}{1+i(\omega_2-\omega_1)\tau} \qquad [5.25]$$

where in the second equality we used the zero external field ($E_o=0$) form of γ as given by Eq. [3.9] and f is given by

$$f = \int_{V_{crystal}} \frac{\left|\vec{E}_{1o}^{\,*}(\vec{r})\cdot\vec{E}_a(\vec{r})\right|^2}{|\vec{E}_{1o}(\vec{r})|^2+\frac{1}{\epsilon}|p_{ao}(\infty)\vec{E}_a(\vec{r})|^2}\,dV \qquad [5.26]$$

so that it is dimensionless and real.

The left side of [5.25] is a complex number which depends only on the passive resonator parameters and the (yet unknown) oscillation frequency ω_2. According to [5.22] the phase of the right side of [5.22] depends on $(\omega_2-\omega_1)$. The frequency ω_2 will thus adjust itself relative to ω_1 so as to satisfy [5.25]. Using [5.22] and separating the real and imaginary parts of [5.25] leads to

$$\omega_a^2 - \omega_2^2 = \frac{2c\,\epsilon_o f\gamma_o \omega_2(\omega_2-\omega_1)\tau}{\epsilon\left[1 + (\omega_2-\omega_1)^2\tau^2\right]} \qquad [5.27]$$

and

$$\frac{\omega_a\omega_2}{Q_a} = \frac{2c\,\epsilon_o f\gamma_o \omega_2}{\epsilon\left[1 + (\omega_2-\omega_1)^2\tau^2\right]} \qquad [5.28]$$

and since $\omega_1 \simeq \omega_a$, [5.27] and [5.28] can be accurately approximated by

$$\omega_a - \omega_2 = \frac{c\epsilon_o f\gamma_o\,(\omega_2-\omega_1)\tau}{2\epsilon\left[1 + (\omega_2-\omega_1)^2\tau^2\right]} \qquad [5.29]$$

In the limit $t_a \lll \tau$ where $t_a = Q_a/\omega_a$ is the decay time constant of the photon density in the a^{th} mode (with no photorefractive interaction) By using Eq. [5.28] and [5.29], ω can be solved

$$(\omega_2-\omega_1) \simeq 2\,\frac{t_a}{\tau}\,(\omega_a-\omega_1) \qquad [5.30]$$

which agrees exactly with the two beam coupling theory analysis, Eq. [5.8].

Let us return next to the threshold condition [5.28]. The parameter f is given by [5.26] and can be written as

$$f = \int \frac{\left|\vec{E}_{1o}^{\,*}(\vec{r})\cdot\vec{E}_a(\vec{r})\right|^2}{|\vec{E}_{1o}(\vec{r})|^2 + |\vec{E}_{osc}(\vec{r})|^2}\,dV \qquad [5.31]$$

$$\simeq \frac{1}{1 + \dfrac{\langle|\vec{E}_{osc}|^2\rangle}{\langle|\vec{E}_{1o}|^2\rangle}} \int_{V_c} \frac{\left|\vec{E}_{1o}^{\,*}(\vec{r})\cdot\vec{E}_a(\vec{r})\right|^2}{|\vec{E}_{1o}|^2}\,dV \qquad [5.32]$$

where the oscillating electric field of the a^{th} mode is written as, by using Eq. [5.12a]

$$\vec{E}_{osc}(\vec{r}) = -\frac{1}{\sqrt{\epsilon}} p_{ao}(\infty)\vec{E}_a(\vec{r})$$

and $< >$ to denote spatial averaging over the crystal volume. f is rewritten as

$$f = \frac{f_o}{1 + \dfrac{<|\vec{E}_{osc}|^2>}{<|\vec{E}_{10}|^2>}} \qquad [5.33]$$

where

$$f_o = \int \frac{\left|\vec{E}_{10}^{\,*}(\vec{r})\cdot\vec{E}_a(\vec{r})\right|^2}{|\vec{E}_{10}|^2}\, dV \qquad [5.34]$$

and [5.28] becomes

$$\frac{1}{t_a} = \frac{2\epsilon_o c\gamma_o f_o}{\epsilon\left[1 + 4(\omega_1-\omega_a)^2 t_a^2\right]}\left[\frac{1}{1 + \dfrac{<|\vec{E}_{osc}|^2>}{<|\vec{E}_{10}|^2>}}\right] \qquad [5.35]$$

The start oscillation condition is

$$\gamma_o \geq \frac{\epsilon\left[1 + 4(\omega_1-\omega_a)^2 t_a^2\right]}{2c\epsilon_o f_o t_a} \qquad [5.36]$$

and does not depend on the pumping intensity $|\vec{E}_{io}|^2$. The is a consequence of the index variation being driven by intensity modulation, not absolute intensity.

Equation [5.35] can be solved for the oscillating field intensity inside the resonator

$$\langle|\vec{E}_{osc}|^2\rangle = \langle|\vec{E}_{io}|^2\rangle\left[\frac{2\,\epsilon_o c\gamma_o f_o t_a}{\epsilon\left[1+4(\omega_1-\omega_a)^2 t_a^2\right]} - 1\right] \qquad [5.37]$$

which is reminiscent of the expression for the power output of homogeneously broadened lasers[15].

In the above analysis, the change in intensity of both the pump and resonator beams in the crystal due to the mutual power exchange is neglected. This neglect is well justified near threshold. Another important issue is the relationship of distortion (or intentional spatial modulation) of the pumping beam $\vec{E}_{io}$ on the oscillation. It follows from [5.34] that the main effect is to reduce the "projection" of $\vec{E}_{io}$ on $\vec{E}_a$ leading to a smaller f_o and thus, according to [5.36], to a higher threshold. The shape $\vec{E}_a(\vec{r})$ of the oscillating field is not affected. This is also the basic operational principle of the wave front converter to be discussed in Section (5.4).

This formalism can be generalised to include higher order modes of oscillation and be used to describe resonators with 4-wave mixing gain. In the latter case, the nonlinear polarization $\vec{P}_{NL}$ must include all the grating terms involved in the interaction.

(5.3) Double phase conjugate resonator

A photorefractive double phase conjugate resonator[6,11] is an optical cavity bounded by two phase conjugate mirrors. In the following, the experimental and theoretical results concerning the non-degenerate oscillation, which have been observed to be strongly dependent on the phases of the pumping beams, in a double phase conjugate resonator are discussed .

Consider the propagation of a probe beam traveling between two PCM's pumped at different frequencies. Suppose the first PCM (PCM_1) is pumping at frequency ω_1 and the second PCM (PCM_2) is pumping at ω_2. Without loss of generality, the probe is assumed travelling initially towards PCM_2, and to have frequency ω. Using the frequency-flipping character of PCM's, $(\omega_{pump} + \delta \rightarrow \omega_{pump} - \delta)$, the probe frequency has become $\omega + 2(\omega_1-\omega_2)$ after one round trip. After a sufficient number of round trips, the frequency of the probe would walk off the gain spectrum of both PCM's. In practice, this means that oscillation between two PCM's is not possible unless the mirrors are pumped by lasers whose frequency spectra overlap appreciably. If at least one of the PCM's is self pumped, this condition will be satisfied automatically.

With this in mind, the oscillation between a pair of PCM's pumped at the same frequency ω is analyzed, see Fig. 5.5. Allowing for possible non-degenerate oscillation we write the frequency of the field propagating from PCM_1 to PCM_2 as $\omega + \delta$, with $\omega - \delta$ the frequency of the field travelling in the opposite direction. The net accumulated round trip phase change is $\Phi_2(-\delta) - \Phi_1(\delta) + 2\delta L/c$, where $\Phi_i(\delta)$ is the phase change upon reflection from PCM_i and L is the cavity length. A self-consistent oscillation must satisfy

$$\Phi_2(-\delta) - \Phi_1(\delta) + 2\delta L/c = 2m\pi \qquad [5.38]$$

where m is an integer.

Each of the phase shifts Φ_i are due to two separate physical effects. The first is a dependence on the combined phases of the pumping beams. The amplitudes of the three input beams are essentially multiplied to give the amplitude of the phase conjugate reflection:

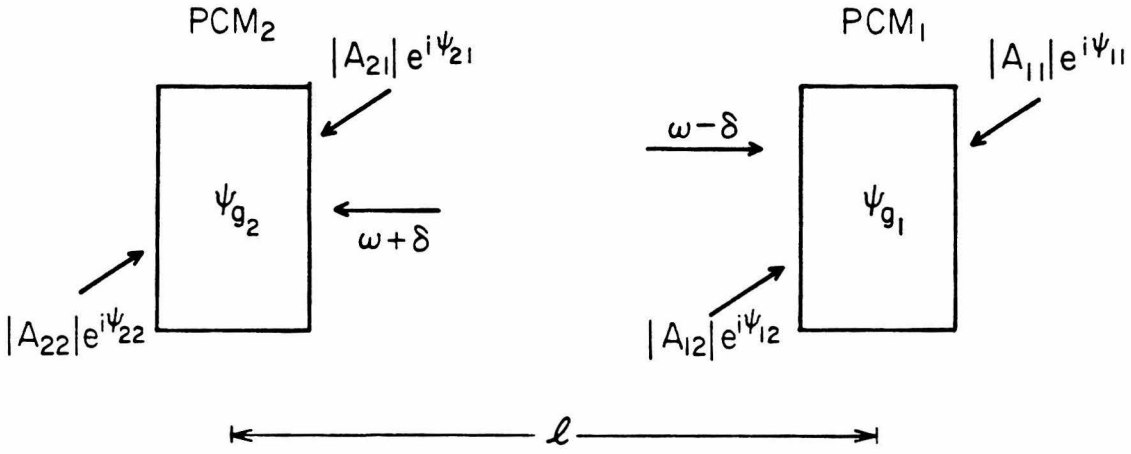

Fig. 5.5: Schematic diagram of a double phase conjugate resonator.

hence the pump phases, ψ_1 and ψ_2, are added to the reflected wave. The second effect involves the internal physics of the crystal. When the probe beam frequency is offset from that of the pump beams, the refractive index grating responsible for beam coupling moves in space in synchronism with the light interference pattern. The finite response time of the medium implies a phase lag, Θ, between the interference pattern and the index grating[16-17].

A general expression for Φ_i is given in Eq. [4.30]. In the undepleted pumps approximation, the phase shift Φ_i at mirror i is

$$\Phi_i(\delta) = \psi_{1i} + \psi_{2i} + \Theta_i(\delta) \qquad [5.39]$$

where Θ is given by Eq. [4.13]

$$\Theta = \text{Im ln} \left[\frac{\sinh\left(\frac{\gamma\ell}{2}\right)}{\cosh\left(\frac{\gamma\ell}{2} + \frac{\ln r}{2}\right)} \right] \qquad [5.40]$$

where r is the ratio of the intensities of the two pumping beams and γ is given by Eq. [3.9].

To see the underlying physics of the device more clearly, both PCM's are assumed to be the same except for the phases of the pumping beams so that $\Theta_1=\Theta_2=\Theta$. Since in the photorefractive case Θ is an odd function of δ, Eq. [5.38] can be rewritten as

$$-\Psi - 2\Theta(\delta) + 2\delta L/c = 2\pi m \qquad [5.41]$$

where $\Psi = \psi_{11} + \psi_{21} - \psi_{12} - \psi_{22}$. We see that, except for the special case $\Psi=0$, δ must be non-zero. It also follows from Eq. [5.41] that the δ is periodic in Ψ and L.

In the experiment, the response time of the photorefractive medium was much greater than the cavity round trip time, so that the term $2\delta L/c$ in Eq. [5.41] was negligible. Fig. 5.6 shows the theoretically

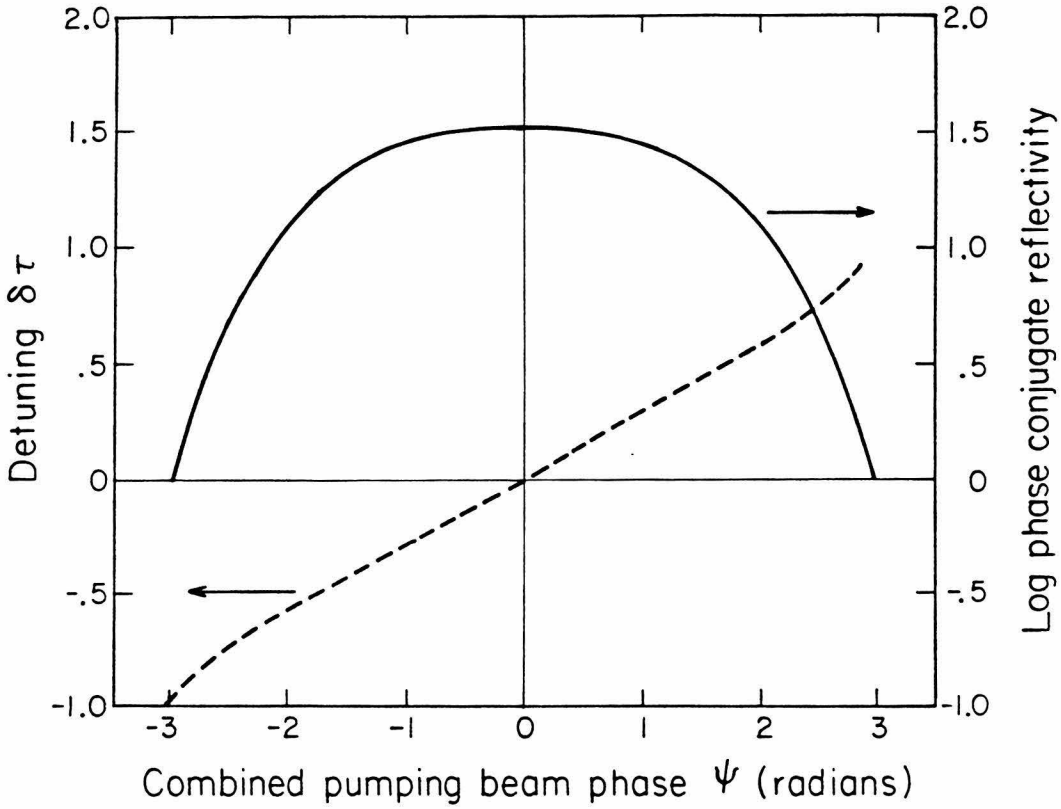

Fig. 5.6: Theoretical plot of frequency detuning in double conjugate conjugate resonator and associated reflectivity of the phase conjugate mirrors of which it is composed. The coupling constant $\gamma_o \ell$ for each mirror equals 3. The undepleted pumps approximation is used.

predicted frequency offset δ and the associated phase conjugate reflectivity as a function of Ψ with $\gamma_0 \ell = -3$. In the experiment, while it is the oscillation intensity and not the undepleted phase conjugate reflectivity that is measured in the experiment, these two quantities should be at least qualitatively similar.

Fig. 5.7 is a schematic of our experimental arrangement. The output of an argon ion laser running in single longitudinal mode at 514.5nm was divided at beamsplitter BS into two beams of equal intensity which pumped two crystals of $BaTiO_3$ as PCM's. The second set of two pumping beams, one for each PCM, was provided by retroreflecting mirrors M_1 and M_2. Mirror M_1 was on a piezomount, so that the combined pumping beam phase Ψ could be controlled by its position. The crystal orientations were chosen so that the reflectivity of each PCM to a beam arriving from the other was greater than unity. Oscillation beams built up in the double phase conjugate resonator, and the parts of these beams transmitted through the crystals were made to interfere with each other. Detector D_1 was used to measure the fringe speed from which the detuning δ was inferred. Detector D_2 gave the oscillation intensity. A 100-μm pinhole was used to stabilize oscillation in the resonator[18]. The frequency detuning and oscillation intensity showed periodicity in Ψ with period 2π (or equivalently in L with period $\lambda/2$). Fig. 5.8 shows one period of detuning δ and the oscillation intensity as a function of the combined pumping phase Ψ. Similar experiments in which the oscillation beams beated directly against light at the pump frequency ω_{pump} split directly off the laser output have been performed. The detunings were equal and opposite in sign, consistent with the theory.

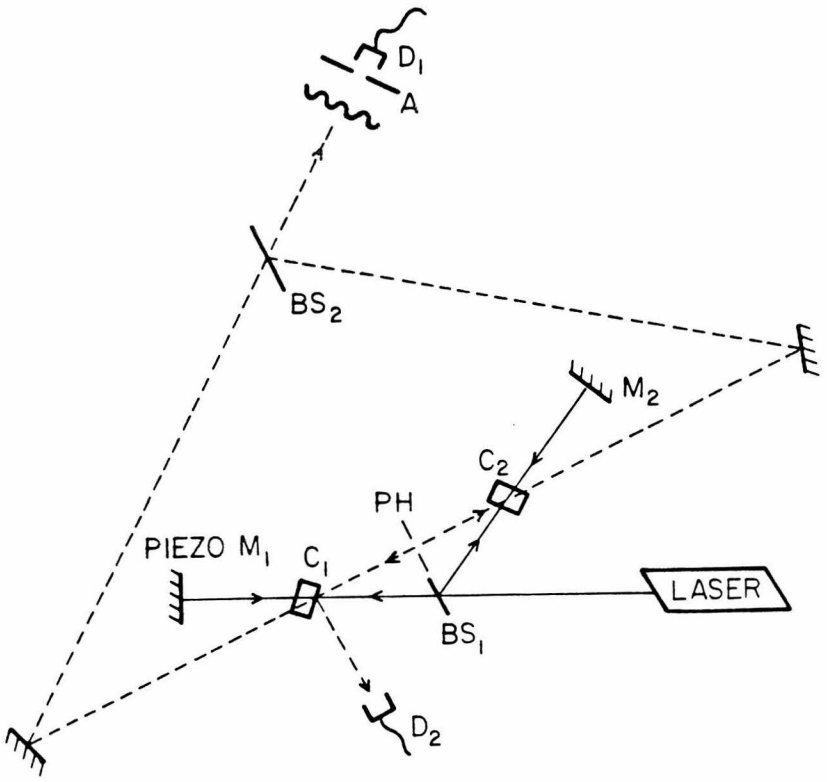

Fig. 5.7: The experimental arrangement used to demonstrate oscillation detuning in the double phase conjugate resonator. An argon ion laser was used at 514.5nm in single longitudinal and TEM_{00} modes. The power output was 100 milliwatts. Using a Cartesian coordinate system with the abscissa coincident with the beam leaving the laser locations of the elements measured in centimeters were: beam splitter BS_1 (0,0), $BaTiO_3$ crystal C_1 of PCM_1 (-8.9,0), $BaTiO_3$ crystal C_2 of PCM_2 (8.9,7.6), piezo-mirror M_1(-19,0), mirror M_2(17.8,15.3). The c-axis of C_1 pointed in the direction of the vector (0.95,-0.30), the c-axis of C_2 in the direction (0.91,-0.42). The c-axis is defined here as pointing towards the surface which had been connected to the negative electrode at poling. A 100-μm pinhole PH was inserted in the resonator to stabilize the oscillation. Detector D_1 was placed behind aperture A at the output of the interferometer to measure the detuning. Detector D_2 monitored the oscillation intensity using a Fresnel reflection from the surface of crystal C_1.

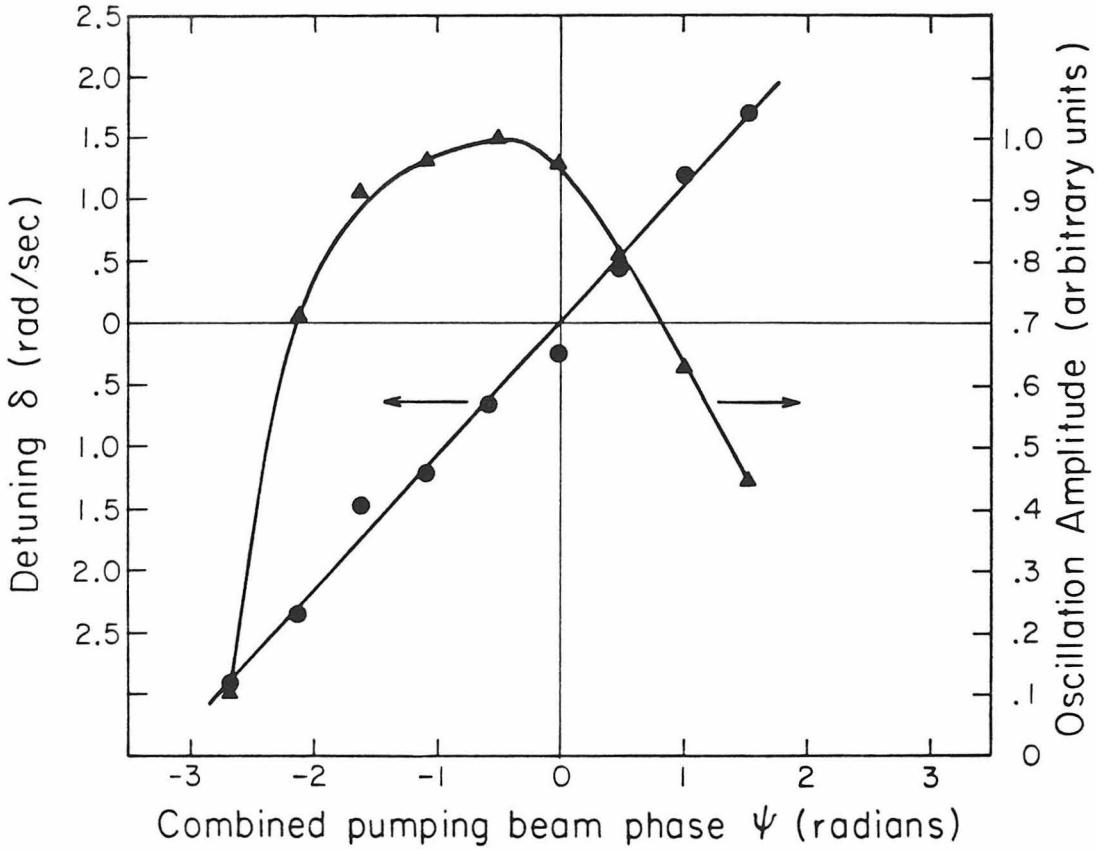

Fig. 5.8 : The experimental results showing the detuning and oscillation intensity as a function of the combined pumping beam phase derived from the position of piezo-mirror M_1.

If the detuning effect is thermal in origin, the amount of detuning should be related to the intensity of light in the crystal. This possibility may be ruled out by referring to the experimental data of Fig. 5.8, which show that for each value of total intensity in the crystal there are two possible signs for the associated detuning. Also, there are values of Ψ near ± 3 where no oscillation is observed. This prohibition of oscillation because of an unfavorable pumping phase is again inconsistent with a thermal effect. The results are, moreover, in qualitative agreement with the theoretical analysis above.

(5.4) Applications

In this section, two applications of resonators with photorefractive gain are discussed; they are: (a) the optical path length to frequency conversion interferometer; and (b) the one-way, real time wave front convertors. Optical bistabilities and associative memories will be discussed in Chapters 5 and 6, respectively. Other applications such as distortion correction in laser cavities[19], laser gyroscopes[10,20], and self-scanning of a cw dye laser[21-23] have been reported separately.

(5.4a) Optical Path Length to Frequency Convertion Interferometers

In traditional interferometery, changes in optical path length cause changes in fringe position at the output of an interferometer. This change in fringe position is inferred by intensity measuring detectors. The precision of these devices might thus be limited by the precision with which intensity measurements can be made.

Frequency can often be measured with much higher precision than intensity. Therefore an interferometer whose output can be measured by a frequency counter will benefit from this improved precision. Many types of photorefractive oscillator including the ring resonator (Fig. 5.3), the double phase conjugate resonator (Fig. 5.7) and the linear PPCM[4] can be used in this manner[1,3].

4.4(b) One-way, real time wave front convertors

Many laser systems give rise to highly distorted laser beams. The distortion is due mostly to optical 'imperfections' and aberrations in the laser resonator (including those of the pumped gain medium) or in transmission through a distorting medium. The question arises as to the possibility of beam 'cleanup', i.e., of improving the spatial properties of the beam, in real time.

A number of schemes were described recently in which Stimulated Raman Scattering (SRS) was used to amplify a 'clean' Stokes seed beam by a highly distorted pump beam[24]. The basic physical idea is that power can be transferred continuously from the distorted pump beam to the Stokes beam without transferring the phase, i.e., distortion of the former. The distortion phase increment is transferred, instead to the locally excited molecular vibration.

The mathematical nature of the Raman (or Brillouin) nonlinearity is similar to that of the photorefractive effect. In each of these the presence of two beams

$$\vec{E}_1(\vec{r},t) = \frac{1}{2}\,\vec{E}_{10}(\vec{r})\; e^{i(\omega_1 t - \vec{k}_1\cdot\vec{r})} + \text{c.c.} \qquad [5.42a]$$

$$\text{and}\quad \vec{E}_2(\vec{r},t) = \frac{1}{2}\,\vec{E}_{20}(\vec{r})\; e^{i(\omega_2 t - \vec{k}_2\cdot\vec{r})} + \text{c.c.} \qquad [5.42b]$$

gives rise to a nonlinear polarization[8,25]

$$P_{NL}(\vec{r},t) = \frac{i\gamma'(\vec{E}_{10}^{*}\cdot\vec{E}_{20})E_{10}}{1+i[(\omega_1-\omega_2)-\omega']\tau} e^{i(\omega_2 t-\vec{k}_2\cdot\vec{r})} + c.c. \qquad [5.43]$$

where ω' is some characteristic frequency of the medium, τ is a damping time, and γ' represents the strength of the coupling between $\vec{E}_{10}$ and $\vec{E}_{20}$, which is related to the physical mechanism of the nonlinear interaction and where for the sake of simplicity we adopted scalar notation. The imaginary part of P_{NL}, in quadrature with $\vec{E}_{20}$, gives rise to an amplification of $\vec{E}_{20}$ (the Stokes beam) by $\vec{E}_{10}$. This polarization then radiates thus causing transfer of power from ω_1 to ω_2.

This formal similarity between SRS and photorefractive two-beam coupling suggests that one can achieve beam cleanup using photorefractive nonlinear optical techniques. An advantage of using a photorefractive medium is that it can be operated at low power, mW, while SRS requires high beam power to reach the threshold.

In the experiment the cleaned up beam does not result from injecting and amplifying a seed input[26] but is a self generated a mode of an optical resonator pumped by the distorted beam. The experimental setup is similar to Fig. 5.9. The distorted pump beam $\vec{E}_{10}$ is incident on a poled $BaTiO_3$ crystal placed inside a ring oscillator. The photorefractive two-beam coupling described in Chapter 3 provides gain which enables a mode $\vec{E}_{20}$ of the ring resonator to oscillate. The spatial characteristics of the mode $\vec{E}_{20}$ are determined by the resonator and ideally, not the pump beam thus leading to beam cleanup.

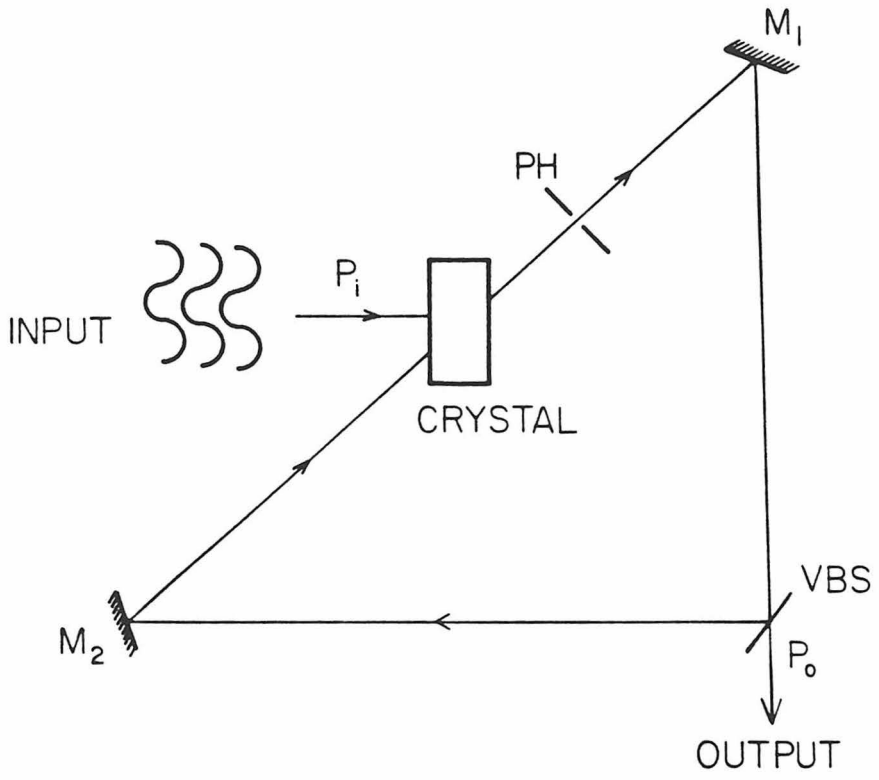

Fig. 5.9 : Schematic diagram of a wave front convertor.

A fundamental figure of merit for the wavefront converter is the ratio G of the photometric brightness (W/m^2-Sr) of the output beam to that of the input. This ratio is

$$G = \left(\frac{P_o}{P_i}\right)\left(\frac{\theta_i}{\theta_o}\right)^2\left(\frac{A_i}{A_o}\right) \qquad [5.44]$$

where θ_o and θ_i refer to the beam spreading angle at the output and input respectively, and $A_{o,i}$ and $P_{o,i}$ are the respective beam diameters and powers. We note that in passive optical systems G<1.

In the experiment a TEM_{00} mode Argon laser beam (514.5nm, 50mW, beam diameter 1.5mm and beam divergence .5 mrad) was passed through a distorting medium. The distortion media used in these experiments were prepared by etching pieces of glass (1mm thickness) in 48% hydrofloric acid for 1 min. A piece of etched glass can cause the beam divergence to increase to about 50 mrad. A ring resonator (L = 40cm) was placed about 5cm behind the distortion medium. The ring resonator consists of two 99% reflecting mirrors, a variable beam splitter (VBS) serving as the output coupler, and a poled $BaTiO_3$ crystal. By introducing an intracavity aperture with a diameter <0.4mm, the higher order modes of the ring resonator were suppressed and oscillation in a steady TEM_{00}-like mode resulted. Several types of distorting media (both thin and thick) have been used.

The very considerable improvement in the spatial characteristics of the mode is evident in a comparison between Fig. 5.10(f) and 5.10(g). The output (oscillating beam) beam has beam waist and divergency equal to .4mm and 1.15 mrad respectively. The maximum power

Fig. 5.10

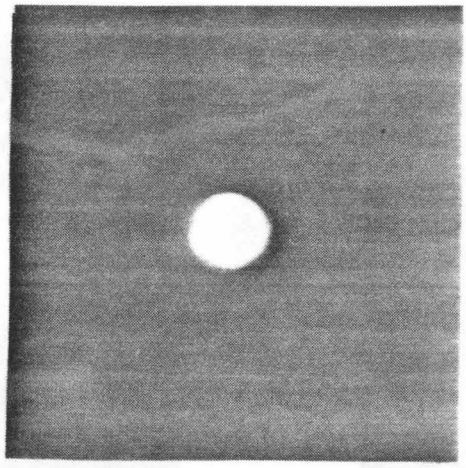

(a) Undistorted laser beam;

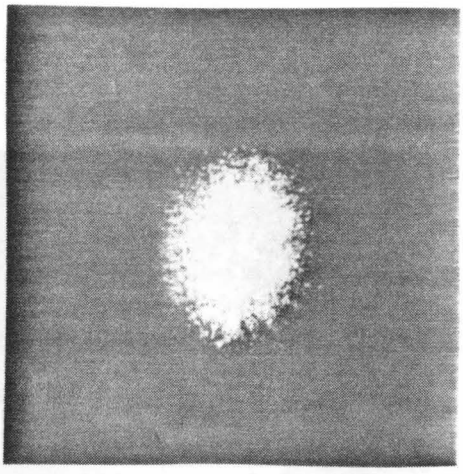

(b) laser beam after passing through a distortion medium without correction;

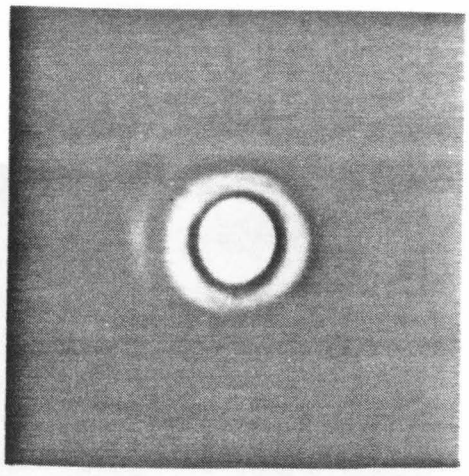

(c) the corresponding corrected output beam;

Fig. 5.10

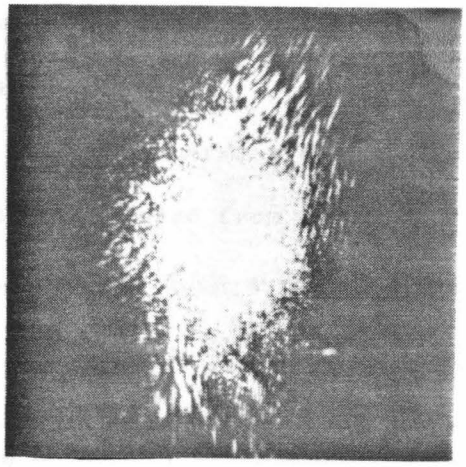

(d) laser beam after passing through a distortion medium formed by two pieces of etched glass stacked together;

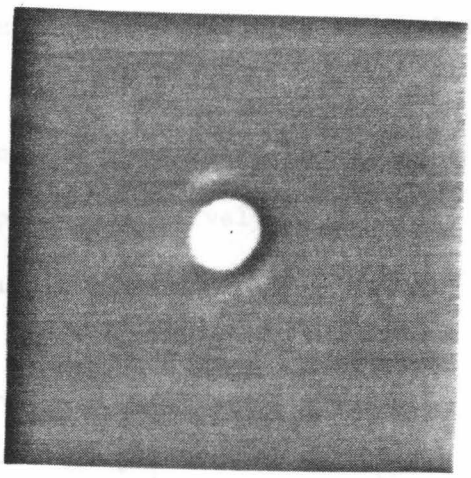

(e) the corresponding corrected output beam;

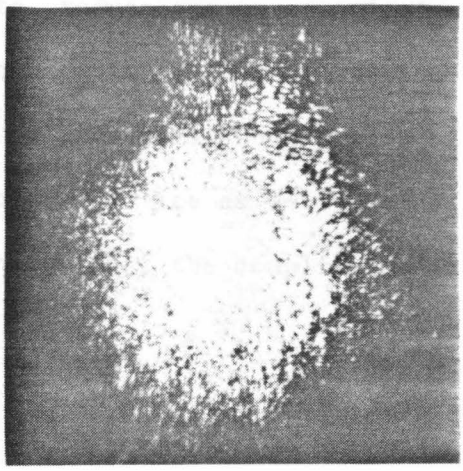

(f) laser beam after passing through a thick distortion formed by three pieces of etched glass, each of them separated by 1 inch;

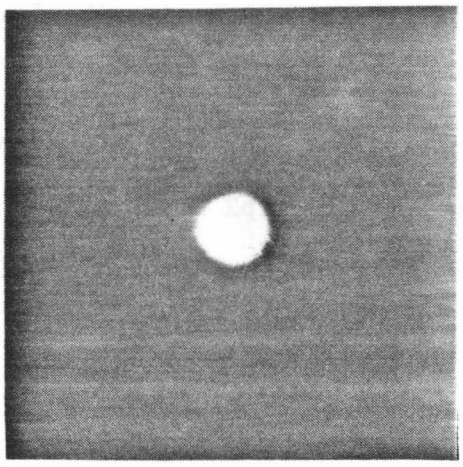

(g) the corresponding corrected output beam.

conversion efficiency $\eta = P_o/P_i$ measured was 15% which corresponding in a wavefront conversion figure of merit G=4000. This is to be compared with the results using spatial filtering techniques which yield $\eta < 0.1\%$ and G<1.

The power conversion efficiency η of the wave front converter can be calculated from a recent theory for photorefractively pumped oscillators[3,8]. Such a theory leads to a result

$$\eta = \frac{(1-R)}{R}\left[\frac{1 - \exp\left(-\frac{2\gamma_o \ell f_o}{1 + 4(\omega_2-\omega_1)^2 t_2^2}\right)}{1 - R\, e^{-\alpha\ell}} - 1\right] \qquad [5.45]$$

where ω_1 and ω_2, we recall, are the frequencies of the pump and the oscillation beam respectively, t_2 is the photon life time of the passive ring resonator, and f_o is the overlap integral given by Eq. [5.34]. We note that the effect of distortion of the pump beam $\vec{E}_{10}$ is to reduce the "projection" of $\vec{E}_{10}$ on $\vec{E}_{20}$ leading to a smaller f_o and thus to a smaller conversion efficiency.

Fig. 5.11 shows a plot of the measured power conversion efficiency of our device as well as the theoretical values from Eq. [5.45], we noted that the coupling constant $\Gamma\ell$ equals to

$$\Gamma\ell = \frac{2\,\gamma_o\,\ell\,f_o}{[1+4(\omega_2-\omega_1)^2 t_2^2]} \qquad [5.46]$$

The theoretical curves agree quite well with experimental data when $\alpha\ell = 1.11$ and $\Gamma\ell = 3.6$. From independent experiments, we also measured $\alpha\ell = 1.11$ and $\Gamma\ell = 3.4$.

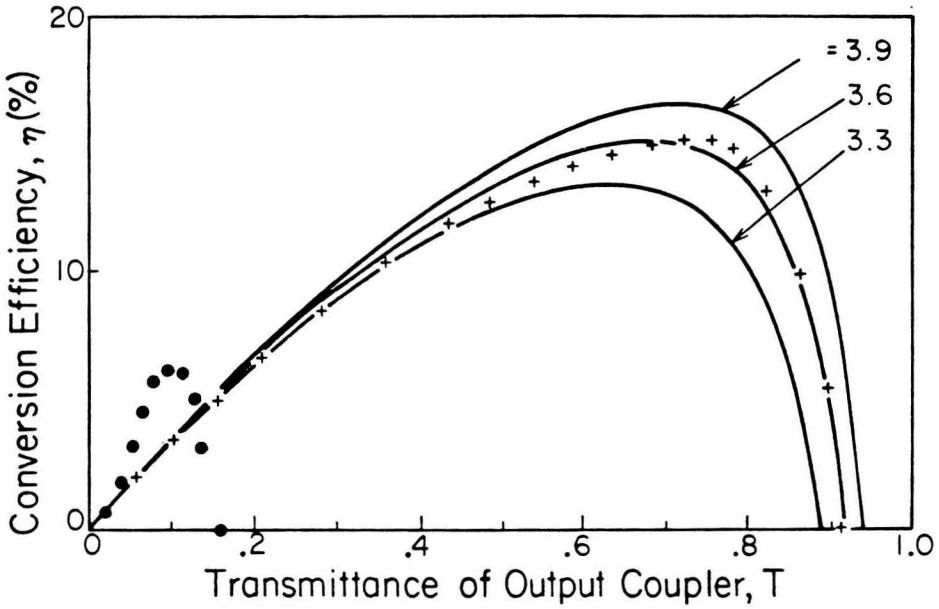

Fig. 5.11: Conversion efficiency η versus transmittance T=1-R of the output coupler (VBS). (+) and (•) are experimetal points using ring oscillator (Fig. 5.9) and ring PPCM (Fig. 5.14 d). The continous lines are theoretial plots based on Eq. [5.45], for $\alpha\ell$=1.11, and κ=3.3, 3.6 and 3.9.

From Eq. [5.45], the maximum conversion efficiency, η_{max}, is derived for given $\alpha\ell$ and $\Gamma\ell$,

$$\eta_{max} = \frac{(e^{-\alpha\ell} + e^{-\Gamma\ell})\left[1 + \sqrt{1 - e^{\alpha\ell} - e^{\Gamma\ell} + e^{(\alpha\ell+\Gamma\ell)}}\right] - 2}{\sqrt{1 - e^{\alpha\ell} - e^{\Gamma\ell} + e^{(\alpha\ell+\Gamma\ell)}} - 1} \qquad [5.47]$$

at the transmitivity of the output coupler, R_{max},

$$T_{max} = 1 - \frac{e^{-\Gamma\ell}\left[1 - \sqrt{1 - e^{\alpha\ell} - e^{\Gamma\ell} + e^{(\alpha\ell+\Gamma\ell)}}\right]}{e^{-\alpha\ell} + e^{-\Gamma\ell} - 1} \qquad [5.48]$$

Theoretical plots of η_{max} and T_{max} as a function of $\Gamma\ell$ for various $\alpha\ell$ are shown in Figs. 5.12 and 5.13 respectively. We note that η_{max} is saturated for given $\alpha\ell$. On the other hand, the $\alpha\ell$ should not be too small because it is required for the photorefractive effect.

Other resonator configurations instead of a ring oscillator have also been employed, Fig. 5.14. These included the linear, the semi-linear, the ring cavity and the two interaction region PPCMs which are discussed in section 4.6. They all led to impressive spatial mode cleanup but with smaller power conversion (≃6%). This may be due to the fact that in these cases a good deal of power is phase conjugated back to the pump. One advantage of the devices in Fig. 5.14c and 5.14d is that they can be pumped with light sources of short coherent length or even with mode locked laser light[28]. This is because of the semi-linear and the ring PPCM used dynamic transmission holograms which are insensitive to vibration.

The small frequency shift (section 5.1) between the pump and the oscillating beam which exists in these oscillators (a few Hz) is probably of little consequence in most practical situations but should be noted.

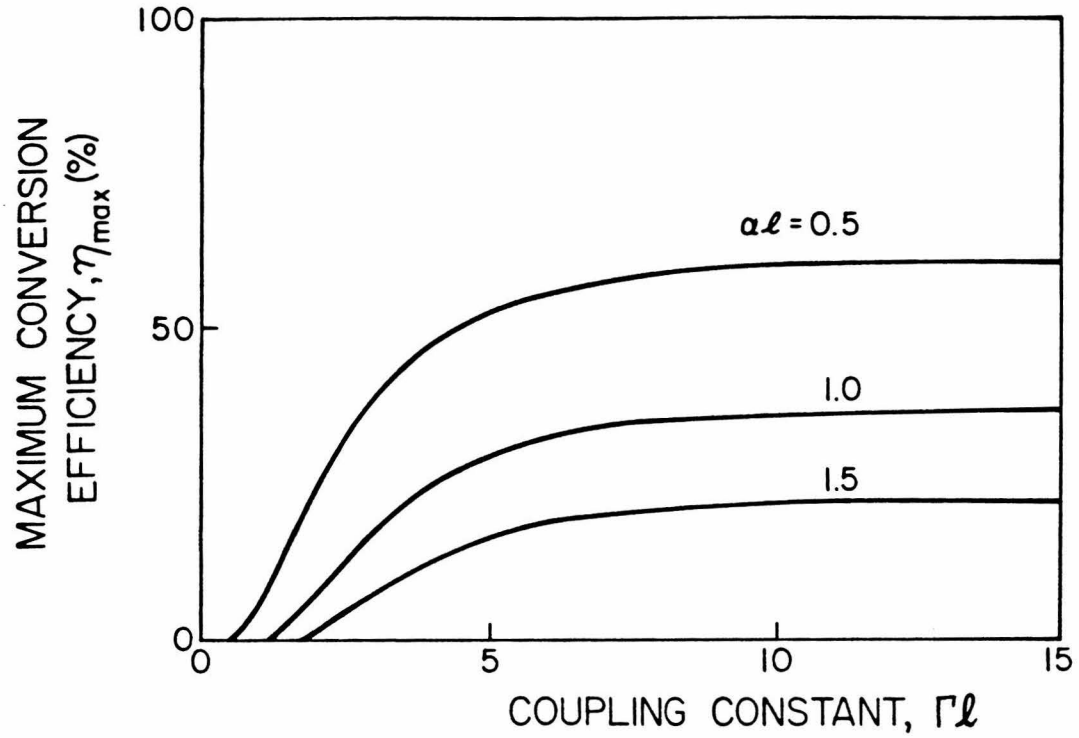

Fig. 5.12: Maximum conversion efficiency η_{max} versus modified coupling constant $\Gamma\ell$ with $\alpha\ell$ = .5, 1.0, 1.5.

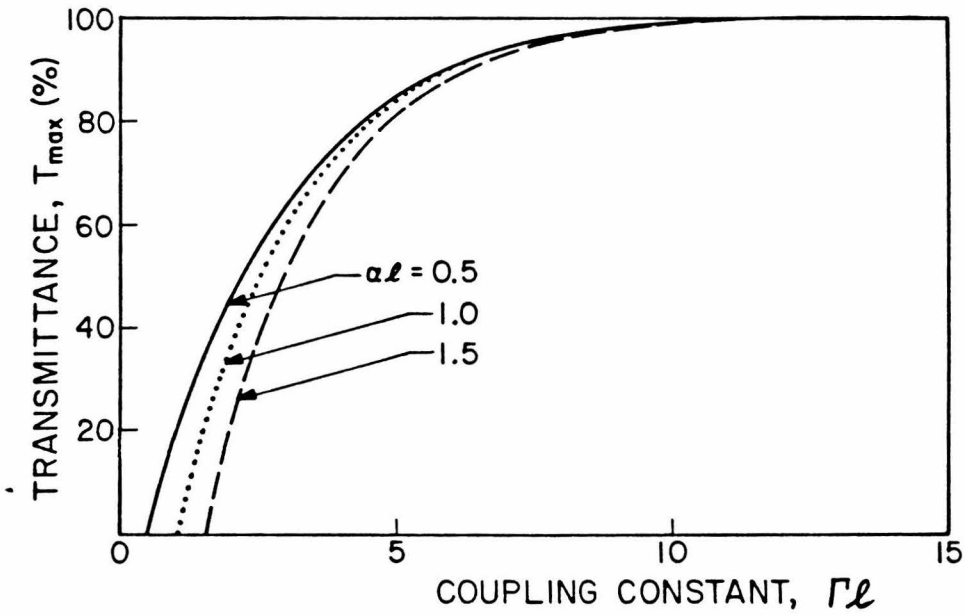

Fig. 5.13: Transmitivity of output coupler at maximum conversion efficiency T_{max} versus modified coupling constant $\Gamma\ell$.

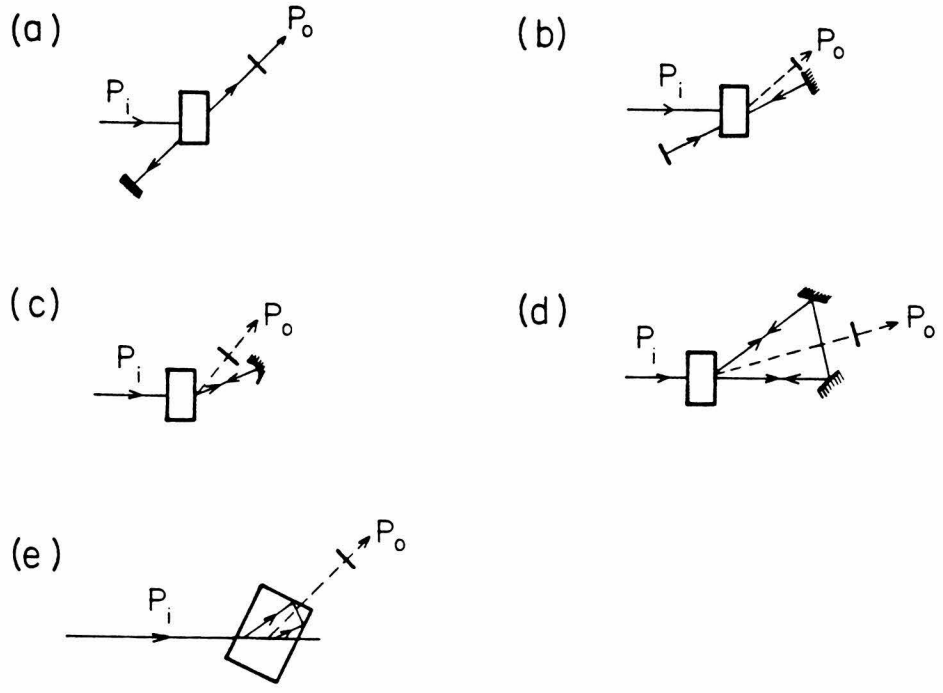

Fig. 5.14: Wave front converters using other oscillation configurations: (a) linear PPCM with output taken from the self-induced pumping beam (b) linear PPCM with a self-induced oscillation (c) semi-linear PPCM with an self-induced oscillation (d) ring PPCM with a self-induced oscillation (e) two interaction region PPCM with a self-induced oscillation.

References for Chapter 5:

1. S.-K. Kwong, M. Cronin-Golomb, and A. Yariv, to be published in IEEE Quant. Electron., special issue on "Dynamic gratings and four-wave mixing", July, 1986.
2. J.O. White, M. Cronin-Golomb, B. Fischer and A. Yariv, Appl. Phys. Lett. pp. 450-452 (1982).
3. S.-K. Kwong, A. Yariv, M. Cronin-Golomb and I. Ury, Appl. Phys. Lett. **47**, 460-462 (1985).
4. M. Ewbank and P. Yeh, Opt. Lett. **10** 496-498 (1985).
5. H. Rajbenbach and J.P. Huignard, Opt. Lett. **10** pp. 137-139 (1985)
6. M. Cronin-Golomb, B. Fischer, S.K. Kwong, J.O. White and A. Yariv, Opt. Lett. **10** pp. 353-355 (1985).
7. J. Fienberg, and R.W. Hellwarth, Opt. Lett. **5**, 519; Erratum Opt. Lett. **6**, 257, 1981.
8. A. Yariv and S.-K. Kwong, Opt. Lett. **10** pp. 454-456 (1985).
9. P. Yeh, J. Opt. Soc. Am. B, **2**, 1924, 1985.
10. P. Yeh, Appl. Opt. **23** pp. 2974-2978 (1984).
11. S.-K. Kwong, M. Cronin-Golomb, B. Fischer and A. Yariv, J. Opt. Soc. Am. **A3**, 157, 1986.
12. W. E. Lamb, Jr., Phys. Rev. 134, (6A), A1429 (1964).
13. A. Yariv, Quantum Electronics, 2nd ed., John Wiley & Sons, New York, Inc. (1975).
14. J. C. Slater, Microwave Electronics, Van Nostrand, Princeton, N.J. (1950).

15. A. Yariv, Optical Electronics, 3rd Ed., Holt, Rinehart and Winston, Inc. (1985) Equation (6.4-13), p. 159.

16. S.I. Stepanov, V.V. Kulikov and M.P.Petrov, Opt. Commun. 44 pp. 19-22 (1982).

17. Ph. Refregier, L. Solymar, H. Rajbenbach, and J.P. Huignard and Ph. Refregier, J. Appl. Phy. 58 pp. 45-57 (1985).

18. G.C. Valley and G.J. Dunning, Opt. Lett. 9, pp. 513-515 (1984).

19. M. Cronin-Golomb, B. Fischer, J. Nilsen, J.O. White and A. Yariv, Appl. Phys. Lett. 41 219-220 (1982).

20. B. Fischer and S. Sternklar, Appl. Phys. Lett. 47 1-3 (1985).

21. W.B. Whitten and J.M.Ramsey, Opt. Lett 9 pp. 44-46 (1984).

22. J. Feinberg and G.D. Bacher, Opt. Lett. 9 pp. 420-422 (1984).

23. J.M. Ramsy and W.B. Whitten 10 362-364 (1985).

24. There was a session on 'Beam Cleanup and Beam Combining' at the Conference on Lasers and Electro-optics CLEO'85, Technical Digest WA1-5 and WG1-5.

25. A. Yariv, Quantum Electronics, 2nd Ed., John Wiley and Sons, New York, Inc. (1975), Chapter 18, Equation (18.4-13).

26. A.E.T. Chiou and P. Yeh, Opt. Lett. 10, 621, 1985.

27. M. Cronin-Golomb, J. Paslaski and A. Yariv, Appl. Phys. Lett. 47 pp. 1131-1133 (1985).

Chapter 6: Optical bistability with self-pumped phase conjugate mirrors

In chapter 4, it was already mentioned that at large coupling constants $\gamma\ell$ and at certain regions of probe and pumping beam ratios, both the magnitude[1] and the phase[2] of the phase conjugate beam theoretically have multiple solutions. However, so far, these multiple solutions have not been experimentally verified.

This chapter, instead of seeking the 'intrinsic' multiple solutions in four-wave mixing, will study the bistability of a self-pumped phase conjugate mirror with nonlinear feedback. The results have potential applications in the fields of optical memory, switching devices, and pattern recognition. In the following, two kinds of bistable devices will be described. They are: (6.1) bistability of a self-pumped phase conjugate mirror with a feedback erasing beam;[3] and (6.2) bistable oscillations with a self-pumped phase conjugate mirror.[4]

(6.1) Bistability and hysteresis of a semilinear self-pumped phase conjugate mirror with a feedback erase beam

The basic experimental arrangement is shown in Fig. 6.1. The Argon laser (514nm) beam after passing through polarizer P_1 is polarized in the plane of the figure. The poled $BaTiO_3$ crystal and the curved mirror M_2 form the semilinear passive phase conjugate mirror as

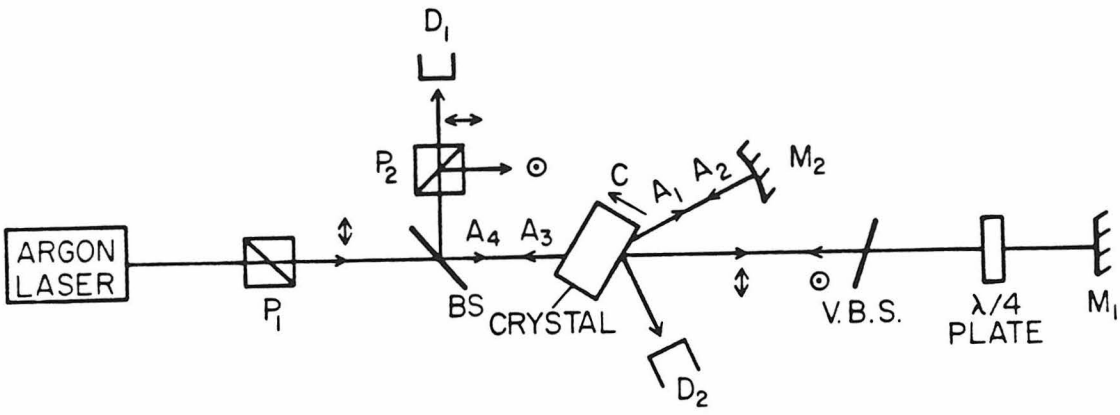

Fig. 6.1 : The experimental arrangement of the optical bistable device. The laser used in the experiment is an argon ion laser operating at 488nm wavelength and 2.3 mm beam diameter. The incident laser beam power on the crystal is 340 mW. The crystal is a poled $BaTiO_3$ crystal with dimension 5x5x4 mm and the C-axis is parallel to the 5mm surface. M_2 is the curved mirror with radius of curvature 5cm. BS is a beam splitter. P_1 and P_2 are polarizing beam splitters. VBS is the variable beam splitter. M_1 is a mirror. A Pockels cell was used as a quarter-wave plate.

described in section 4.6. The light beam from the laser after passing through the crystal generates a broad fan[5] of amplified scattering toward the external curved mirror which is used to reflect the fanning light back into the crystal. This seeds oscillation between the crystal and the curved mirror. This oscillation composed of beams A_1 and A_2 is supported by a phase grating formed inside the crystal so that light is continuously diffracted from the input beam A_4 by the grating into the oscillation cavity. The oscillating beams inside the cavity supply the necessary pumping to generate the phase conjugate beam A_3 monitored by detector D_1. Simultaneously, an orthogonally polarized light beam is fed back by the mirror M_1 into the crystal to erase the phase grating. This feedback beam is attenuated by the variable beam splitter VBS. The detector D_2 detects the reflection of the feedback erase beam from the crystal surface. The polarizer P_2 is used to discriminate the phase conjugate output from the feedback erase beam. An orthogonally polarized erase beam is used to ensure that it only erases the phase grating and does not write its own grating. This is a result of the small electrooptic coefficient of the crystal at this polarization. In fact, we demonstrated experimentally that the device works if we simply remove the polarizer P_1 and P_2, and replace the VBS, M_1, and quarter wave plate by a single VBS which controls the feedback erase beam. In the latter case, the VBS is tilted at a small angle so that detector D_1 does not detect the reflected beam from the VBS. The bistable behavior can be explained as follows.

The plane wave theory of the semilinear PPCM has been described in Ref. 6. The threshold coupling strength above which it is possible for

the semilinear PPCM to operate is given by

$$(\gamma\ell)_t = (1 + M_2)^{1/2} \ln \left[\frac{(1 + M_2)^{1/2} - 1}{(1 + M_2)^{1/2} + 1} \right] \qquad [6.1]$$

The fanning effect, interpreted as the two beam coupling amplification of scattered light may also be described in terms of this coupling constant and the fraction χ of the incident intensity I_{in} scattered by the crystal into the fanning direction. If χ is assumed small, then the intensity I_f of light leaving the crystal as amplified scattering may be expressed as (similar to the two-beam coupling expression shown in Eq. [3.14])

$$I_f = \frac{I_{in}}{1 + e^{\gamma\ell}/\chi} \qquad [6.2]$$

In reality, the fanning light is generated in a wide solid angle. Since the coupling constant γ depends on the direction of the wave vector of the grating it describes, the above description of fanning in terms of a single value of the coupling constant is necessarily approximate.

The oscillation beams A_1 and A_2 are generally confined to a smaller solid angle so that the description of the semilinear mirror in terms of a single coupling constant is more accurate, though still approximate. Also these models assume that the beam intensities are uniform across their phase fronts where in reality the beams are at

least approximately Gaussian. These approximations, notwithstanding, still allow us to proceed to a qualitative understanding of the operation of the device.

An experimental curve is shown in Fig. 6.2, which was taken by continuously changing the reflectivity of the VBS. At point A the intensity of the erase beam is zero, and we have pure semilinear mirror operation. As the attenuation of the VBS is decreased the intensity I_e of the erase beam rises. This beam does not contribute to the writing of any significant gratings, since it is of ordinary polarization; its effect is to saturate the coupling constant

$$\gamma\ell = \frac{(\gamma\ell)_o}{1 + I_e/I_+} \qquad [6.3]$$

where I_+ is the total intensity of beams A_1, A_2, A_3 and A_4 participating in four wave mixing in the PPCM. As I_e rises the phase conjugate reflectivity drops. When the point B is reached, the coupling strength is driven below threshold, the PPCM stops working and the reflectivity falls to zero at point C. The light in the crystal-M_2 cavity is now just due to fanning, not oscillation. Mirror M_2 reflects this light back to the crystal where it contributes to the saturation of the coupling constant:

$$\gamma\ell = \frac{(\gamma\ell)_o}{1 + (I_e + I_f)/I_+} \qquad [6.4]$$

Now as the intensity of the erase beam is decreased, the fanning light continues to depress the coupling constant and oscillation does

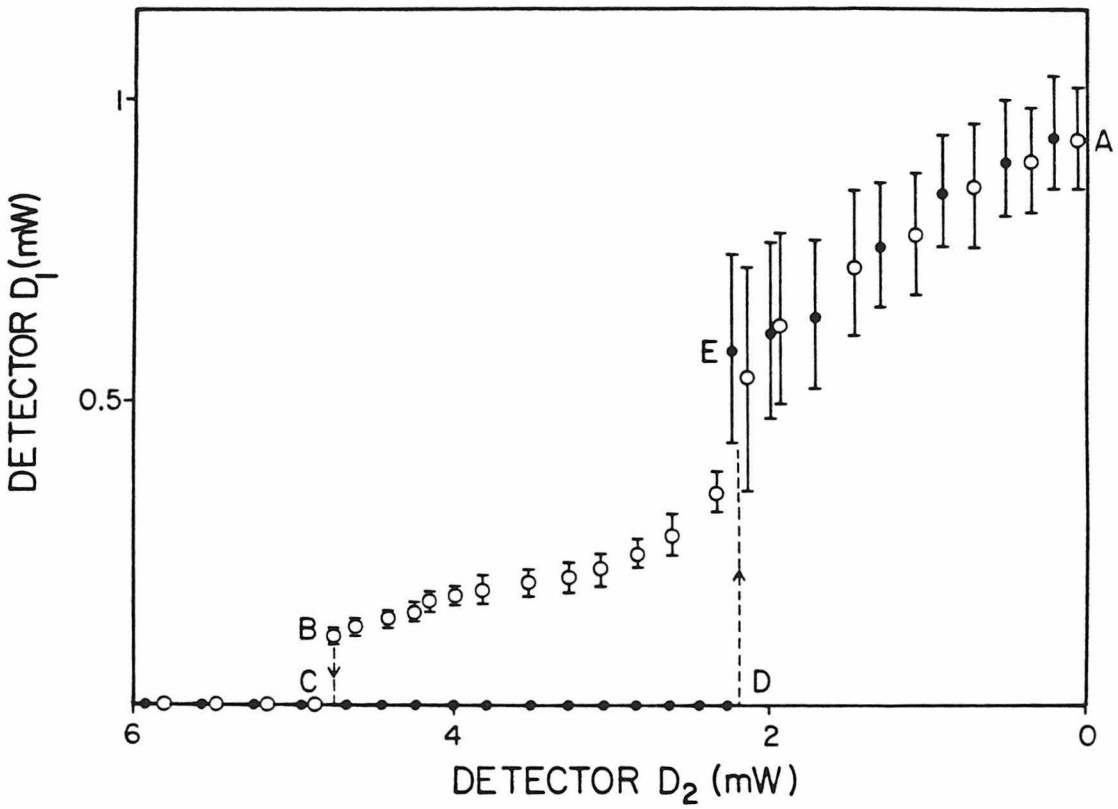

Fig. 6.2 : The experimental data of phase conjugate output against the transmitted erase beam power. The O and • are the points taken when the erase beam is increasing and decreasing respectively.

not again reappear until the point D when the coupling constant again reaches threshold and jumps with the collapse of the fanning into oscillation to a value well above threshold corresponding to reflectivity at point E.

On the basis of this explanation it might be expected that with the transitions between fanning and PPCM operation, the erase beam intensity I_e should also change discontinuously. That such a jump in I_e is not observed experimentally is somewhat surprising, and is the subject of current investigations.

In the experiment, a temporal oscillation of phase conjugate output with period 8.0±0.5 seconds was also observed. The period of oscillation was inversely proportional to the input laser power and independent of the feedback erase beam power. The cause of this oscillation at the output may be due to the mode competition in the multimode oscillation cavity (crystal-curved mirror).[7]

This device has two distinctive features:

(1) since beams A_1 and A_2, A_3 and A_4 are phase conjugate pairs, any phase aberration along these optical paths can be easily corrected.

(2) the 'ON' and 'OFF' state can be controlled by any incoherent light or even with light of a different wavelength as long as it can erase the grating inside the crystal.

A typical measured rise time and erase time curve of the device in Fig. 6.1 are shown in Fig. 6.3a and 6.4a. Since neither of these curves is exponential , we arbitrarily define the time required to reach 90% and 10% of the maximum output as the rise time constant t_r

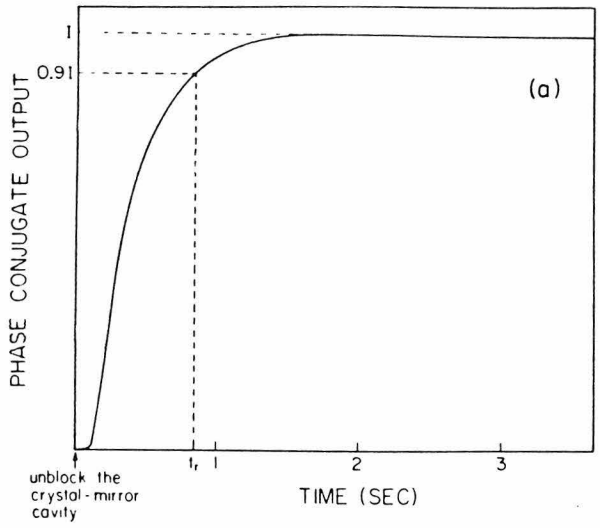

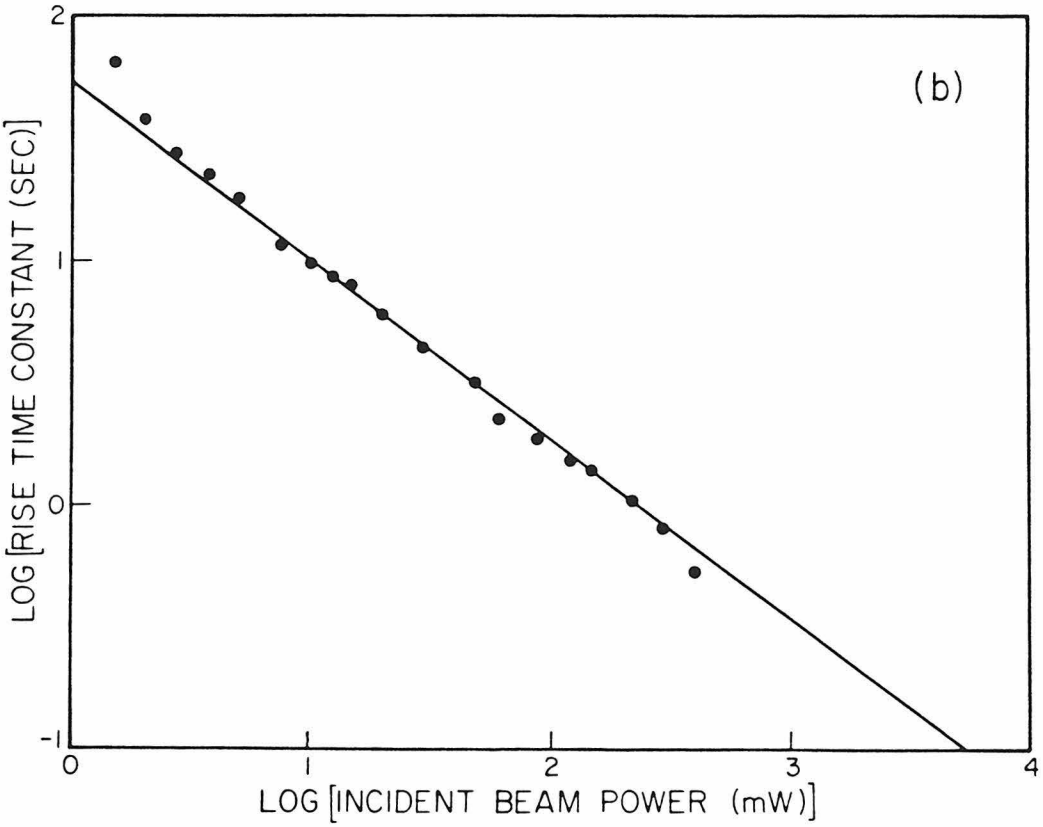

Fig. 6.3 : (a) A typical turn on time curve of the device in Fig. 6.1

(b) An experimental plot of rise time constant against the incident beam power in the absence of an erase beam. The slope of the best fit straight line is 0.74. The crystal used in the experiment is a $BaTiO_3$ crystal.

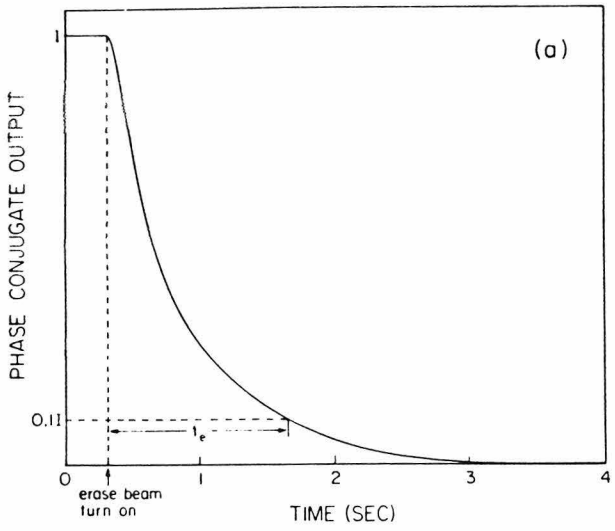

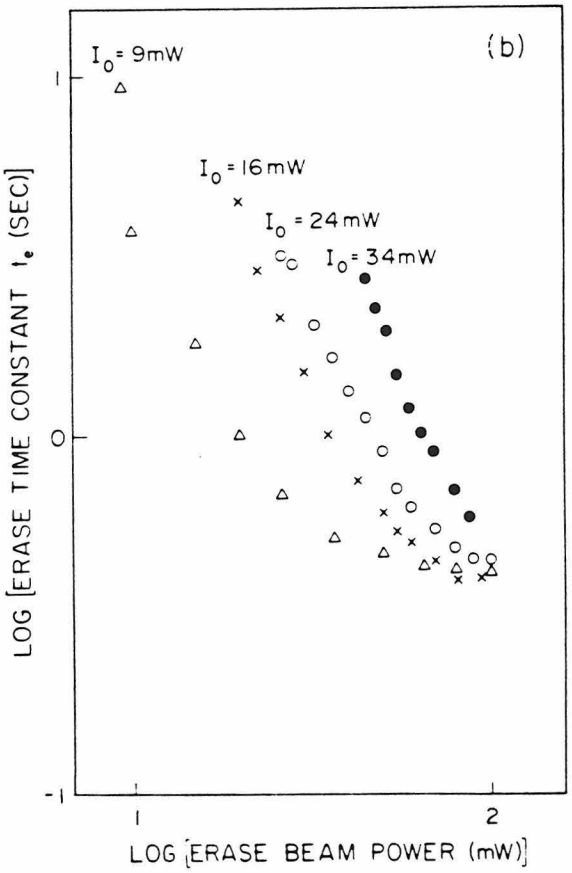

Fig. 6.4 : (a) A typical turn off curve of the device in Fig. 6.1.

(b) An experimental plot of the erase time constant against the erase beam power for several incident beam powers.

and the erase time constant t_e, respectively. Fig. 6.3b shows a plot of the measured rise time constant against input beam power with no erase beam. Except at very high or very low beam power, the data may be described moderately well with a straight line which corresponds to the relationship $t_r I_o^{0.74} =$ constant. Fig. 6.4b illustrates the measured erase time constant against the erase beam power for various input beam power I_o . The curves indicate the time constant is longer for larger I_o with the same erase beam power. The erase time constant seems to be bounded by certain limit even at very high erase beam power, which may be due to a carrier saturation effect in the photorefractive crystal.

Fig. 6.5 illustrates a proposed switching scheme. By adjusting the VBS and the average input power of the control beam to the point where the device will be operate at the hysteresis region of Fig. 6.2. Then the input and output are related in fig. 6.6.

The bistable behavior reported in this experiment is unrelated to that observed in previous experiments with a Fabry-Perot cavity involving a photorefractive $LiNbO_3$ waveguide[8] in which at low optical powers, the change in refractive index in the intracavity medium was found to be intensity dependent, giving rise to standard Fabry-Perot bistability. The mechanism is also quite different from another proposed bistable device[9] in which light fed back to a fanning crystal discourages that fanning.

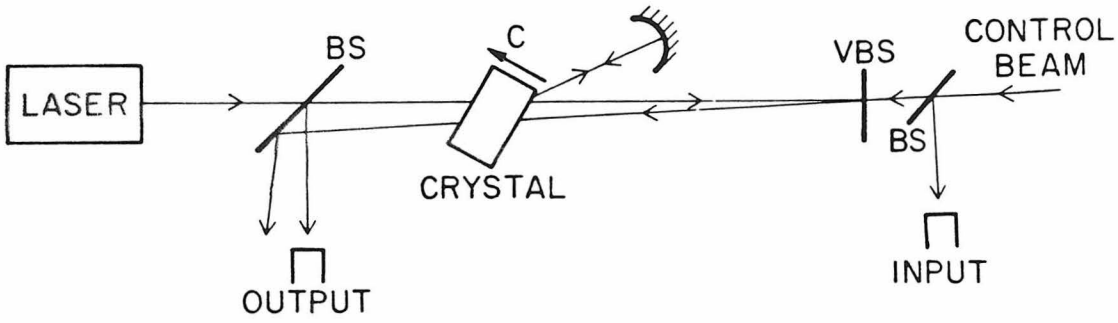

Fig. 6.5 : The proposed experimental arrangement to switch the bistable device in Fig. 6.1.

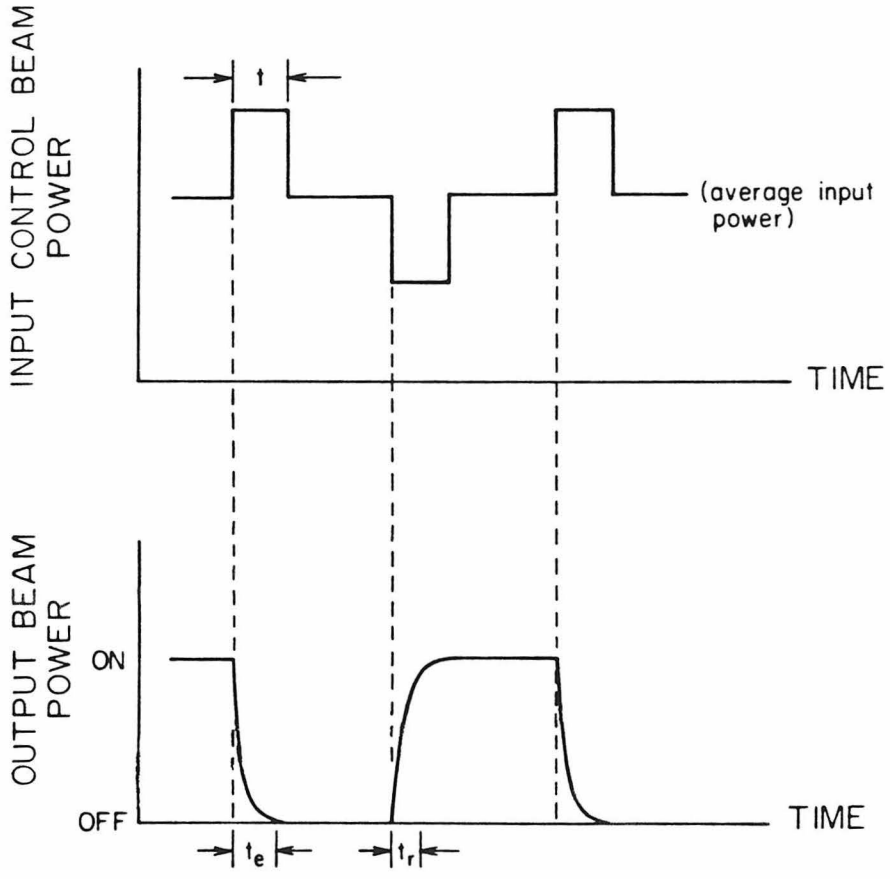

Fig. 6.6 : The input/output relationship of the device, where t, t_e and t_r are the switching pulse width, the erase and the rise times constants of the device respectively.

(6.2) Bistable oscillations with a self-pumped phase conjugate mirror

The device shown in Fig. 6.7 is based on a ring self-pumped phase conjugate mirror discribed in section 4.6. The oscillation takes place in the resonator consisting of the crystal and mirrors M_1 and M_2 with P_0 serving as the pump beam. This oscillation is referred to as the primary one and results in the appearance of a phase conjugate reflected beam P_1. Since P_0 and P_1 are a phase conjugate pair they should be capable of acting as pump beams for oscillation between a mirror (say M_3) and the pumped crystal[10]. This is verified experimentally and that oscillation in an auxiliary resonator (crystal-M_3) can be sustained by the primary oscillation in the ring resonator. However, if two auxiliary resonators were set up, the second one involving the crystal and M_4, then the two secondary oscillations cannot coexist, the result being a bistable mode of oscillation.

The experimental arrangement is shown in Fig. 6.7. The Argon ion laser (514nm, P_0=10mW) was operated in a TEM_{00} mode, but in a multi-longitudinal mode (without etalon) so that the coherent length L_c of the laser beam was about 7cm. The length of the ring cavity for the primary oscillation was L=34.5cm. The distances of the two auxiliary mirrors M_3 and M_4 from the crystal were L_1=14cm and L_2=20.5cm respectively. They were used to form auxiliary oscillations with the crystal. Notice that

$$|L-2L_i| < L_c \qquad i=1,2$$

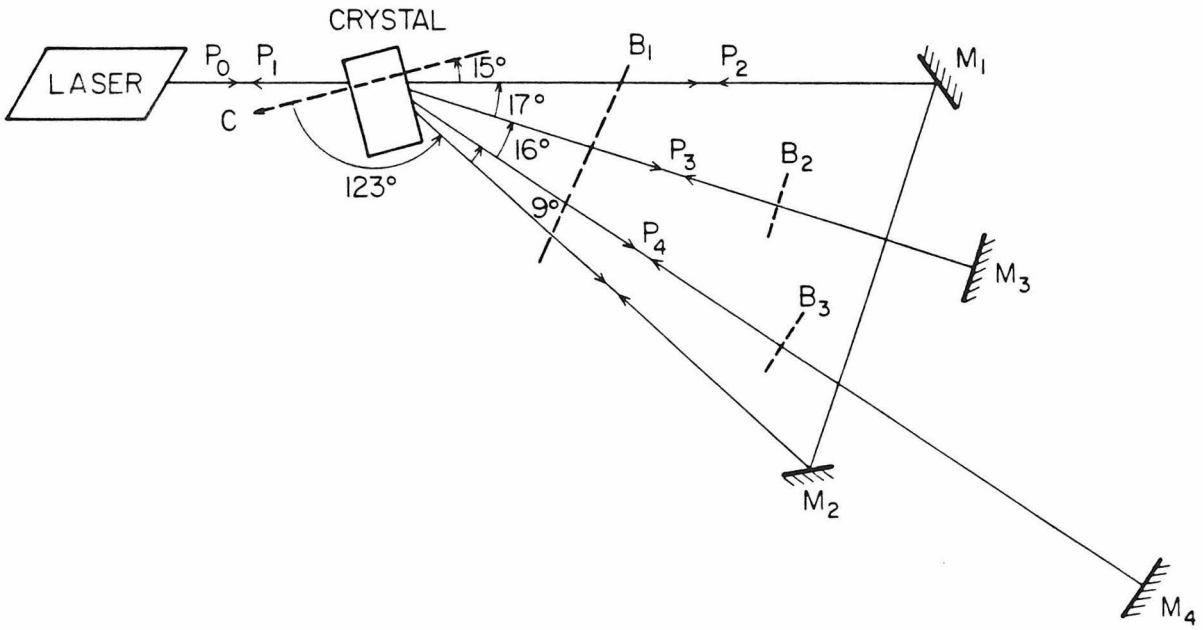

Fig. 6.7 : Experimental arrangement to observe bistable oscillations. M_1, M_2, M_3 and M_4 are mirrors of reflectivity $\simeq 1$. B_1, B_2 and B_3 are beam blocks.

and $2|L_1-L_2| > L_c$. [6.5]

These numbers are important in explaining the observed bistable behavior. Let P_0 be the power of the pumping laser beam, P_1 the power of the reflected phase conjugate beam, P_2 the power of the beam circulating anti-clockwise in the ring cavity, P_3 the power of oscillation between the crystal and mirror M_3, and P_4 the power of oscillation between the crystal and mirror M_4. B_1, B_2 and B_3 are beam blocks used to study the bistable oscillations. The experimental procedures and results are as follows:

[1] Initially B_1, B_2 and B_3 were inserted i.e., in the blocking position (• and o represent block and unblock in Fig. 6.8).

[2] When B_1 was removed, the primary oscillation built up. The phase conjugate reflectivity was about 1.26×10^{-2}. The small phase conjugate reflectivity was due to a slight intentional misalignment of the primary oscillation by tilting M_2 horizontally.

[3] When B_2 was removed, oscillation between the crystal and M_3 built up, and P_3 increased. Simultaneously, P_1 increased substantially and P_2 decreased. It seems that the auxiliary oscillation at M_3 dominated over the primary oscillation. The reason may be due to misalignment of the primary oscillation and the self-alignment of the auxiliary oscillation, so that the latter had an effectively larger coupling constant. P_2 decreased because its corresponding grating was partially washed out by the strong auxiliary oscillation beam.

[4] When B_3 was removed, the system remained unchanged and no oscil-

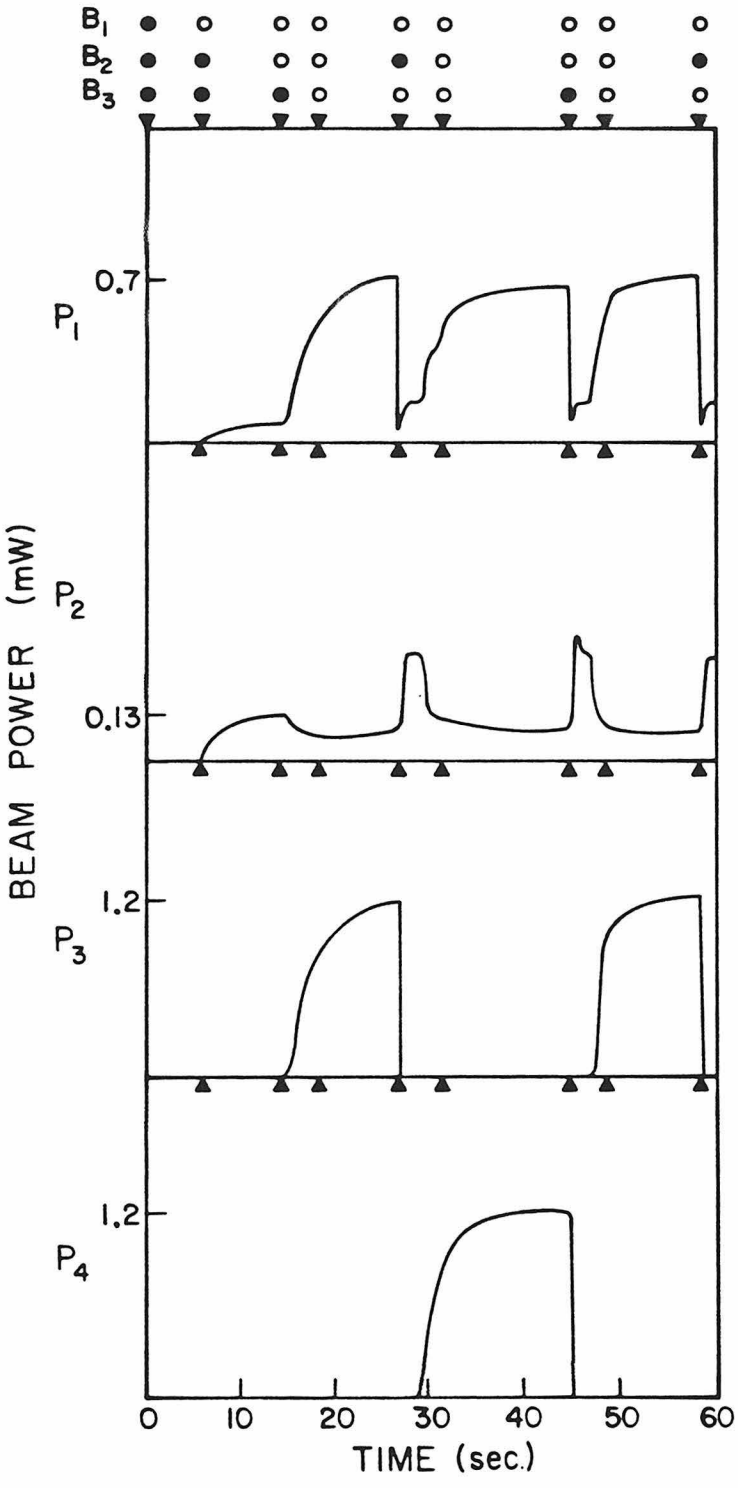

Fig. 6.8 : P_1 is the power of the phase conjugate beam, P_2 is the power of the beam circulating anti-clockwise in the ring cavity, P_3 is the power of oscillation between the crystal and mirror M_3, and P_4 is the power of oscillation between the crystal and mirror M_4. • and o represent the B_i is inserted and removed respectively.

lation between the crystal and M_4 was observed.

[5] When B_2 was inserted, the intensity of the oscillation at M_3 died out ($P_3 \rightarrow 0$) and P_1 decreased drastically, which shows that the major contribution to P_1 came from the oscillation between the crystal and M_3. P_2 increased due to the absence of the auxiliary oscillation, and oscillation at M_4 began to build up. Consequently, P_1 and P_4 increased and P_2 decreased to the steady state value (same steady state value as in step [3]).

[6] When B_2 was removed, the system remained unchanged and no oscillation between the crystal and M_3 was observed.

This cycle can be repeated indefinitely. These two auxiliary oscillations can be considered as two separate bistable states of the system: when the system, originally at one state, is disturbed, it will switch to the other state and remain in that state even when the disturbance is removed.

A complete theory of this phenomenon would require the solution of eight coupled wave equations. Nevertheless, a qualitative understanding of the system can be deduced by making some reasonable approximations.

A necessary condition for oscillation is that after a complete round trip the beam amplitude return to its original value, i.e. gain equals loss. Near the threshold of the auxiliary oscillation, the oscillations are assumed to be pumped by a phase conjugate pair of beams[11] in the main ring resonator with a beam ratio r given approximately by P_2/P_0. Since the oscillation beams are weak compared to the pumping beams at the threshold, the undepleted pump approximation

discussed in section (4.2a) is applicable. The oscillation condition is then

$$R = \frac{1}{r}\left|\frac{J(0)\ e^{-\alpha\ell}}{J(0)\ -\ 1}\right|^2 \geq \frac{1}{M\ T^2} \simeq 1.24 \qquad [6.6]$$

where , from Eq. [3.11]

$$J(0) = \int_0^{\gamma\ell} \frac{e^{-x}\ dx}{1 + r^{-1}e^{-\alpha\ell}\ e^{2\alpha x/\gamma}} \qquad [6.7]$$

and M includes the loss due to the finite reflectivity of the cavity mirror and the loss due to diffraction, T is the Fresnel transmittance of the crystal surface. From a separate experiment, we measured $\gamma\ell$=5.2 and $\alpha\ell$=1.11 for the same beam geometry. A theoretical plot of Eq. (2) for $\gamma\ell$=5.2 and $\alpha\ell$=1.11 is shown in Fig. 6.9. With the pump ratio $r=1.26\times10^{-2}$, R>1.24 (point A), and oscillation can occur. Now the question why there is no oscillation build up in step [4] and step [6], is addressed. There are two reasons: (a) Due the auxiliary oscillation at M_3, r drops to 6.63×10^{-3} and (b) From Eq. (1), the auxiliary oscillation at M_3 is incoherent with the auxiliary oscillation at M_4, so that P_3 can act as an erase beam for P_4. As the result, the effective coupling constant for the auxiliary oscillation at M_4 was reduced[3]

$$(\gamma\ell)_{eff} = \frac{(\gamma\ell)_o}{1 + \dfrac{\text{Erase beam intensity}}{\text{total beam intensity}}}$$

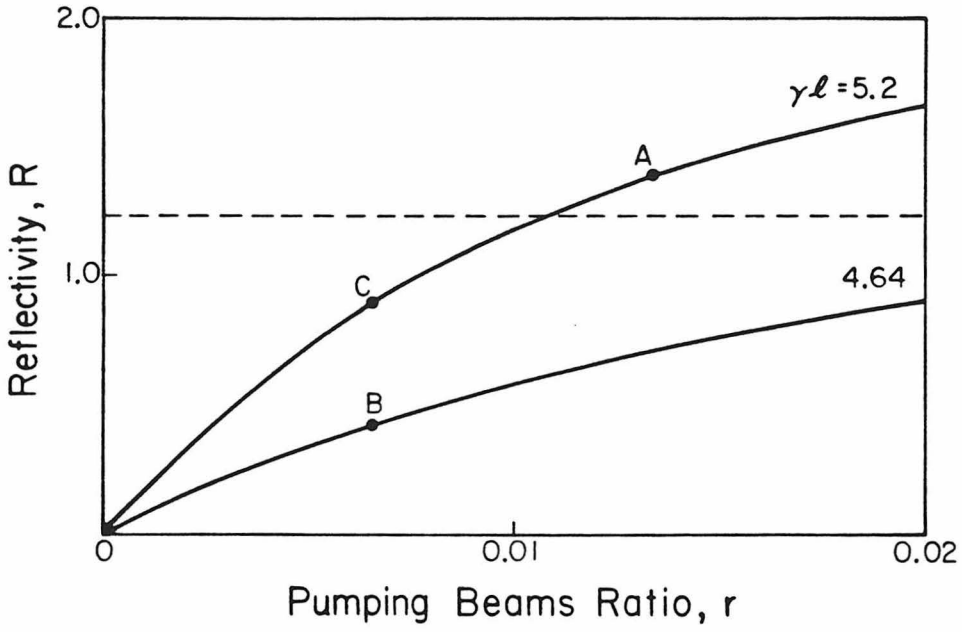

Fig. 6.9 : Theoretical plots of reflectivity R versus ring phase conjugate mirror reflectivity r for $\gamma\ell$=4.64 and 5.2. For R>1.24, oscillation can occur.

$$\simeq \frac{(\gamma\ell)_o}{1 + \frac{P_3}{P_o}} \simeq \frac{5.2}{1 + \frac{1.2}{10}} \simeq 4.64$$

where $(\gamma\ell)_o$ is the coupling constant without an erase beam. Therefore, the net result is R<1.24 (point B) and no oscillation can occur. Step [5] can also be explained in the similar way: when B_2 was inserted, the effective coupling constant increased from 4.64 to 5.2 (point B to point C). The beam ratio r increased gradually as the primary oscillation built up (P_2 increased) and eventually at R>1.24, the auxiliary oscillation began to build up (point C to point A).

If the crystal does not have any pre-written grating except that corresponding to the primary oscillation, then the system does not prefer one oscillation state over the other. A small intensity probe beam can then be used to selectively excite one of the auxiliary oscillations. This was also experimentally observed. In the next chapter this bistable oscillations is proved useful as a thresholding element in an associative memory.

Reference for Chapter 6

1. M. Cronin-Golomb, B. Fischer, J.O. White and A. Yariv, IEEE J. QE-20 12 (1984).
2. S.-K. Kwong, A. Yariv, M. Cronin-Golomb and B. Fischer, J. Opt. Soc. Am. **A**, **3**, 157, 1986.
3. S.K. Kwong, M. Cronin-Golomb and A. Yariv, Appl. Phys. Lett. 45 1016 (1984).
4. S.-K. Kwong and A. Yariv, submitted to Opt. Lett.
5. S. Odoulov, K. Belabaev and I. Kiseleva, Opt. Lett., **10**, 31, 1985.
6. M. Cronin-Golomb, B. Fischer, J.O. White and A. Yariv, Appl. Phys. Lett., **42** 919 (1983).
7. G. Valley and G.J. Dunning, Opt. Lett. **9** 513, 1984.
8. P.W. Smith, I.P. Kaminow, P.J. Maloney and L.W. Stulz, Appl. Phys. Lett. **34**, 25, 1978; Appl. Phys. Lett. **35**, 62, 1979.
9. J. Feinberg, J. Opt. Soc. Am. **72**, 46, 1982.
10. J. Feinberg, Opt. Lett. **8** 480 (1983).
11. The coherent pumping condition is satisfied for the transmission grating since $|L-2L_i|<L_c$ i=1,2, from Eq. (1). A detailed discussion on the coherent conditions in ring PPCM is given by M. Cronin-Golomb, J. Paslaski and A. Yariv, Appl. Phys. Lett. 47 1131 (1985).

Chapter 7: Mathematical operations on images

In recent years, photorefractive crystals have been used to perform various real-time image processing operations. For example, real time convolution and correlation[1], edge enhancement[2], image subtraction[3], differentiation[4], division[5], and inversion[6] have been demonstrated. In this chapter, some mathematical operations on images will be discussed. In section 7.1a, an interferometer using a self-pumped phase conjugate mirror is described, which produces the real time 'exclusive or' operation and image subtraction[7-8]. Also, results of intensity inversion and image differentiation are shown Section 7.1b and 7.1c, respectively. Methods of extending the operation to higher order differentiation and of obtaining the Laplacian are also discussed

(7.1) Real time image subtraction and 'exclusive or' operation

Fig. 7.1 illustrates the system for 'exclusive or' operation. A plane wave with amplitude E_{in} is split by beam splitter BS_1 whose reflection and transmission coefficients are equal to r and t, respectively. Without making any assumptions, let r' and t' be the amplitude reflection and transmission coefficients for wave incident from the opposite sides of the beamsplitter. Each of the two resultant waves then passes through a transparency with amplitude transmittance T_1 for beam 1 and T_2 for beam 2. The two beams are then reflected by a self-pumped phase conjugate mirror (PPCM) with phase conjugate amplitude

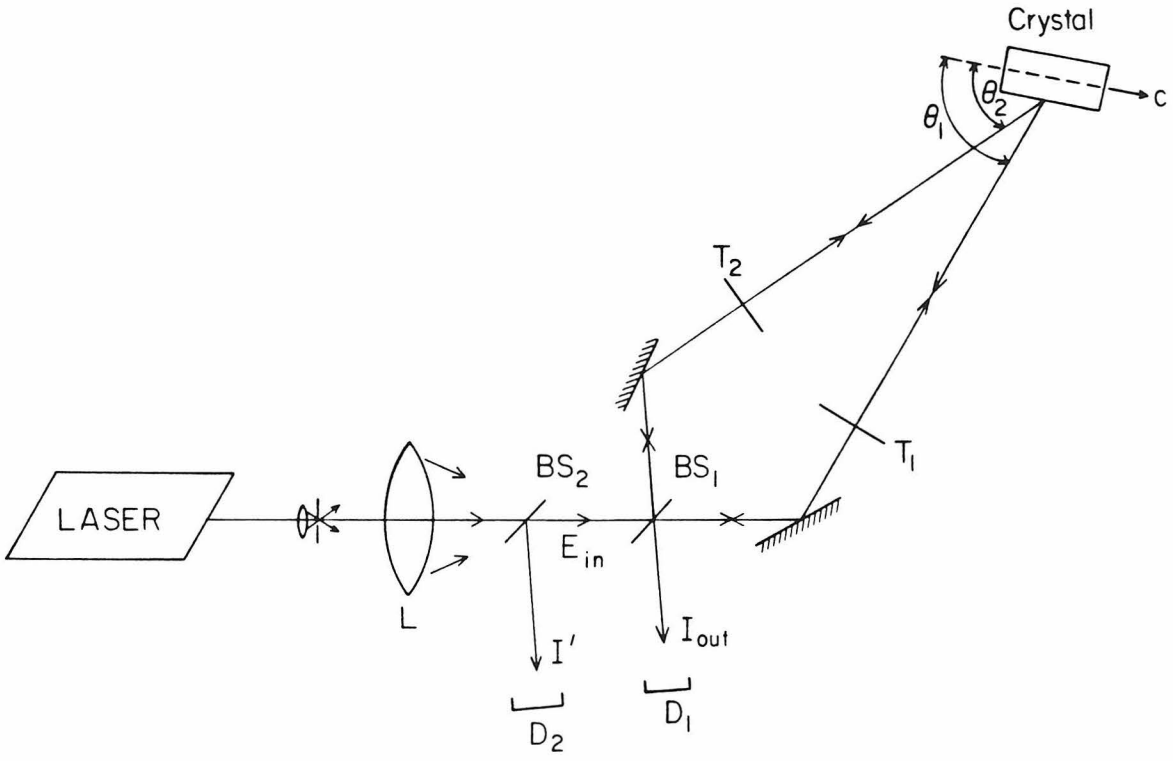

Fig. 7.1: Experimental arrangement to demonstrate the exclusive or operation.

reflectivities R_1 and R_2 for beam 1 and beam 2 respectively. (R_1 and R_2 are in general not the same) The phase conjugated beams recombine interferometrically at beam splitter BS_1 to form an output field intensity I_{out} at detector D_1 given by

$$I_{out} = | r't^*R_1|T_1|^2 + tr^*R_2|T_2|^2 |^2 I_{in} \qquad [7.1]$$

where $I_{in} = |E_{in}|^2$.

From Stokes' principle of the time reversibility of light

$$r't^* + r^*t = 0 \qquad [7.2]$$

so that

$$I_{out} = | R_1|T_1|^2 - R_2|T_2|^2 |^2 |r^*t|^2 I_{in} \qquad [7.3]$$

If the two phase conjugate reflectivities are identical, i.e. $R_1=R_2=R$, then

$$I_{out} = | |T_1|^2 - |T_2|^2 |^2 |r^*tR|^2 I_{in} \qquad [7.4]$$

$$\propto |T_1|^2 \oplus |T_2|^2 \qquad [7.5]$$

where $\oplus$ represents the Boolean 'exclusive or' operation. This is the main result. Similarly, the field intensity I' measured by detector D_2 is

$$I' \propto | |T_1|^2 + |r|^2(|T_2|^2-|T_1|^2)|^2 |R|^2 I_{in} \qquad [7.6]$$

The π phase shift between the complex fields of the two images, which is the key element of the 'exclusive or' operation, is introduced naturally by the time reversibility of light. This is the essential difference between this method and other methods[3] in which the π phase shift was artificially provided by a piezo-electric mirror or an electro-optical modulator. This device is only sensitive to intensity differences of the two transparencies and is independent of the phase information of the transparencies or the optical path lengths of the two arms.

In the experiment, a single TEM_{00} mode Argon laser beam (5145A, 50mW) was expanded and split into two beams by 50% beam splitter BS_1. Each beam was then passed through separate transparencies T_1 and T_2. A lens L (f=30cm) was used to focus the two expanded beams which were adjusted to overlap completely inside the poled $BaTiO_3$ crystal. The crystal was then aligned to form a self-pumped phase conjugate mirror[9] by setting the angles between the beams and the crystal C-axis to $\theta_1=50^o$ and $\theta_2=40^o$. The two image bearing beams were phase conjugated simultaneously with no cross talk[10]. The magnitude of the phase conjugate reflectivities of beam 1 and beam 2 were approximately the same and equal to 25%. The phases of the complex phase conjugate reflection coefficients of the two beams were also the same, since the PPCM regarded the combination of the two input beams as a single complex input wave, and since the beams overlapped in the crystal, they were both reflected from the same set of gratings.† The phase conjugate reflected image bearing beams were then combined interferometrically at the beam splitter BS_1. The two transparencies

† Another method for obtaining phase locking between the two phase conjugate beams is described in Ref. 11, in which a self induced oscillation locks the relative phase between the two phase conjugate beams.

and the detectors were placed close to the beam splitters to reduce diffraction aberration.

The transparencies T_1 and T_2 used in the experiment were pictures of a semicolon and a colon, respectively. The phase conjugate images of these two transparencies are shown in Figs. 7.2a and 7.2b, respectively. Fig. 7.2c is the image detected by D_1, which represents the 'exclusive or operation' (or, in this case, image subtraction) between the two images, $|T_1|^2 \oplus |T_2|^2$. Fig. 7.2d is the image recorded by D_2, which represents $||T_1|^2+|r|^2(|T_2|^2-|T_1|^2)|^2$, and it is proportional to the sum of intensities, $||T_1|^2+|T_2|^2|^2$, when $|r|^2=.5$. Slight edge enhancement effects[2] were also observed in these figures, which are probably due to large object beam intensities as compared to the weaker pump beam intensities. These results are independent of the optical path lengths of either beam between the BS_1 and the crystal.

The response time of the self-pumped phase conjugate mirror obeyed approximately the relation $\tau \simeq 10/I$ s, where I is the total intensity of the interaction beams in mW/mm^2.

(7.2) Real-time intensity inversion

Optical intensity inversion was also observed by simply removing transparency T_2 so that the intensity detected by D_1 is proportional to $|1-|T_1|^2|^2$, whose result follows from Eq. [7.3] when we put $|T_2|^2=1$. Figs. 7.3a and 7.3b are the phase conjugate images of a uniform illumination and a resolution chart, respectively. Fig. 7.3c is the intensity inverted image detected by D_1. Fig. 7.3d is the image addition observed by detector D_2, which is proportional to

Fig. 7.2

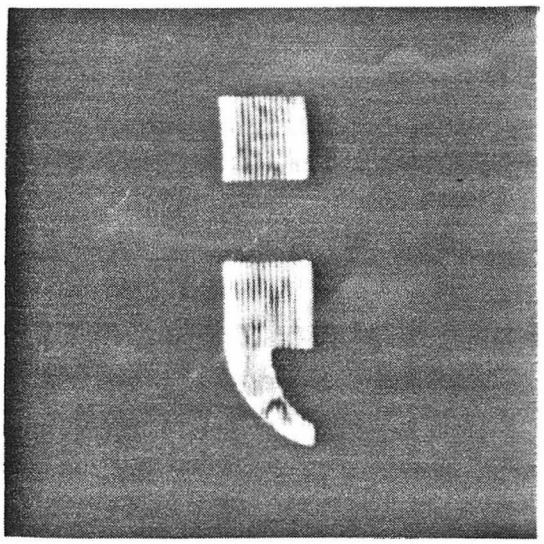

(a) Image of a semicolon after phase conjugation;

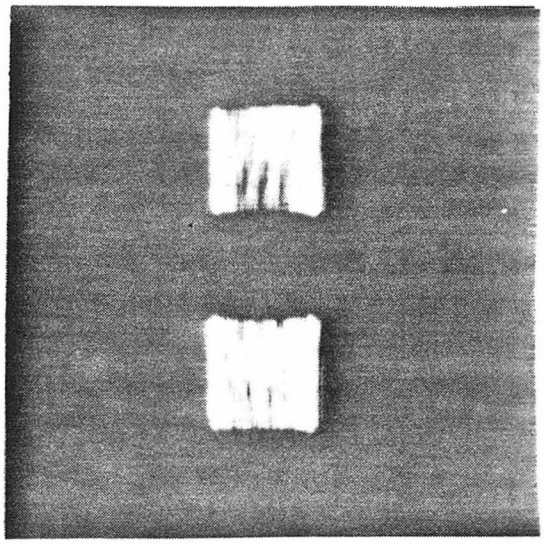

(b) Image of a colon after phase conjugation;

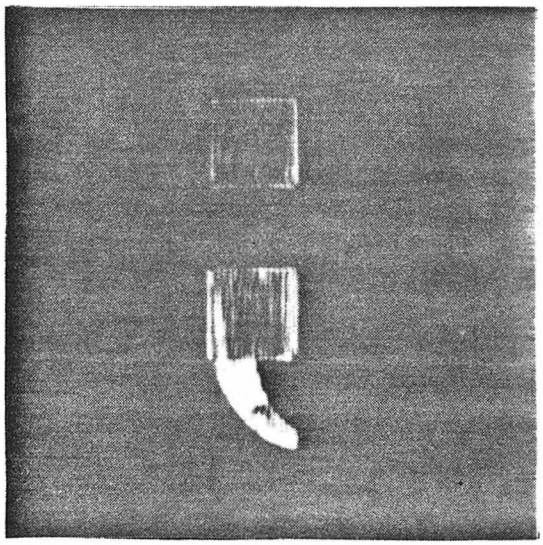

(c) Image subtraction of the semicolon and the colon;

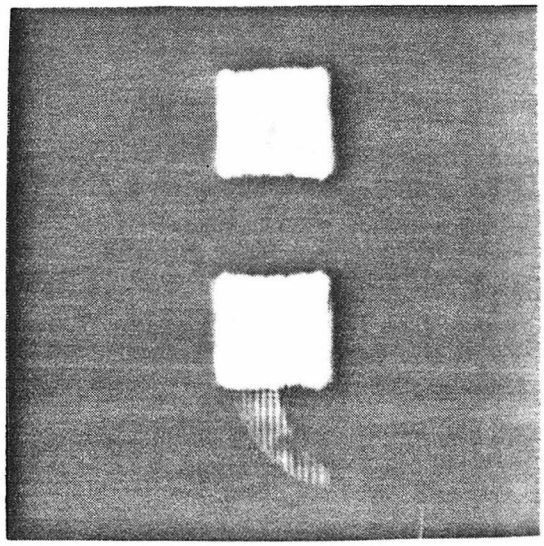

(d) Image detected by detector D_2.

Fig. 7.3 :

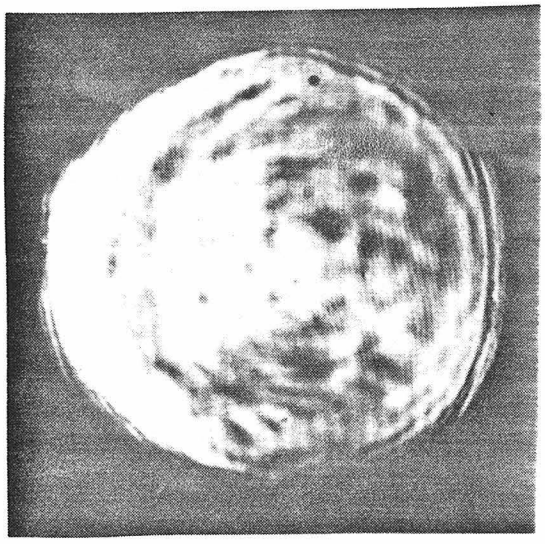

(a) Image of the uniform illumination after phase conjugation.

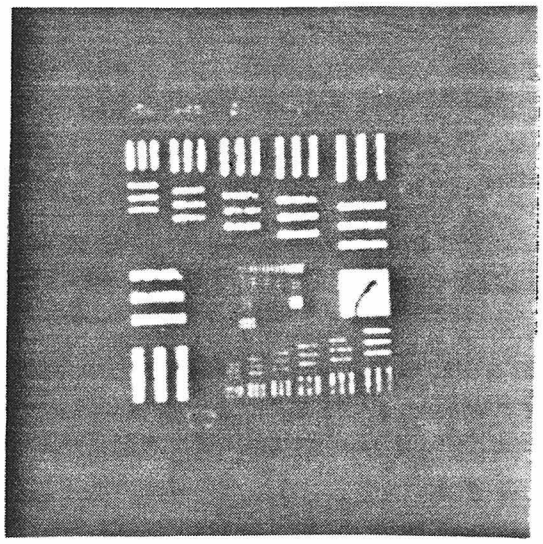

(b) Image of resolution chart after phase conjugation.

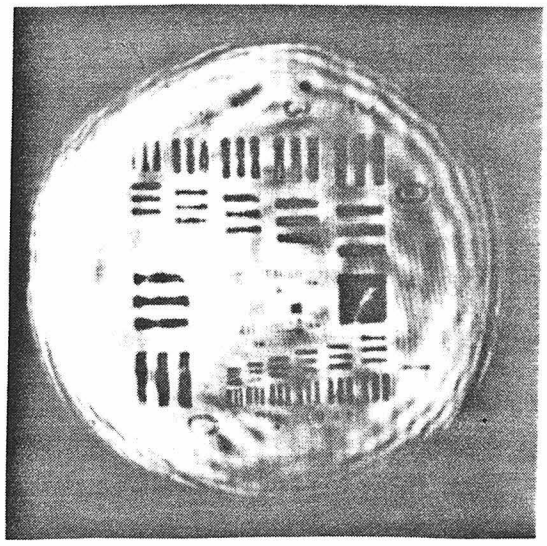

(c) Intensity inversion of the resolution chart.

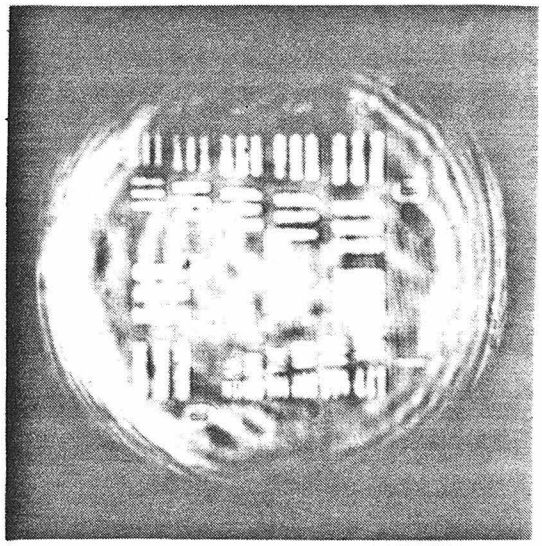

(d) Intensity addition of the resolution chart and the uniform illumination.

$|1+|T_1|^2|^2$.

Intensity inversion by a different method which uses four wave mixing was reported recently by Ochoa et al.[6] In their method the object beam intensity is required to be much higher than that of the reference beam in order to ensure that the diffraction efficiency of the index grating is inversely proportional to the object beam intensity.

(7.3) Real-time image differentiation

The differential of a function I(x,y) can be approximated to any degree of accuracy by using finite differences. Using such a method, the first and second-order differentials are given by

$$\frac{\partial I(x,y)}{\partial x} = \frac{I(x+\Delta x,y)-I(x,y)}{\Delta x} \qquad [7.7]$$

$$\frac{\partial^2 I(x,y)}{\partial x^2} = \frac{I(x+\Delta x,y)-2I(x,y)+I(x-\Delta x,y)}{(\Delta x)^2} \qquad [7.8]$$

Therefore, the differential of any order can be obtained by adding and subtracting various shifted images of a pattern function.

The experimental arrangement used to perform first-order differentiation, which is very similar to Fig. 7.1, is shown in Fig. 7.4. Since the transparency is not placed at the intersection of the two beams, each beam reads a slightly shifted image of the other. The two images are then focused down into the $BaTiO_3$ crystal which through total internal reflection forms a self pumped phase conjugate mirror. The phase conjugate images are thus phase locked and can recombine at BS_1, giving an output amplitude which is proportional to the first

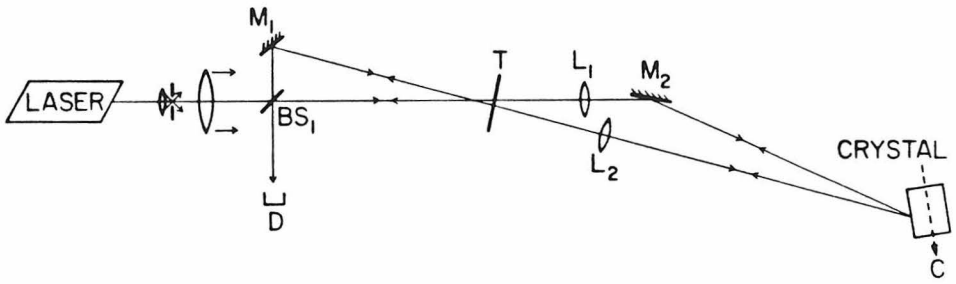

Fig. 7.4 : Experimental arrangement used to demonstrate first order image differentiation.

Fig. 7.5 :

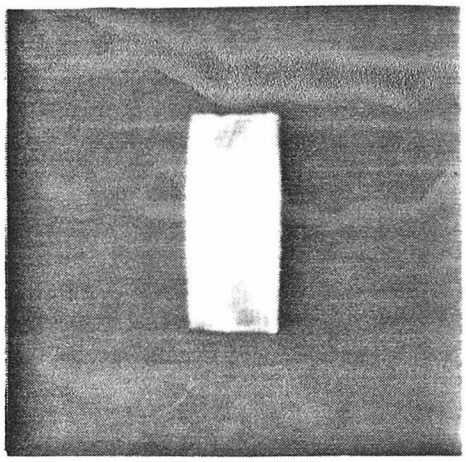

(a) Image of a rectangle after phase conjugation.

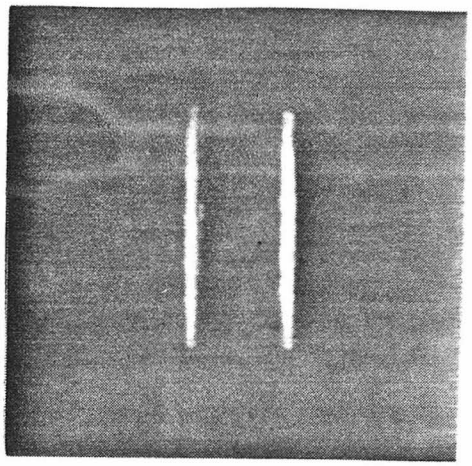

(b) Image of Fig. 6(a) after first-order differentiation.

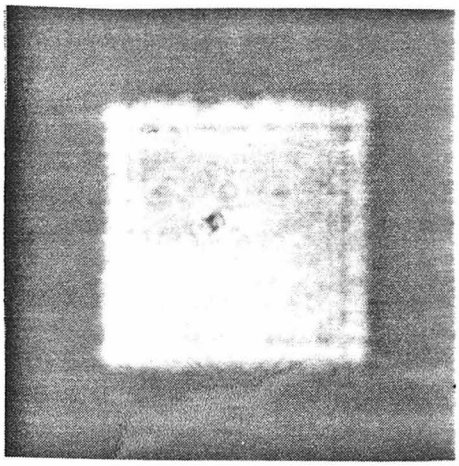

(c) Image of a square after phase conjugation.

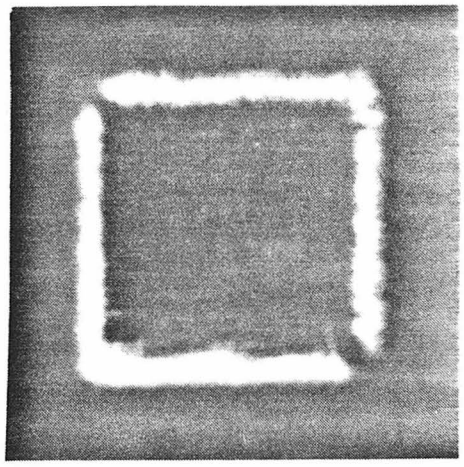

(d) Image after $\frac{\partial}{\partial x} + \frac{\partial}{\partial y}$ operation.

order differential. Results are given in Fig. 7.5. Also given in Fig. 7.5(d) is $(\partial/\partial x + \partial/\partial y)$ obtained by shifting the images by $\Delta x+\Delta y$.

Fig. 7.6 gives the set up used to perform second-order image differentiation. The two outside beams read $T(x+\Delta x,y)$ and $T(x-\Delta x,y)$, while the center beam reads $T(x,y)$. The reflectivity of beam splitter BS_2 is 50%, giving an output amplitude at BS_1 proportional to the second order differential.

$$I_{out} \propto \left| \, |T(x+\Delta x,y)|^2 + |T(x-\Delta x,y)|^2 - 2|T(x,y)|^2 \, \right|^2 \qquad [7.9]$$

Results are given in Fig. 7.7.

Extensions to higher order image differentiation can be obtained by adding up appropriately shifted images into two groups which are then subtracted at the final beam splitter. While the final beam splitter reflectivity can be arbitrary the remaining ones must have their reflectivities chosen to perform the image additions in the correct proportions. The many shifted images required for higher order derivatives may cause difficulties in focusing all the images into a single crystal. In that case two or more crystals phase locked through spontaneous oscillations[14] could be used to handle the many images. Efforts are also under way to couple the multiple images into the crystal using a single optical fiber.

Using methods similar to those used for image differentiation a device can be constructed whose output amplitude is proportional to $\nabla^2 I(x,y)$, where $I=|T(x,y)|^2$. A beam is expanded and split into two beams. One of the beams will read $T(x,y)$. The other beam will be split into four beams of equal intensity using 50% beam splitters.

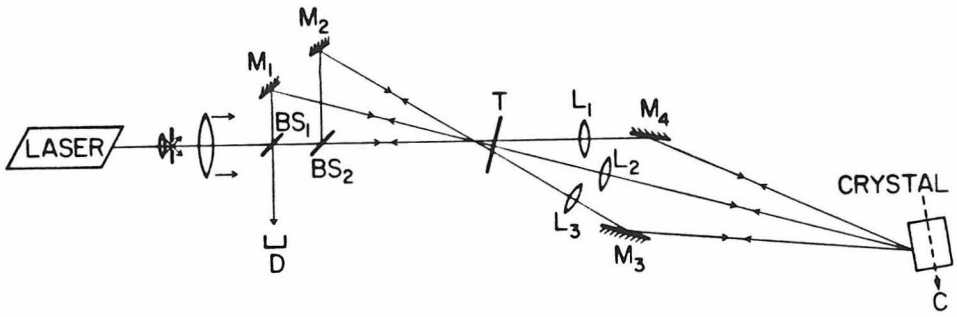

Fig. 7.6 : Experimental arrangement used to demonstrate second order image differentiation.

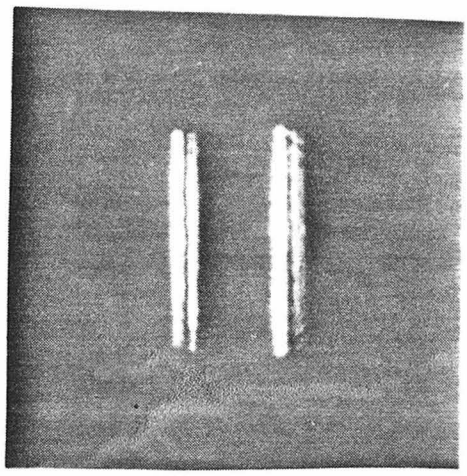

Fig. 7.7 : Image of Fig. 7(a) after second order differentiation.

These beams will then read images of $T(x,y)$ shifted by $\pm\Delta x$ or $\pm\Delta y$. These beams will then recombine at the first beam splitter giving an output proportional to $\nabla^2 I(x,y)$.

References for Chapter 7

1. J.O. White and A. Yariv, Appl. Phys. Lett., **37**, 5, 1980.

2. J. Feinberg, Opt. Lett., **5**, 330, 1980.

3. Related work by J.P. Huignard, J.P. Herriau and F. Micheron, Appl. Phys. Lett., **26**, 256, 1975 and by Y.H. Ja, Opt. Comm., **42**, 377, 1982 employed two sequential exposures of the hologram and was thus not strictly real time.

4. Y.H. Ja, Appl. Phys. B, **36**, 21, 1985.

5. Y.H. Ja, Opt. Comm., **44**, 24, 1982

6. E. Ochoa, L. Hesselink and J.W. Goodman, Appl. Opt., **24**, 1826, 1985.

7. S.-K. Kwong, G. Rakuljic and A. Yariv, Appl. Phys. Lett., **48**, 201, 1986.

8. S.-K. Kwong, G. Rakuljic, V. Leyva and A. Yariv, SPIE O-E LASE'86 Conference, Los Angeles, 1986, paper 613-07

9. In our experiment, a self-pumped phase conjugate mirror using internal reflection at the crystal cornor was used (J. Feinberg, Opt. Lett., **7**, 486, 1982. Other kinds of self-pumped phase conjugate mirror with different geometries (see discussion in section 3.6) also give similar results.

10. J. Feinberg, Opt. Lett., **8**, 480, 1983.

11. M.D. Ewbank, P. Yeh and M. Khoshnevisan and J. Feinberg, Opt. Lett., **10**, 282, 1985.

Chapter 8: Associative holographic memories

Recently there has been a strong interest in the area of associative memories.[1-9] These are memories in which a stored piece of information or "message" can be retrieved whole in response to a partial or similar input. The memory yields the stored message which most "closely" resembles the input. In this chapter, we assume that the information can be encoded into two-dimensional pictorial images. These images are stored in a multiple- exposure hologram. Such a hologram will be used in all the schemes discussed in the following. A method to retrieve the stored images in which the brightness of each retrieved image is proportional to the overlap integral of that stored image and the input image is described. By adding a threshold effect to this operation, an all-optical associative holographic memory of more than one overlapped images is demonstrated for the first time.

(8.1) Holographic images storage

In all the schemes that will be discussed in the next sections, a storage element that can store a large number of messages is used. For example, a large number of messages can be stored if the storage element is a volume transmission hologram. Figure 8.1 shows how a "message" E_i is recorded holographically using a reference beam E_{io}[1-3] (a plane wave, for example,). The direction of the reference beam is different for each stored message. The result is a volume index variation hologram,

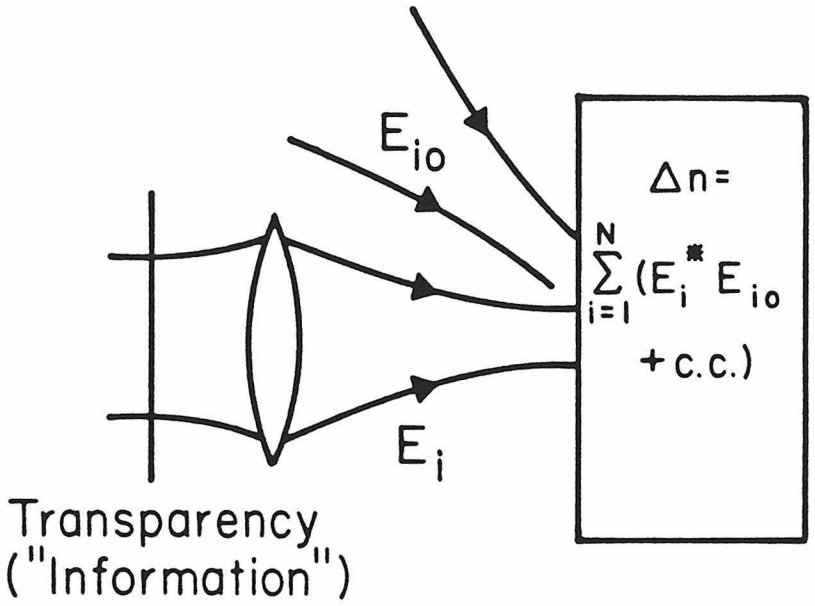

Fig. 8.1 : Information recorded in a fixed hologram Δn. E_i is the beam carrying the information and E_{io} is the reference beam. The angle between E_{io} and E_i is sufficiently large to prevent spillover of information in the memory application into the zero order mode.

$$\Delta n \propto \sum_{i=1}^{N} (E_i^* E_{io} + c.c.) \qquad [8.1]$$

where N is the number of recorded messages. There are several methods of making multiple holograms. For example, 500 fixed holograms, each with more than 2.5% diffraction efficiency, have been recorded in heated Fe-doped $LiNbO_3$[10], and the recording of more than 10 holograms, each with 20% difraction efficiency, in dichromated gelatin[11] has been reported.

(8.2) Experimental demonstration of associative holographic memory

This section describes the first experimental demonstration of an all-optical associative holographic memory where storage of more than one overlapped images is reported†. Extension of this method to a large number of stored messages is also discussed.

The basic premise of this associative memory is as follows: A large number, N, of images ("messages") is stored in a volume hologram using the method described in the previous section. In the retrieval step, the hologram is illuminated with the "partial" input E'. This results in N distinct beams each centered angularly about a direction of one of the reference beams E_{io} used in the recording step. Spatial filtering of these beams results in an optical field comprising the ensemble of original reference beams E_{io} used to record the individual message E_i. Due to a volume overlap effect basic to the hologram, the most intense of these reference beams is that whose corresponding stored message most closely resembles the partial input. All that remains is to employ thresholding or some other equivalent nonlinear

---

† The demonstration of storage and retrieval of more than one image is pivotal since the absence of "cross contamination" of messages is a prerequisite to an associative memory.

effect to squelch all but the most intense reference beam, say E_{jo}, and then use it to illuminate the storage hologram (or a suitable equivalent), thereby obtaining a unique reproduction of the desired message E_j most closely resembling the partial input E'.

The principle of operation is illustrated schematically in Fig. 8.2. The partial input image beam E' is incident on the hologram, thereby giving rise to a diffracted field consisting of a group of N beams, each radiated by a polarization term

$$P_i \propto E'(\Delta n)_i \propto E'E_i^* E_{io} = A'(\vec{r}')A_i^*(\vec{r}')A_{io}(\vec{r}')\, e^{-i\vec{k}_{io}\cdot\vec{r}'} \qquad [8.2]$$

where the slowly varying amplitudes $A(\vec{r})$ are defined by

$$E_i(\vec{r}') = A_i(\vec{r}')\exp(-i\vec{k}_i\cdot\vec{r}') \quad ,$$

$$E'(\vec{r}') = A'(\vec{r}')\exp(-i\vec{k}_i\cdot\vec{r}') \quad ,$$

$$E_{io}(\vec{r}') = A_{io}(\vec{r}')\exp(-i\vec{k}_{io}\cdot\vec{r}') \quad ,$$

where $\vec{r}'$ are the coordinates of points in the hologram, and the $\vec{k}$'s correspond to the principal direction of propagation of the respective wave. The polarization P_i radiates a beam which propagates essentially in the direction of the reference beam E_{io} with a certain angular spread caused by the spatial modulation due to $A'A_i^*$. The distribution of this diffracted beam in the far field (or the focal plane of a lens) can be shown to be given by

$$E_{diff}^{(i)}(\vec{r}) \propto \int_V A'(\vec{r}')A_i^*(\vec{r}')A_{io}(\vec{r}')\, e^{-i(k/r)(xx'+yy')}dx'dy'dz' \qquad [8.3]$$

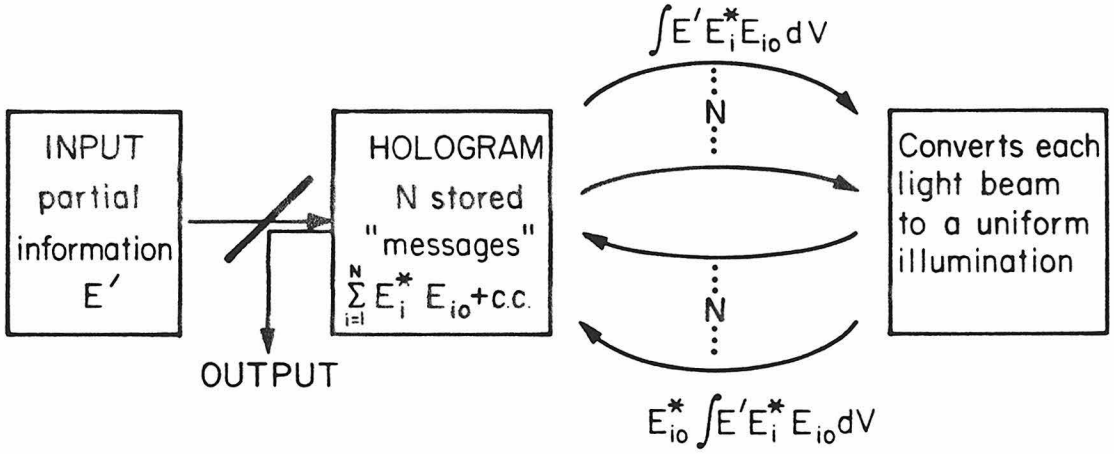

Fig. 8.2 : Schematic diagram of image comparison using feedback from optical fibers.

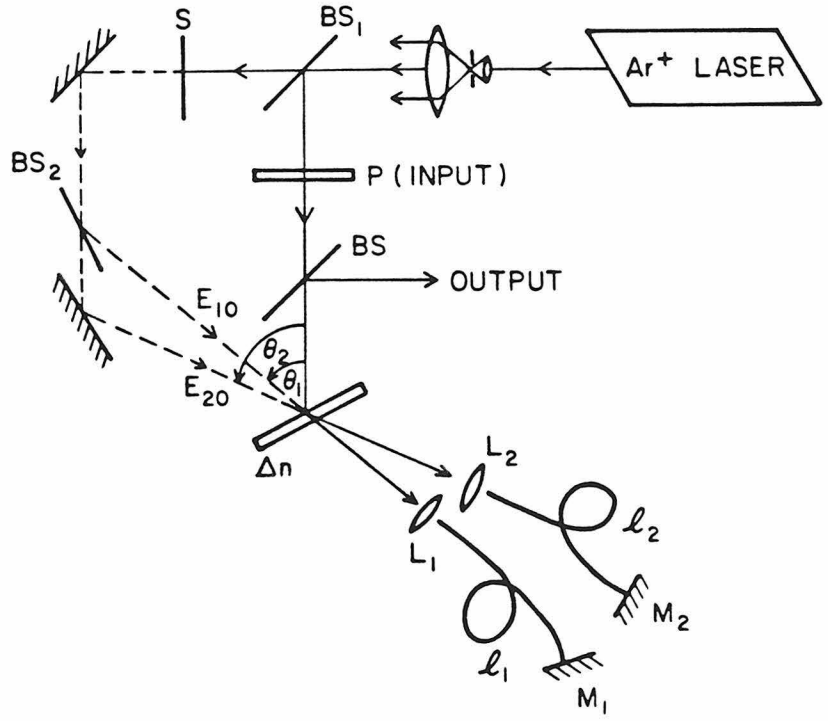

Fig. 8.3 : Experimental arrangement of image comparison using feedback from optical fibers.

where V is the volume of the hologram and $r=|\vec{r}|$ where $\vec{r}$ is the coordinate of a general point in the observation plane. For the proper choice of reference beams, these diffracted beams are angularly and spatially distinct. Each of these beams is then converted to a plane wave propagating opposite to E_{io}. This can be done by spatial filtering and retroreflection. The result of the spatial filtering is a plane-like wave propagating along the direction of each original E_{io} with a complex field amplitude proportional to the overlap integral

$$J_i(\vec{r}) = \int_V A'(\vec{r}')A_i^*(\vec{r}')A_{io}(\vec{r}')\,dx'dy'dz' \qquad [8.4]$$

Assuming equal reflection and spatial filtering losses (or gain) for the beams, each retroreflected plane wave is thus proportional to

$$E_{Refl}^{(i)} \propto E_{io}^* J_i \qquad [8.5]$$

Assuming some thresholding devices will select the most intense of these plane waves, the one with the biggest J_i, and completely suppress the remaining ones, the surviving plane wave is allowed to fall again on the hologram, this time from the right, or used to illuminate a second equivalent hologram. In the first case, as in this experiment, the polarization wave produced in the hologram is of the form

$$P_i'(\vec{r}') \propto (\Delta n)_i E_{Refl}^{(i)} \propto J_i E_{io}^*(\vec{r}')E_i^*(\vec{r}')E_{io}(\vec{r}') = J_i|A_{io}|^2 A_i^*(\vec{r}')\, e^{i\vec{k}_i\cdot\vec{r}'} \qquad [8.6]$$

where in the limit of small diffraction efficiency $|A_{io}|$ is taken to be constant.

The far field radiated by the i-th polarization term is determined as in Eq. [8.3] and is thus

$$E^{(i)}_{reconst} \propto J_i |A_{io}|^2 \int_V A_i^*(\vec{r}') e^{i(k/r)(xx'+yy')} dx'dy'dz' \qquad [8.7]$$

Eq. [8.15] describes the process of reconstruction of a volume hologram Δn. $A_{io}A_i^*$ is illuminated by a plane wave A_{io}^* traveling in the opposite sense to that used in recording it. The result, from basic holography, is that the phase conjugate $A_i^*(\vec{r})$ of the original image. The integral of Eq. [8.7] is made up of a sum of Fraunhoffer diffraction integrals[12], each for a slice of thickness dz' centered on z'. Each "slice" generates a field proportional to $A_i^*(\vec{r})$ at the point of observation $\vec{r}$, with the individual contributions adding up in phase. The far field radiated by the hologram is thus

$$E_{reconst}(\vec{r}) \propto J_i |A_{io}|^2 A_i^*(\vec{r}) \qquad [8.8]$$

and is proportional to the conjugate of the message field $A_i(\vec{r})$.

The above device thus selects and displays the one stored image which is "closest" to the partial or uncertain input. The "closest" stored image is the one with the largest spatial overlap integral J_i.

An experimental demonstration of these ideas is depicted in Fig. 8.3. The hologram Δn was recorded using, first, picture E_1 (Fig. 8.4(a)) and reference E_{10}, followed in a second exposure by a recording of E_2 (Fig. 8.4(f)) with reference beam E_{20}. The pictures E_1 and

Fig. 8.4 :

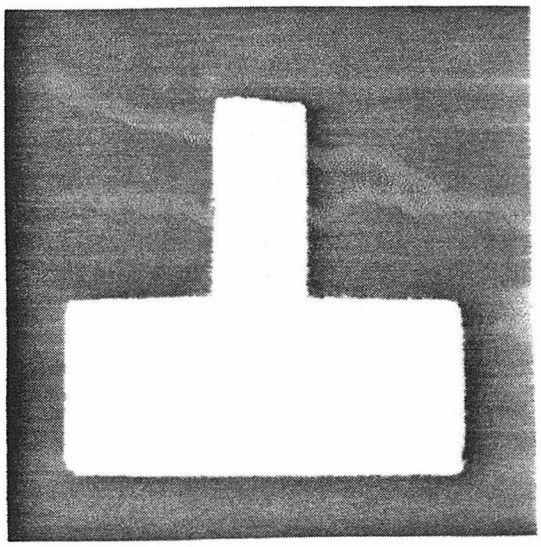

(a) Stored image E_1;

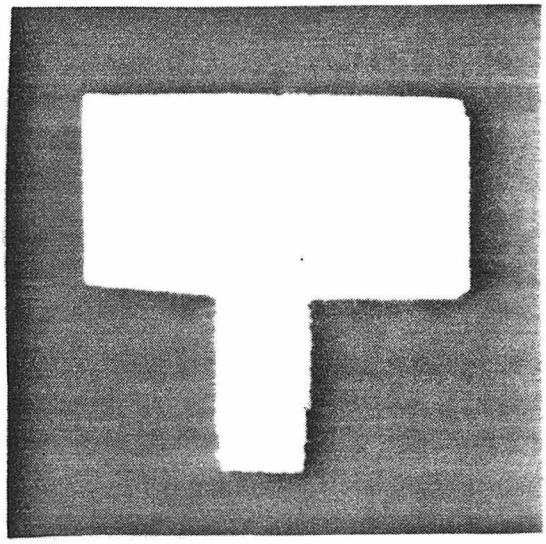

(f) Stored image E_2;

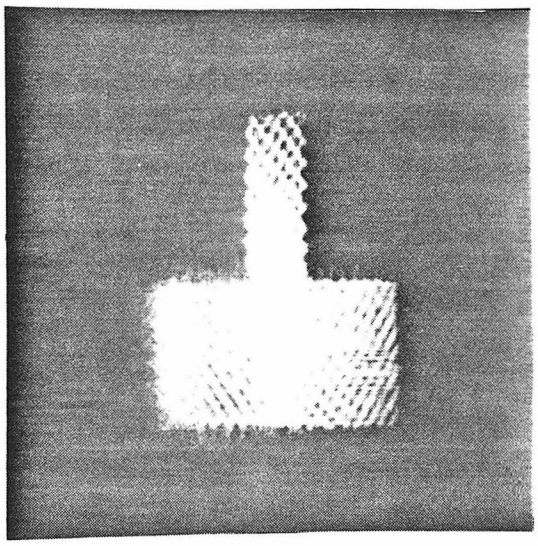

(b) image E_1 diffracted off the hologram by a plane wave input at plane P;

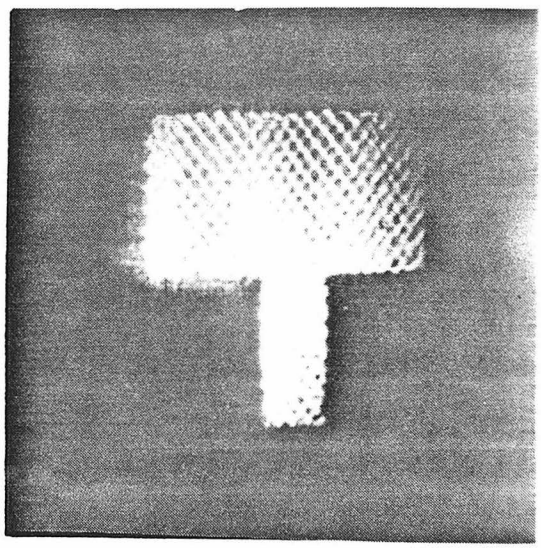

(g) image E_2 diffracted off the hologram by a plane wave input at plane P;

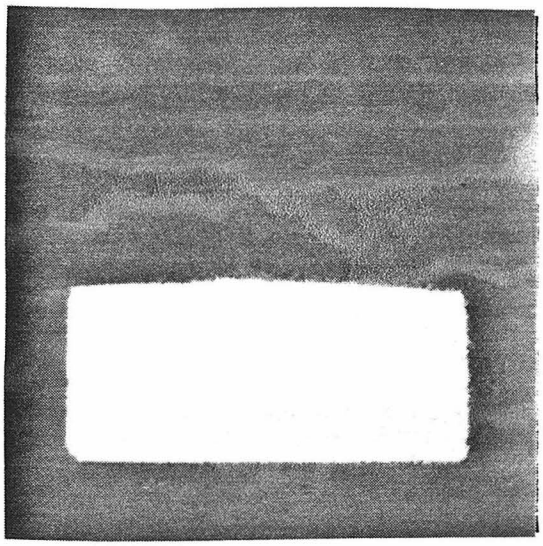

(c) partial image input E_1';

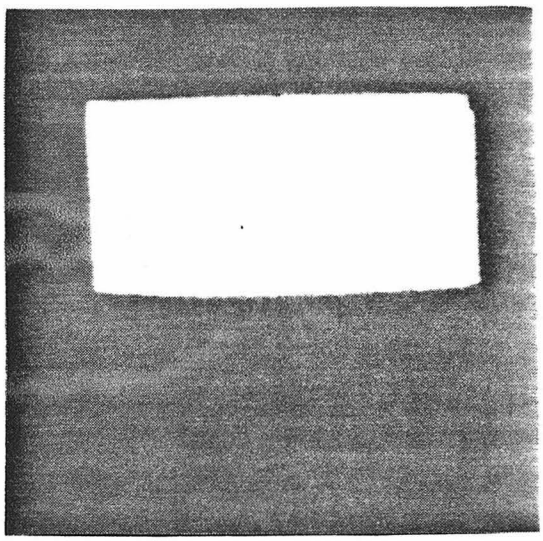

(h) partial image input E_2';

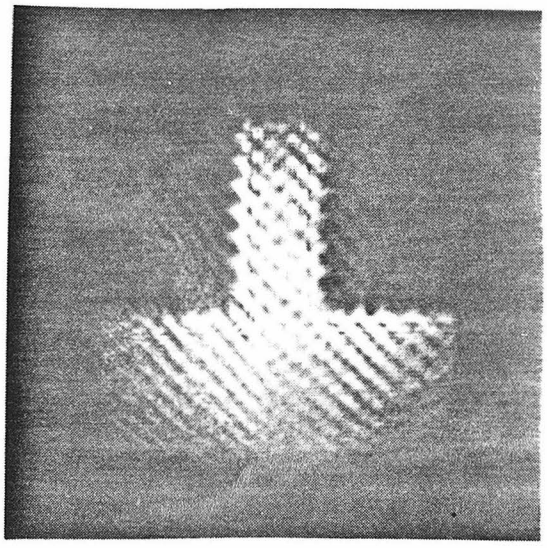

(d) retrieval of the stored messages E_1 by the partial image E_1' using feedback from optical fibers;

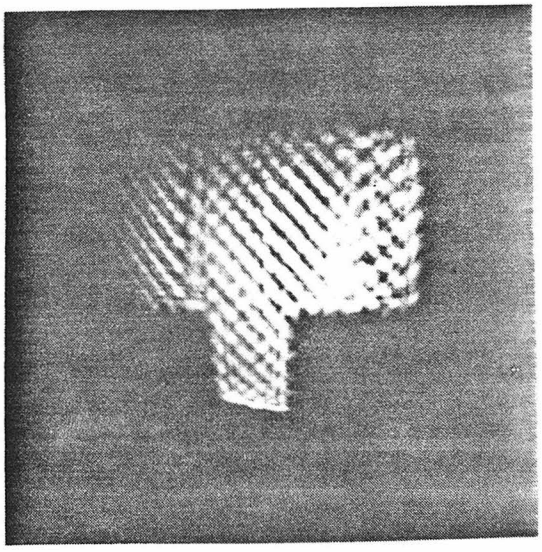

(i) retrieval of the stored image E_2 by the partial image E_2' using feedback from optical fiber;

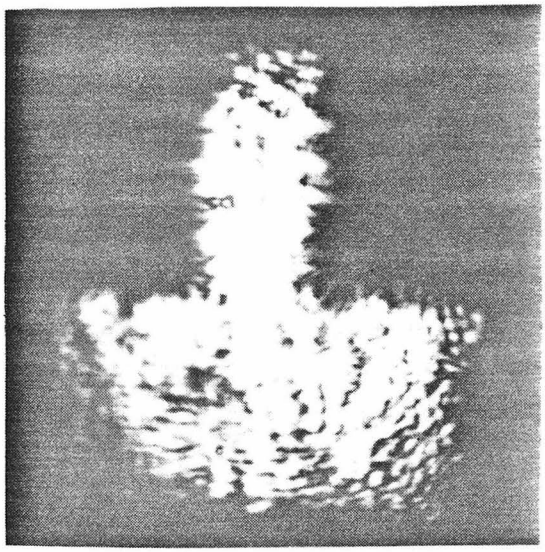

(e) retrieval of the stored messages E_2 by the partial image E_2' using associative memories with thresholding device;

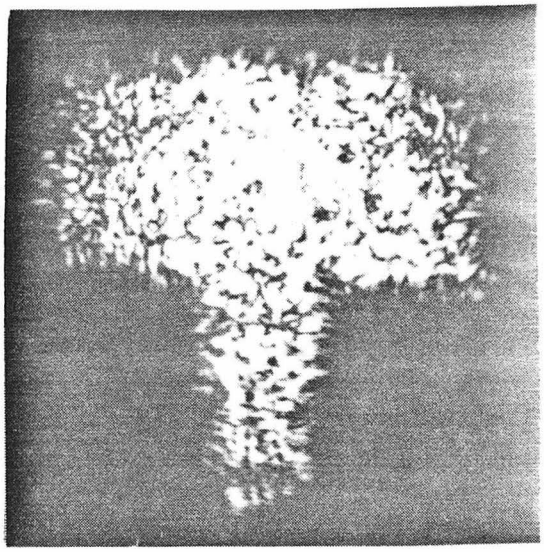

(j) retrieval of the stored image E_2 by the partial image E_2' using associative memories with thresholding device.

E_2 were placed at plane P during their respective recordings. In the retrieval experiment, the reference arm was blocked off with stop S and the partial input picture E' was inserted in plane P. The two images, E_1 and E_2, overlap by approximately 50%. The images diffracted off the hologram by a plane wave input at plane P are shown in Fig. 8.4(b) and 8.4(g). The diffraction efficiency of the E_1 (or E_2) hologram was about 20%. Either of the partial images $E_{\frac{1}{2}}$ or $E_{\frac{1}{2}}$, which are shown in Fig. 8.4(c) and (h), respectively, was used, one at a time, as inputs at plane P. The two resulting beams diffracted simultaneously off the hologram and were separately coupled into two single mode optical fibers with 4 μm core diameter. The length of the fibers was about 85cm. A plane mirror was placed at the end of each fiber to reflect the light back into the fiber. The spatial filtering due to propagation through the single mode fibers helped convert each diffracted beam $E_{diff}^{(i)}$ to a near plane wave E_{io}^{*} propagating opposite to E_{io}. These reflected beams were used to readout the hologram. The results of the experiment are shown in Fig. 8.4(d) and (i). Although no thresholding element was included in this case, the experimental results show good discrimination against the second (undesired) stored image which has a much smaller overlap with the input image. This is because fields $E_{\frac{1}{2}}E_1^{*}$ and $E_{\frac{1}{2}}E_2^{*}$ have low spatial frequencies and can thus be effectively coupled into a single mode fiber, whereas fields $E_{\frac{1}{2}}E_2^{*}$ and $E_{\frac{1}{2}}E_1^{*}$ cannot since they contain higher order Fourier spatial frequencies.

Previously the use of a thresholding device to single out the strongest diffracted (and spatially filtered) beam from the hologram

has already been discussed. A schematic diagram of the associative memory with a thresholding device is shown in Fig. 8.5. Electronic thresholding devices in combination with photo-detectors have already been demonstrated in 'Hopfield' types of associative memories[6]. All optical thresholding devices have the advantage of natural interconnectivity with other optical systems. The thresholding device used in this experiment is the bistable oscillator[13] with a ring passive phase conjugate mirror[14]. The experimental arrangement of this system is shown in Fig. 8.6. The first part of the experiment involving hologram recording and read-out by the partially complete input is the same as in the previous experiment. The two diffracted beams were coupled into two graded-index optical fibers with 100 μm core diameter. The output beams from the fibers were then focused and injected into the bistable oscillator.

The principle of operation of the bistable oscillator has been discussed in section 6.2. In this experiment, it suffices to describe it as a device that only allows one, the strongest, of the two input beams to exist. This surviving (reference) beam is used to illuminate a transparency, the same as that used to record the corresponding message, thereby resulting in an output E_1 or E_2, but not both, depending on the surviving reference beam. The experimental results are shown in Fig. 8.4(e) and (j).

The number of stored images can be expanded by using a curved mirror in the thresholding device instead of two auxiliary mirrors as described above. Other thresholding devices, such as microchannel spatial light modulators (MSLM) device[15] or the imaging threshold

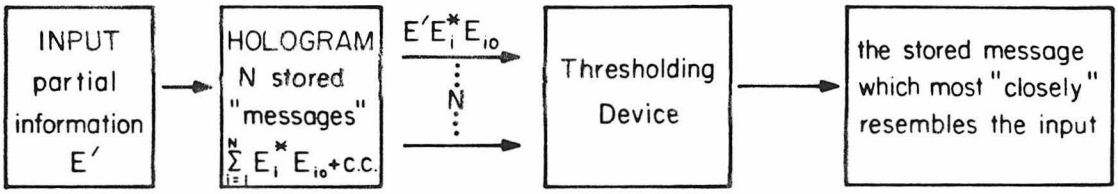

Fig. 8.5 : Schematic diagram of associative memories with thresholding device

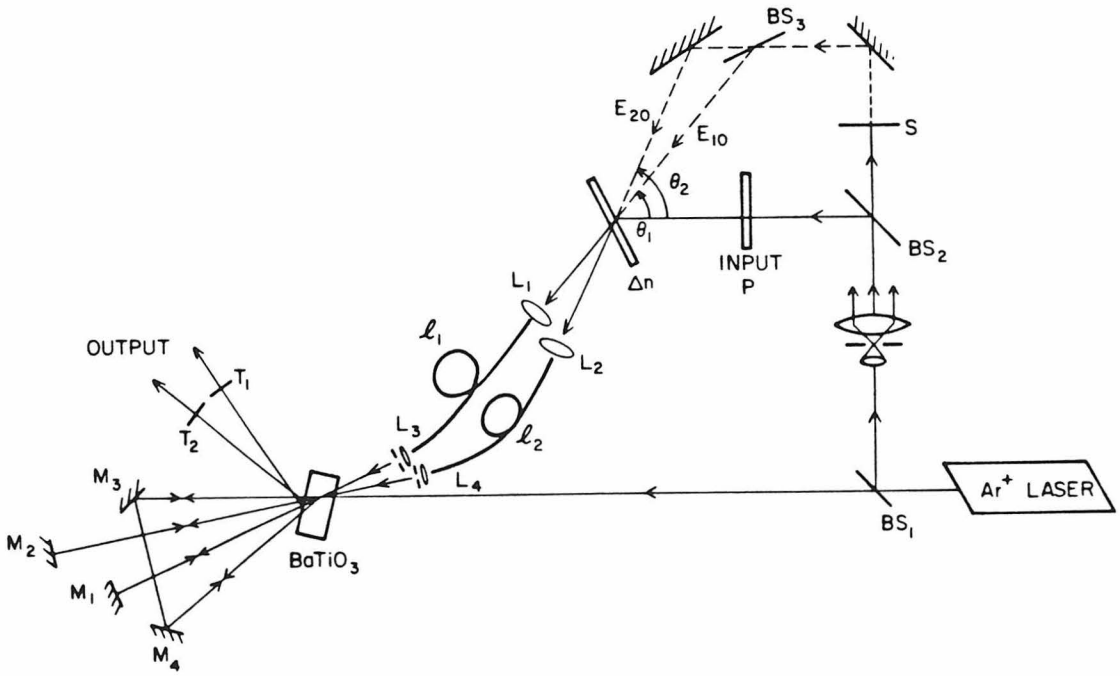

Fig. 8.6 : Experimental arrangement of associative memories with bistable oscillator

detector with a phase conjugate resonator[16] can also be used in this system. Such experiments are currently in progress.

References for Chapter 8

1. A. Yariv, S.-K. Kwong and K. Kyuma, Appl. Phys. Lett., 48, pp. 1114, 1986.
2. A. Yariv, S.-K. Kwong and K. Kyuma, SPIE O-E LASE'86 Conference, paper 613-01, 1986.
3. A. Yariv and S.-K. Kwong, Opt. Lett., **11**, 186, 1986.
4. D. Gabor, IBM J. Res. Dev., **13**, 156, 1969.
5. J.J. Hopfield, Proc. Nat. Acad. Sci. USA, **79**, 2554, 1982.
6. D. Psaltis and N. Farhat, Opt. Lett., **10**, 98, 1985.
7. A session on "Associative memories and optics" at the Optical Society of America Annual Meeting, Washington D.C., 1985, Technical Digest, session WK and WT, T. Kohonen, paper WK1; J.A. Anderson, paper WK2; D.Z. Anderson, paper WT5; G.J. Dunning, E. Marom, Y. Owechko and B.H. Soffer, paper WT8.
8. D. Anderson, Opt. Lett., **11**, 56, 1986.
9. B.H. Soffer, G.J. Dunning, Y. Owechko and E. Marom, Opt. Lett., **11**, 118, 1986.
10. D.L. Staebler, W.J. Burke, W. Phillips, and J.J. Amodei, Appl. Phys. Lett., **26**, 182, 1975.
11. D. Meyerhofer, RCA Rev., **33**, 110, 1972.
12. See for example, "Introduction to Fouier Optics" by J.W. Goodman, McGraw-Hill Book Company, New York 1968, P.61.
13. S.-K. Kwong and A. Yariv, Technical Digest, Optical Society of America Annual Meeting, Washington D.C., 1985, paper THU3.
14. M. Cronin-Golomb, B. Fischer, J.O. White and A. Yariv, Appl. Phys. Lett., **42**, 919, 1983.

15. C. Warde and J. Thackara, Opt. Eng., 22, 695, 1983.

16. M.B. Klein, G.J. Dunning, G.C. Valley, R.C. Lind and T.R. O'Meara, Conference on Lasers and Electro-optics, 1985, Technical Digest, paper PD5-1.

List of publications resulting from thesis research

1. "Oscillations with photorefractive gain", S.-K. Kwong, M. Cronin-Golomb, and A. Yariv, to be published in IEEE J. Quantum Electron., Aug,. 1986.

2. "Bistable oscillations with a self-pumped phase conjugate mirror", S.-K. Kwong and A. Yariv, to be published in Opt. Lett., June, 1986.

3. "Demonstration of an all-optical associative holographic memory", A. Yariv, S.-K. Kwong, and K. Kyuma, Appl. Phys. Lett., vol. 48, pp. 1114, 1986.

4. "One-way, real-time optical wave front convertors", S.-K. Kwong and A. Yariv, Appl. Phys. Lett., 48, 564, 1986.

5. "Real time image subtraction and 'exclusive or' operation using a self-pumped phase conjugate mirror", S.-K. Kwong, G.A. Rakuljic and A. Yariv, Appl. Phys. Lett., 48, 201, 1986.

6. "Associative memories based on message bearing optical modes in phase conjugate resonators", A. Yariv and S.-K. Kwong, Opt. Lett., vol. 11, pp. 186, 1986.

7. "Wave mixing in dynamic holographic materials", J.O. White, M. Cronin-Golomb, B. Fischer, S.-K. Kwong and A. Yariv. (Chapter 4 of the book "Photorefractive materials and applications" Vol. II, edited by P. Gunter and J.P. Huignard.)

8. "The phase of phase conjugation and its effect in the double phase conjugate resonator" S.-K. Kwong, M. Cronin-Golomb, B. Fischer and A. Yariv, J. Opt. Soc. Am. A, 3, 157, 1986.

9. "Optical path length to frequency converting interferometer using photorefractive oscillation" S.-K. Kwong, A. Yariv, M. Cronin-

Golomb and I. Ury, Appl. Phy. Lett.,47 460 (1985).

10. "Theory of laser oscillation in resonators with photorefractive gain", A. Yariv and S.-K. Kwong, Opt. Lett., vol. 10, pp. 454, 1985.

11. "Experimental studies of phase conjugation with depleted pumps in photorefractive media", S.-K. Kwong, Young-Hoon Chung, M. Cronin-Golomb and A. Yariv, Opt. Lett. **10**, 359, 1985.

12. "Non-degenerate optical oscillation in a resonator formed by two phase conjugate mirror" M. Cronin-Golomb, B. Fischer, S.-K. Kwong, J.O. White and A. Yariv, Opt. Lett. **10**, 353, 1985.

13. "Optical bistability and hysteresis with a photorefractive self-pumped phase conjugate mirror", S.-K. Kwong, M. Cronin-Golomb and A. Yariv, Appl. Phys. Lett. **45**, 1016, 1984.

14. "Multicolor passive (self-pumped) phase conjugation", M. Cronin-Golomb, S.-K. Kwong and A. Yariv, Appl Phys. Lett. 44, 727, 1984.